INFRARED LOW OBSERVABLE MATERIAL DESIGN, SYNTHESIS AND CHARACTERIZATION

A THESIS SUBMITTED TO
THE GRADUATE SCHOOL OF NATURAL AND APPLIED SCIENCES
OF
MIDDLE EAST TECHNICAL UNIVERSITY

BY

AHMET KESKİN

IN PARTIAL FULFILLMENT OF THE REQUIREMENTS
FOR
THE DEGREE OF MASTER OF SCIENCE
IN
METALLURGICAL AND MATERIALS ENGINEERING

JANUARY 2023

Approval of the thesis:

INFRARED LOW OBSERVABLE MATERIAL DESIGN, SYNTHESIS AND CHARACTERIZATION

submitted by **AHMET KESKİN** in partial fulfillment of the requirements for the degree of **Master of Science** i**n Metallurgical and Materials Engineering, Middle East Technical University** by,

Prof. Dr. Halil Kalıpçılar
Dean, Graduate School of **Natural and Applied Sciences** _____

Prof. Dr. Ali Kalkanlı
Head of the Department, **Metallurgical and Materials Eng.** _____

Prof. Dr. Hüsnü Emrah Ünalan
Supervisor, **Metallurgical and Materials Eng., METU** _____

Prof. Dr. Alpan Bek
Co-Supervisor, **Physics, METU** _____

Examining Committee Members:

Assoc. Prof. Dr. Simge Çınar Aygün
Metallurgical and Materials Eng, METU _____

Prof. Dr. Hüsnü Emrah Ünalan
Metallurgical and Materials Eng., METU _____

Assoc. Prof. Dr. Alpan Bek
Physics, METU _____

Assist. Prof. Dr. Yusuf Keleştemur
Metallurgical and Materials Eng., METU _____

Assist. Prof. Dr. Şahin Coşkun
Metallurgical and Materials Eng., ESOGU _____

Date: 27.01.2023

I hereby declare that all information in this document has been obtained and presented in accordance with academic rules and ethical conduct. I also declare that, as required by these rules and conduct, I have fully cited and referenced all material and results that are not original to this work.

Name Last name : Ahmet Keskin

Signature :

ABSTRACT

INFRARED LOW OBSERVABLE MATERIAL DESIGN, SYNTHESIS AND CHARACTERIZATION

Keskin, Ahmet
Master of Science, Metallurgical and Materials Engineering
Supervisor: Prof. Dr. Hüsnü Emrah Ünalan
Co-Supervisor: Assoc. Prof. Dr. Alpan Bek

January 2023, 123 pages

In recent years, infrared low-observable technology has come to the fore in the aerospace and defense industry to conceal military aircraft against rapidly developing infrared search and tracking systems. Pigment materials developed for coatings applied to aircraft surfaces based on materials science and engineering in line with electromagnetic principles play a crucial role in this regard. Although low-observable structures were obtained in the 8-14 μm infrared wavelength range in particle studies, radar and visible region invisibility, which are among the stealth requirements, posed the major challenge. Core/shell particles developed to provide low observability in the multiband range resulted in succesful demonstrations on this subject. Although efficient results were obtained for the radar and visible region in the literature, sufficiently low infrared emissivity could not be obtained. In addition, there are only limited number of studies investigating the efficiency of the particles embedded in the coating in the literature.

In this study, the focus is on the development of infrared low emissivity core/shell particles, as well as radar and visible region reflectance. In the first step, candidate materials were screened for the development of core/shell particles. Aluminum,

which is the most efficient material in this field, was determined as the core, and magnetite (Fe_3O_4), silica (SiO_2), titania (TiO_2) and zinc oxide (ZnO) were determined as the shell materials. Depending on the shell thickness of the determined materials, 8-14 μm infrared reflectance performances in the form of metal/metal oxide core/shell particles in the simulation environment under the same conditions were analyzed by FDTD method. Al/ZnO core/shell particles were decided to be synthesized, showing the highest performance in all shell thicknesses. Solvothermal synthesis method was used for the synthesis of Al/ZnO core/shell particles and the effect of temperature and Zn molar ratio were investigated in detail. A systematic material characterization study was performed on the Al/ZnO particles using X-Ray diffraction (XRD), scanning electron microscopy (SEM) and energy dispersive X-Ray Analysis (EDX) methods. Following characterisation, powders were combined with aerospace-standard polyurethane by 1/1 weight ratio and the composites were coated onto glass and aluminum substrates. Firstly, 8-14 μm FTIR spectrometer transmittance and reflectance performances of powder and composite coatings were investigated, and then the visible region reflectance of the composite coatings were investigated with UV-Vis spectrophotometer. As the closest value to Al absorbance, Al/ZnO core/shell powder with flake-shaped shell structure synthesized at a reaction temperature of 150 °C demonstrated the closest absorbance to Al in LWIR band. The absorbance and reflectance characteristics of the PU-matrixed composite coatings with pure Al and core/shell particles were evaluated. The average FTIR reflectance of the core/shell composite coating closest to composite coating with Al particle was measured as 45.45%. The results obtained from coatings were consistent with the powder samples. Thermal images of composite materials were obtained at 60, 80 and 100 °C, and the closest value to Al/PU composite coating (emissivity of 0.888) was obtained from Al/ZnO composite coating (emissivity of 0.931). The coatings of Al/PU and Al/ZnO/PU resulted with low-emissivity in previous test were examined depending on the filler fraction from 0.5/1 to 2/1 by weight. The lowest emissivity values of 0.724 and 0.805 were measured in Al/PU and Al/ZnO/PU composite coatings at a particle/binder ratio of 2/1 by weight, respectively. In addition, it has

been proven that lower emissivity values were obtained from Al/ZnO-filled composites than pure Al/PU composites when the core/shell filler fraction is increased. The X-band radar absorbance performances of the composite materials with the lowest emissivity value were examined. As average, X-band radar reflectance was decreased by 10% and visible reflectance was reduced by 4.1% in composite materials with core/shell particles when compared to Al/PU composite coatings. In this study, the visible band absorbance and radar absorbance performances were improved compared to pure Al with development core/shell particles. Consequently, considering all the requirements of stealth characteristics, besides providing LWIR low radiation, it has been proven that the core/shell structures are promising materials to meet radar and visible range low observability.

Keywords: Infrared Stealth Technology, Solvothermal Synthesis, Low-Emissivity Core/shell, FDTD method, Multiband Low Observability

ÖZ

KIZILÖTESİ DÜŞÜK GÖZLENEBİLİR MALZEME TASARIM, SENTEZ VE KARAKTERİZASYONU

Keskin, Ahmet
Yüksek Lisans, Metalurji ve Malzeme Mühendisliği
Tez Yöneticisi: Prof. Dr. Hüsnü Emrah Ünalan
Ortak Tez Yöneticisi: Prof. Dr. Alpan Bek

Ocak 2023, 123 sayfa

Kızılötesi düşük görünürlük teknolojisi, kızılötesi arama ve takip sistemlerinin sahada verimli operasyonlar gerçekleştirmesi ile birlikte havacılık ve savunma endüstrisinde ön plana çıkmıştır. Elektromanyetik prensipler doğrultusunda malzeme bilimi ve mühenisliğine dayalı uçak yüzeyine uygulanan kaplamalar için geliştirilen pigment malzemeleri bu konuda kritik rol oynamaktadır. Bu bağlamda, malzemenin kızılötesi radyasyon oranını belirleyen emisivite parametresi göz önünde bulundurularak, literatürde kızılötesi düşük-emisvite partikül çalışmaları yapılmıştır. Partikül çalışmalarında, 8-14 μm kızılötesi dalga boyu aralığında düşük görünür yapılar elde edilse de, düşük görünürlük gereksinimlerinden olan radar ve görünür bölge görünmezliği en büyük zorluğu oluşturmuştur. Çoklu dalga boyu aralığında düşük görünürlük sağlamak için geliştirilen çekirdek-kabuk partiküller bu konudaki verimli çalışmalar olmuştur. Literatürde bu konuda yapılan çalışmalarda, radar ve görünür bölge için verimli sonuç alınsa da yeterince düşük kızılötesi emisivite elde edilememiştir. Bunun yanında, literatürde geliştirilen parçacıkların kaplama formundaki verimliliğinin araştırıldığı kısıtlı sayıda çalışma bulunmaktadır.

Bu çalışmada, kızılötesi düşük emisivite çekirdek-kabuk parçacıkların geliştirilmesine odaklanılıp, bunun yanında radar ve görünür bölge yansıtma oranları da göz önünde bulundurulmuştur. İlk adımda, çekirdek-kabuk parçacıkların geliştirilmesi için literatürde bulunan çalışmalardan aday malzemeler araştırılmış, çekirdek için bu konudaki en verimli malzeme olan alüminyum, kabuk için Fe_3O_4, SiO_2, TiO_2 ve ZnO belirlenmiştir. Belirlenen malzemelerin kabuk kalınlığına göre, metal çekirdek - metal oksit kabuk formunda aynı şartlardaki simülasyon ortamında kızılötesi yansıtma performansları FDTD metodu ile analiz edilmiş, Al/ZnO çekirdek-kabuk partikül, tüm kalınlıklardaki en yüksek performansı göstererek, sentez malzemesi olarak belirlenmiştir. Solvotermal sentez yöntemi ile sıcaklık ve Zn molar oranına göre üretilen Al/ZnO parçacıkların XRD, SEM-EDX yöntemleri ile yapısal analizleri gerçekleştirilmiş, malzeme doğrulanmıştır. Malzemeler, havacılık standartlarındaki poliüretan ile birleştirilip, malzeme kompozit haline getirilmiştir. İlk olarak, toz ve kompozit malzemelerin 8-14 μm FTIR spektrometresi soğurma ve yansıtma performansları incelenmiş, sonrasında UV-Vis spektrofotometresi ile malzemelerin görünür bölge yansıtma oranları araştırılmıştır. Toz malzemelerden %0.48 yansıtma oranına sahip alüminyuma en yakın performans gösteren %1.66 en düşük soğurma oranı ile 0.005 mol Zn oranına sahip ve 150 C reaksiyon sıcaklığı ile sentezlenen, pulcuk morfoloji içeren Al/ZnO çekirdek-kabuk malzeme, alüminyum plaka ve cam altıklara kaplanan kompozit formda da uyumlu sonuçlar vermiştir. Kompozit malzemelerin 60, 80 ve 100 C° sıcaklıklarda termal görüntüleme testleri yapılmış, 0.888 emisivite değerine sahip Al-bazlı malzemeye en yakın değeri 0.931 ile Al/ZnO kompozit vermiştir. Son olarak malzemenin ağırlıkça kompozit dolgu oranına göre emisivite oranındaki değişim incelenmiştir. Ağırlıkça 2/1 partikül/bağlayıcı oranındaki kompozit malzemelerden en düşük Al partiküllü 0.724, Al/ZnO partiküllü olan ise 0.805 emisivite değeri elde edilmiştir. Ayrıca, aynı dolgu oranındaki saf Al ve Al/ZnO bazlı kompozitlerden, çekirdek kabuk oranı artırıldığında, saf alüminyuma göre daha düşük emisivite değerinin elde edildiği kanıtlanmıştır. En düşük emisivite değerini veren kompozit malzemelerin X-band radar soğurma performansları incelenmiş, core/shell parçacığa sahip

kompozit malzemelerden, %51 ile alüminyum bazlı kaplamalara göre %10 düşük yansıtma oranı elde edilmiştir. Bu çalışmada, alüminyum partikül üzerinde büyütülen ZnO nanoparçacıkları ile, kızılötesi düşük emisivite partiküller üretilmiş, bunun yanında görünür bölge ve radar soğurma performansları alüminyuma göre iyileştirilmiştir. Sonuç olarak, görünmezlik teknolojisinin tüm gereksinimleri göz önüne alındığında, LWIR düşük radyasyon sağlamanın yanı sıra, çekirdek-kabuk yapıların radar ve görünür bölge düşük görünürlüğü karşılamak için umut verici malzemeler olduğu kanıtlanmıştır.

Anahtar Kelimeler: Kızılötesi Düşük Görünürlük Teknolojisi, Solvotermal Sentez, Düşük Emisivite Çekirdek-kabuk, FDTD metodu, Çoklu Bant Düşük Görünürlük

To my family,

ACKNOWLEDGMENTS

This study was supported by Turkish Aerospace Inc. within the scope of Scientific Research Projects Program.

First of all, I would like to express my deepest gratitude to my advisor Prof. Dr. H. Emrah Ünalan, for his support, patience and guidance throughout this study. I would like to express my gratitude to Prof. Dr. Alpan Bek, my co-advisor, for his guidance and support. I also like to express my sincere appreciation to Dr. Nursev Erdoğan, my industrial advisor, for her encouragement, support, and guidance.

I would like to thank Assoc. Prof. Dr. Simge Çınar Aygün and Assist. Prof. Dr. Şahin Coşkun for their guidance and positive approaches.

I would like to express my gratitude to my chief, Alper Madenoğlu for his friendly support and encouragement.

I would also like to thank my labmates Ceren Başköse, Doğa Doğanay, Mete Batuhan Durukan, Yusuf Tütel, Mustafa Caner Görür, Melih .g eday Çiçek, Onuralp Çakır, Onur Demircioğlu, Murathan Çuğunlular, Öykü Çetin, and Ali Deniz Uçar.

Finally, I want to express my gratitude to my family for their support, patience, and faith in me.

TABLE OF CONTENTS

LIST OF TABLES

TABLES

LIST OF FIGURES

FIGURES

CHAPTER 1

INTRODUCTION

In recent years, with the developments in wireless technologies, electromagnetic (EM) wave-based signal systems are used extensively for different purposes such as communicating, exchanging information, monitoring temperature and determining location. Various electronic systems are operating in the different portions of the electromagnetic spectrum from microwave to ultra-violet (UV) frequencies.

Especially in the aerospace and defense industry, the use of EM-based systems in critical missions has become an essential part of ensuring security. The systems such as sensors[1], radars[2], antennas[3], and jammers[4] provide intelligence, communication, and tracing capabilities to armed services. One of the major objectives of the EM wave-based technology in military aerospace is detecting, tracing, and counteracting the jet fighter before or during its operation by the assault systems such as radar and IR wave-based surveillance systems[5].

Ever-growing platforms in the military air such as helicopters, unmanned air vehicles (UAV), warplanes, and missiles provide strategic supremacy over all other systems. Among military air systems, fighter jets with superior features such as supersonic speed, high maneuverability, and improved avionic and assault systems, are the most advanced air vehicles in the defense industry[6,7]. In addition to the unique mechanical, aerodynamic, and avionic characteristics of fighter jets, with the development of 4^{th}-generation, the low-observable specialty has emerged as a distinctive function to perform jet aircraft's operations by reducing the signal without being identified, engaged, or assaulted. The concept of stealth technology has come to the fore in the 5^{th} -generation warplanes utilized in current operations, in response to fast emerging anti-stealth threats[7,8].

Infrared (IR) stealth technology is one of the key low-observable approaches created to lower the generated radiation against guidance kits, infrared search and track systems, and thermal camera systems that trace the radiation emitted by the air platform in the infrared wavelength range. Fifth-generation jet fighters among advanced air platforms are one of the critical systems in which this technology is used[9].

Principally, when the surface temperature of the aircraft rises due to internal heat-generating parts, aerodynamic friction, and light interaction with external sources during operation, the aircraft radiates thermal energy from various regions of the body as electromagnetic waves in the IR spectrum. The EM waves emitted from the surface generate the air platform's IR signature, which is recognized by IR surveillance. Reducing the IR signature of the body makes traceability difficult and is referred to as IR-stealth technology[10].

Infrared wave-based detection covers mid-wave infrared (MWIR, 3-5 μm) and long-wave infrared (LWIR, 8-14 μm) wavebands since the tracking is held in these ranges. The acceleration of the LWIR-based search and tracking system advancements and challenges on misguiding strategies have triggered the LWIR signal reduction efforts[11]. LWIR stealth technology for fighter jet air platforms is developed by the solution of multidisciplinary engineering research. This technology is strongly depending on the optical and electromagnetic properties of the material, which is used for reducing IR-wave radiation. Material science and engineering-based studies have a significant role in the improvement of IR less-visible structures [12].

Infrared low-observable advancement based on material science and engineering can be achieved by coating or painting structures on the surface of the object to be detected. In recent years, the number of coating/painting studies that target to impart low infrared radiation to the platform surface have increased[13].

In the literature, there are various types of material developments such as thin films[14], metamaterials[15], photonic crystals[16,17], nanocomposites[18] and polymer-matrixed composite materials with metallic[19–22], pure and doped metal oxide[23,24], core/shell[25] and composite pigments[26]. The common practice for LWIR stealth materials is particle-embedded polymer-matrix composite coating/painting materials. This is primarily because of the advantages of large-scale synthesis and application convenience to wide and complex-shaped areas. The critical component of the composite materials is the micro-particles dispersed in the polymer binder. These particles allow the composite to have a low emissivity of LWIR radiation. While serving as a binder, polymer also determines the mechanical properties of the composite [27].

1.1 Stealth Technology

In military aviation, stealth technology can be defined as having low observable characteristics of air platforms versus any type of seeker during its operation. The purpose of this advancement is to conceal the airborne from countermeasure systems. The technology can be achieved by suppressing the aircraft signals or creating deceptive signals with various techniques in the EM-wave bands in which surveillance systems are operated [28,29].

In aerospace and defense, fighter jets have become the ultimate power of the armed forces since their first utilization in the operation due to their outstanding performance. On the other hand, the development and evolution of EM-wave-based surveillance systems such as radar and IR-detection have weakened the power of air vehicles by detecting and destroying them and can cause a massive collapse in the fleet. This situation has revealed the demand for stealth technology in air power. The use of stealth technology in warplanes has caused dramatic reduction in aircraft collapse[30,31].

The stealth technology was officially used on the first F-117A and B-2 fighter jets in the late 1980s. With the F-22, which made its first flight in 1997, stealth technology has become an essential feature in the design and production of all 5th -generation aircraft deployed, produced, and developed today[29,32,33].

The radar was the prior system utilized in the possible combat area for detection, yet discovering and taking advantage of weaknesses of radars such as being jammed[34], radar cross-section reduction of the platform[35], and radar absorbing materials development[36] prompted the industry to concentrate on the development of IR-based tracking systems. IR-based seeking and targeting have substantial advantages over typical radar systems, such as passive operation, resistance to jamming, and large detection ranges. Therefore, IR-stealth aircraft has garnered interest in the last decades compared to radar camouflage[37,38].

1.1.1 Aircraft Infrared Radiation

Modern 5th-generation fighter jets are the strongest systems in military aviation compared to other air platforms by means of multirole characteristics such as high agility, high speed over Mach-2, advanced avionic systems, and superior counter-attack integrations. Furthermore, they can carry the payload inside the body and operate in a variety of atmospheric conditions by maintaining completely stealthy features[7,39,40].

During operation, the temperature of certain regions on the fuselage rises resulting in thermal radiation from the surface of the body. The major heated areas on the airframe are the nose zone, leading edges, and nozzle inlets. On the rear side, the tailpipe and plume are the most radiated regions[31,41]. Hot and radiated regions of the aircraft are shown in Figure 1.1.

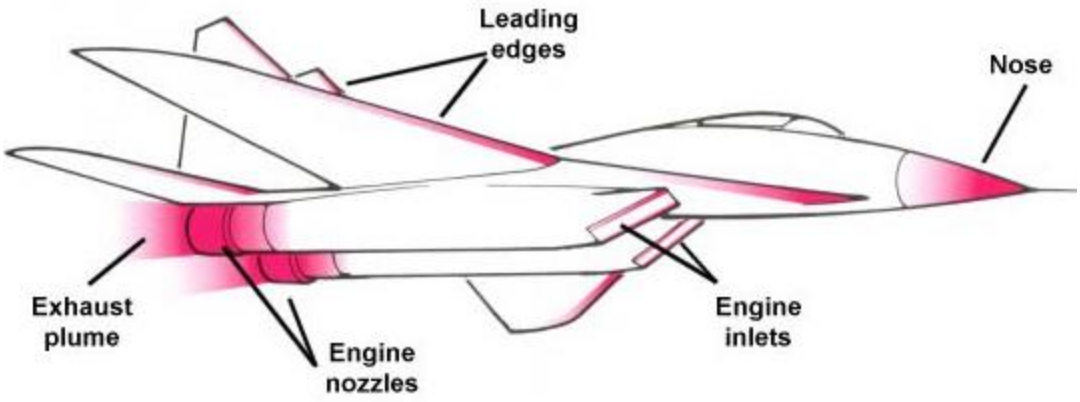

Figure 1.1 Heated and radiated regions in an aircraft[42].

The airframe zones are mainly heated by aerodynamic friction, especially at high speeds, and irrelevant from aerodynamic effects. Heat generation in the engine results in infrared radiation from the rear region of the aircraft. Reflected light from the sky, sun and ground surface also contributes to heat the aircraft. The thermal radiation from the aircraft is classified as a passive signature in terminology. The reasons for the radiation of the air jet with radiating areas are shown in Figure 1.2[31,43].

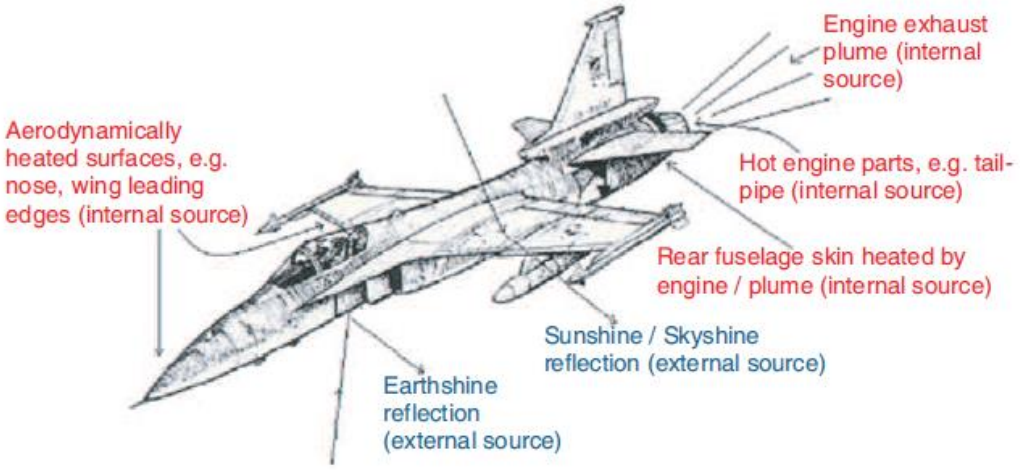

Figure 1.2 Heated regions and the reasons for the radiation of the aircraft[31].

The radiation occurs on the airframe in long-wave infrared (8-12 μm) bands at relatively low temperatures, and the hottest regions radiate in the MWIR wavelengths. The reason for this specific wave range is that the atmosphere transmits IR waves in the specified bands[44,45].

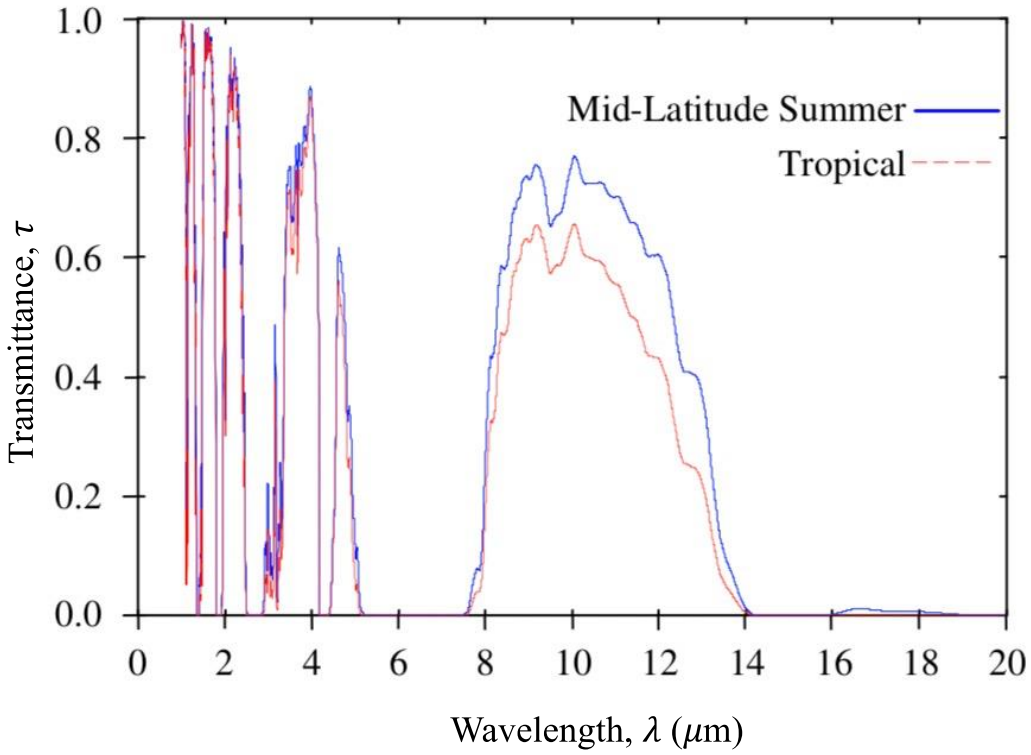

Figure 1.3 Spectral atmospheric transmittance[45]

Atmospheric transmittance in mid-latitude summer and tropical conditions between 0.2-20 μm is shown in Figure 1.3. According to the graph, between the 8-14 μm region the atmosphere has a broad and clear transmission region in both conditions. Although the atmosphere has lots of needle-like transmittance peaks in the MWIR range, the waves can transmit in the 3-5 μm band[38,45].

1.1.2 Surveillance Systems

In military applications; observation, detection, and tracing of possible threats provide a significant advantage to formulate a prior strategy in advance against hostile attacks and intelligence actions. Advanced observation technologies work on the basis of detecting and converting EM waves in a specific wave-band range emitted from the object to be positioned. As an advanced technology, radar (radio detection and ranging) and IR-based surveillance systems have been utilized for this purpose in defense[46].

Radar-based tracing and detecting systems are formulated by sending constant and specific frequency electromagnetic signals in radio-frequency bands and receiving them that are reflected from the body. In the modern aerospace industry, this allows to determine the size, movement speed and direction of the object[47].

IR-range tracking systems can be considered as the eyes which can see in the infrared wave ranges. During the operation of the fighter jet, the contrast occurs in the infrared wavebands between the aircraft and the environment or atmosphere because of the IR signatures of the air vehicle. Infrared detection systems work on the principle of detecting thermal contrast differences between the background and the target. Once the target is determined, the system locks on the object to trace and destroy[30].

In the last half-century, the priority in the air platforms has been given to IR tracking systems for protection from hostile air-defense systems. Modern IR radiation-seeking systems are advanced as technological devices that can detect a temperature difference of 0.1 °C between the object and the environment[48].

Infrared surveillance systems are mainly focused on the MWIR and LWIR wavelength ranges with the types of infrared homing missiles and infrared search and track systems (IRST). MWIR-based systems trace the rear fuselage and plume, while LWIR-based seekers target the airframe skin of the airborne[49]. While the

main purpose of guided air-to-air and ground-to-air fire-and-forget missiles is engaging the target to strike, the intended use of IRST is detecting and tracing the object[50]. IRST systems have become more significant than infrared homing missiles and radar technology because they are not affected by jammers, or do not initiate the alarm systems of the target[51,52].

1.1.3 Infrared Stealth Technology

Infrared radiation is passively emitted from the surface of the target due to the its relatively higher temperature compared to the background. The operating wavelength range of the detectors is restricted by MWIR and LWIR wavebands because of the atmospheric windows that are discussed in Chapter 3.2. As surveillance systems, homing guidance kits are engaged in MWIR radiation, and IRST systems are focused on LWIR radiation[53].

Infrared stealth is a technology that imparts low-observable features to the airborne against infrared detection by misleading the countermeasure systems or suppressing the infrared radiation of the surface. At the infrared wavelengths, the platform cannot be completely invisible, the signal is tried to be reduced as much as possible[28,29,40].

The significance of the IR stealth has been realized since the significant amount of aircraft loss was happened the in the 1970s by the IR-seeker-domed missiles. The prior integration of the IR-stealth features on the aircraft has performed to reconnaissance jet of SR-71 Blackbird. The rapid evolution of detecting systems has promoted IR-stealth advancements[54].

IR stealth in the air vehicle can be achieved by two methods such as passive and active stealth. Active stealth is implemented with flare launch from aircraft as a decoy to IR-seeking missiles and IR-jamming operations. Active deception is more effective on helicopters than on fighter jets[55,56]. Passive concealment is obtained by re-designing aircraft based on characteristic stealth concerns, and covering parts such

as engine intakes and outlets, or by embedding the engine into the body. Another method is to reduce the temperature of the hottest areas with the cooling pipes in the body and to paint or cover the surface with IR-stealth materials[57,58].

The coating and painting strategy is mainly focused on reducing aircraft passive radiation in the infrared waveband by providing surface reflectivity in a related wavelength range[59].

CHAPTER 2

MOTIVATION, NOVELTY AND STRATEGY

The original design and development of infrared stealth materials is a much-needed improvement for aircraft with low all-round observability. While providing infrared stealth features, low observability in visible and radar bands should be considered, the improved material should not weaken radar absorbance operations and should contribute to visible camouflage. Moreover, the material should be resistant to extreme conditions such as high temperatures and corrosive environments and should keep performance at a high and stable level in terms of infrared low radiation features. The desired characteristics of the material are, high reflectivity in infrared, low reflectivity in visible and radar regions. When the low-observability requirements for the stealth fighter are taken into consideration in all regions such as radar, visible and infrared ranges, it has been decided that the composites containing core/shell fillers are the most compatible structures. Core/shell structures have relatively high chemical and structural resistance and provide low observable features in the visible and radar ranges. The expected features and the concept design of the infrared stealth material are schematically illustrated in Figure 2.1.

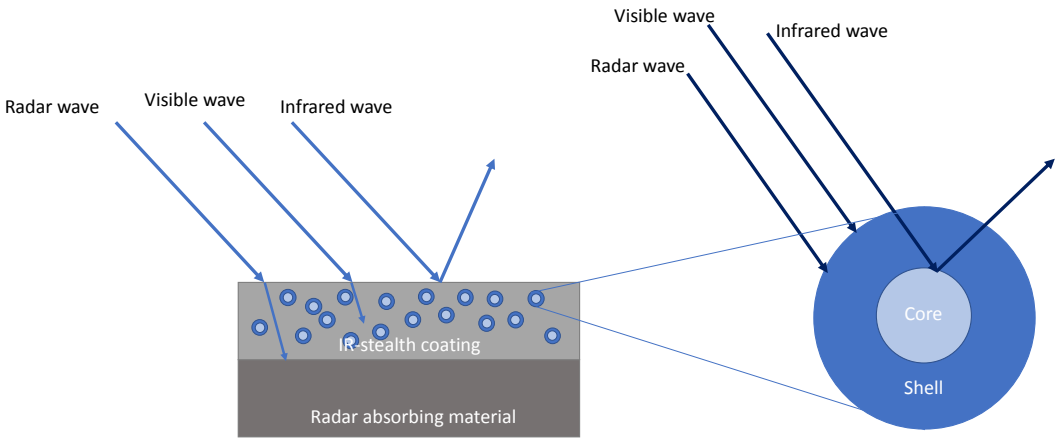

Figure 2.1 Schematic illustration of concept design of coating material and desired characteristics of the core/shell structure.

There is limited research in the literature as it is a very important technology due to the defense concerns of the countries. In the present research, LWIR low-observable materials in terms of types, structures, optical, electromagnetic, and infrared radiation properties have been investigated. Core/shell particle-embedded polymer-matrix composites have been fabricated and their use in IR stealth technology has been researched. Type, size, and structure of the core/shell particles due to their strong effect on the LWIR radiation caharacteristics of the final composite material is investigated in detail.

Although there are several studies on this subject from a materials science and engineering perspective, Al/ZnO core/shell material has been investigated for the first time with this research. Moreover, the core/shell materials in the literature have not been examined within the polymer matrix in terms of infrared radiation, visible and radar absorbing features. In addition, the literature has not covered the electromagnetic absorbance/reflectance analysis via simulation software as a determination method for the core/shell material in this subject.

Throughout the thesis, theoretical background as a scientific approach for the development of the LWIR stealth material has been described in following chapter. In Chapter 4, a literature survey on the LWIR low-observable methods and materials

has been stated and candidate materials have been determined. Chapter 5 covers the description of the Finite-Difference Time-Domain (FDTD) analysis method, analyzing of candidate materials from the point of electromagnetic behaviors in the LWIR range, and determination of main material with specified parameters. In Chapter 6, details of the experimental procedure is provided. In Chapter 7, the experimental results are evaluated. The conclusions and the future recommendations are provided in Chapter 8.

CHAPTER 3

THEORETICAL BACKGROUND

In this chapter, the fundamentals of IR radiation are discussed. As mentioned in Chapter 2, IR radiation of aircraft is occurring because of the heating effects and interaction with external radiation sources. This chapter describes the mechanisms of IR radiation caused by the increase in temperature and interaction with EM wave of the material.

3.1 Electromagnetic Wave

An electromagnetic wave is a phenomenon that is the time-varying continuation of the electric and magnetic fields, which are perpendicular to each other, with synchronized oscillation in a certain frequency or wavelength[60]. A time-varying one-dimensional propagating electromagnetic wave is illustrated in Figure 3.1. *E* stands for electric field intensity and *H* is representing the magnetic field directions.

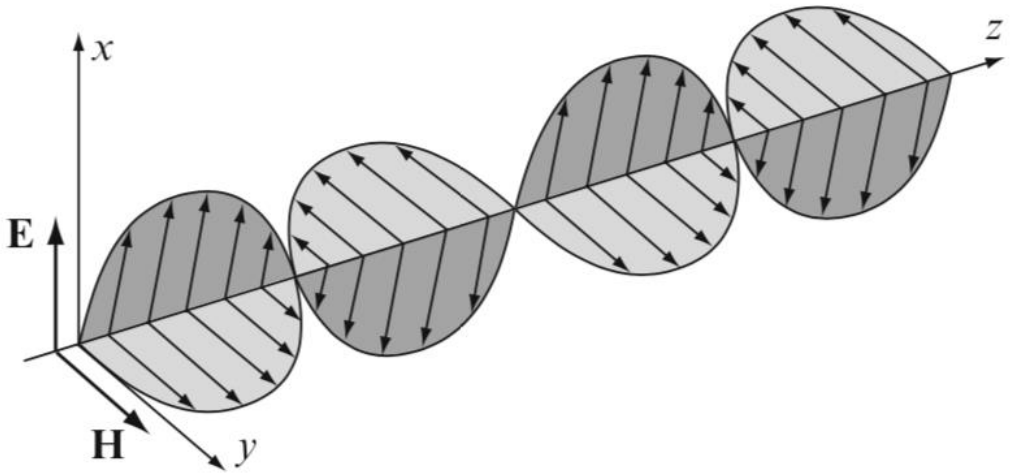

Figure 3.1 Schematic illustration of spatial electromagnetic wave propagation in the *z*-direction, electric field intensity oscillation in *x*, and magnetic field intensity oscillation in *y*-direction[61].

The electromagnetic theory in the macroscopic scale has embodied by James Clerk Maxwell in 1861, and the electromagnetic wave equation has been revealed. The electromagnetic wave equation has been obtained by a combination of electricity and magnetism laws of Gauss, Ampere and Faraday, which are called Maxwell's equations[61,62]. The representative electromagnetic wave equation obtained by derivation of Maxwell's equations is expressed in Equation 3.1[63].

$$\frac{\partial^2 \mathrm{u}}{\partial \mathrm{t}^2} = \mathrm{v}^2 \frac{\partial^2 \mathrm{u}}{\partial \mathrm{z}^2} \tag{3.1}$$

In the equation, *u*, *v*, and *t* are representing the field vector, speed of wave and time, respectively. The wave is propagating in the *z*-direction; hence *z* stands for the variable in the specified direction. In order to obtain electric and magnetic fields; the equation can be changed by superseding magnetic field intensity (H) and electric field intensity (E) by *u*. When the equation is solved for the electric field, the linear electromagnetic plane wave propagating in the *z*-direction, and the electric field vector in the *x*-direction at a particular space and time can be summarized as in Equation 3.2 by the solution of the wave equation[63]. Equation 3.3 shows that the wave number is the function of angular frequency, permittivity, and permeability[64].

$$E_x(z,t) = E_0 \cos(kz - \omega t + \phi) \tag{3.2}$$

$$k = \omega\sqrt{\mu\epsilon} \tag{3.3}$$

, where the E_x stands for the electric field intensity oscillating in x-direction (V/m), E_0 represents constant electric field intensity (V/m), k is wave number, ω denotes angular frequency (rad/s), ϕ is phase angle (rad), μ and ϵ are permeability ($C^2\ N^{-1}\ m^{-2}$) and permittivity ($N\ A^{-2}$) of the medium, respectively.

The distance between two peaks of the waves is defined as wavelength, and the ray moves at a certain frequency. Wavelength and frequency are inversely proportional to each other. Angular frequency, speed of a wave, and wavelength relations are given in Equations 3.4 and 3.5. A schematic illustration of a plane wave with a certain velocity and wavelength is shown in Figure 3.2[63].

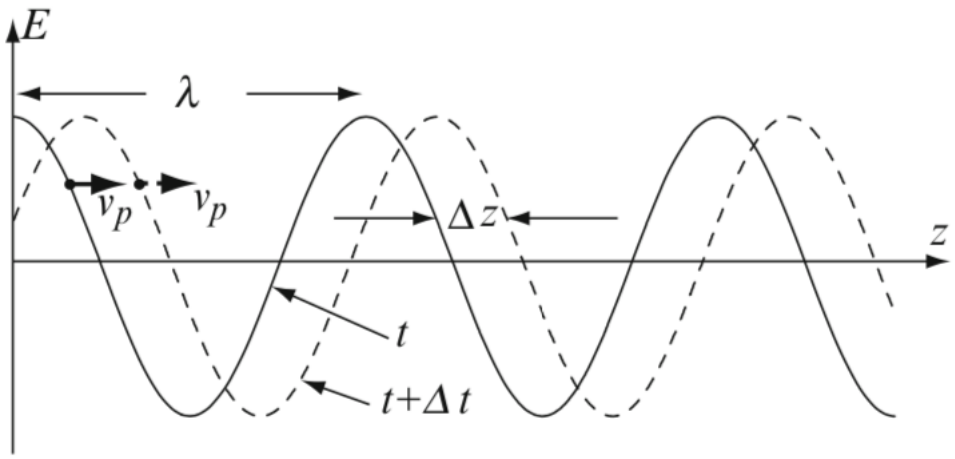

Figure 3.2 Schematic illustration of wavelength and speed of electromagnetic wave[63].

$$\omega = \frac{2\pi v}{\lambda} \tag{3.4}$$

$$\lambda = \frac{v}{f} \tag{3.5}$$

Electric and magnetic field intensities are proportional to each other, and the ratio is defined as wave impedance in a medium. The wave impedance is a function of permittivity and permeability of the medium, through which the wave propagates. The relationship between electric and magnetic field intensities and the wave impedance in a medium are given in Equation 3.6 and 3.7[65].

$$H_y(z,t) = \frac{k}{\omega\mu} E_x(z,t) \tag{3.6}$$

$$\frac{E_x}{H_y} = \frac{\omega\mu}{k} = \sqrt{\frac{\mu}{\epsilon}} = \eta \tag{3.7}$$

In the equations, v is the speed of the wave (m/s), λ represents wavelength (m), H_y is magnetic field intensity oscillating in the y-direction (A/m) and η represents the wave impedance (Ω).

The expression of the speed of an electromagnetic wave propagating in vacuum has been discovered by wave equations. The speed of an electromagnetic wave is proportional to permeability and permittivity, which is given in Equation 3.8[64].

$$v = \frac{1}{\sqrt{\mu\epsilon}} \tag{3.8}$$

In this case, the speed of the wave in the vacuum can be expressed as in Equation 3.9[64].

$$c = \frac{1}{\sqrt{\mu_0\epsilon_0}} \tag{3.9}$$

,where c (speed of light in free space), ϵ_0 (permittivity of free space) and, μ_0 (permeability of free space) are 2.998×10^8 m/s, 8.8542×10^{-12} $C^2N^{-1}m^{-2}$ and $4\pi \times 10^{-7}$ NA^{-2}, respectively.

3.1.1 Light and Matter Interactions

The refractive index of any object is described as the ratio of the speed of the ray in free space to the speed of the light in the material. The speed of the wave in the free space is discussed in Equation 3.9. The refractive index equation, which is obtained by derivation of the speed of light equation, is given in Equation 3.10[66].

$$n = \frac{c}{v} = \sqrt{\frac{\mu\epsilon}{\mu_0\epsilon_0}} \tag{3.10}$$

In this equation, *n* represents the refractive index.

The interaction of the electromagnetic wave with a matter cause some of the beam to be diffracted and some to be reflected. Fresnel explained the reflectance and transmittance intensity ratios per incident wave intensity at the boundary surface of an object and the incident wave medium. The Fresnel equations employ the wave impedance or refractive index and wave vector parameters to compute reflection and transmission magnitudes of main radiation[65]. The equations have originated for S-polarized and P-polarized types of plane waves. Basically, while the E-field vector of the S-Polarized wave is perpendicular to the plane of incidence, the E-field vector of the P-polarized wave is parallel to the irradiation plane. Schematic illustrations of S-polarized and P-polarized electromagnetic waves are given in Figure 3.3 a and b, respectively[67].

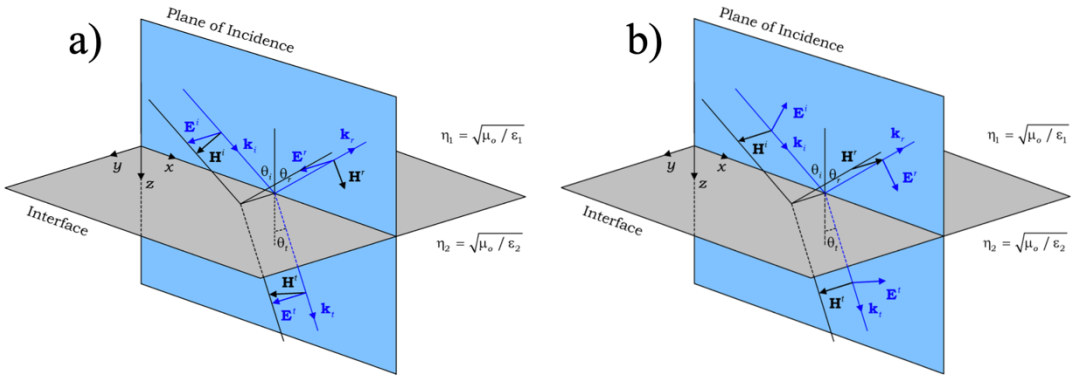

Figure 3.3 Schematic illustration of; (a) S-polarized plane wave and (b) P-polarized plane wave at the boundary of dielectric mediums. (For incident wave; θ_i incident angle with normal P_i incident wave vector, E_i incident electric field vector, H_i incident magnetic field vector[68]

The reflection coefficient can be calculated by Fresnel equations for dielectric media depending on the refractive indexes of the mediums and wave angles, which are given in Equations 3.11 and 3.12[63,68].

$$r_{S-polarized} = \frac{\eta_2 \cos\theta_i - \eta_1 \cos\theta_t}{\eta_2 \cos\theta_i + \eta_1 \cos\theta_t} \tag{3.11}$$

$$r_{P-polarized} = \frac{\eta_2 \cos\theta_i - \eta_1 \cos\theta_t}{\eta_2 \cos\theta_i + \eta_1 \cos\theta_t} \tag{3.12}$$

When the wave impinges perpendicularly to the matter, some portion of the ray transmits through the material by incident angle and the remaining reflects back at a steep angle, which is illustrated in Figure 3.4[67].

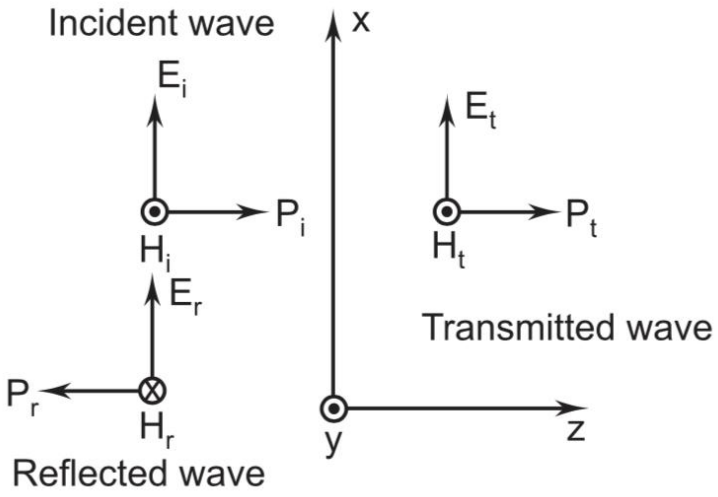

Figure 3.4 Schematic illustration of plane wave at a steep angle at the boundary of dielectric medium[67]

At a steep angle, the reflectance and transmittance do not depend on electric and magnetic field directions. In these circumstances, since $\cos\theta_i = \cos\theta_t = 1$ at normal incidence, the reflectance can be calculated as a function of the refractive index, which is expressed in Equation 3.13[63].

$$r_{perpendicullar} = \frac{\eta_2 - \eta_1}{\eta_2 + \eta_1} \tag{3.13}$$

The magnetic flux density is a function of magnetic field intensity and permeability, which is given in Equation 3.14[63]. The ratio of electric field intensity to magnetic flux density gives the speed of the wave, which is expressed in Equation 3.15[68]. When the equation is resolved with magnetic flux density instead of magnetic field intensity, refractive index (n) takes place in which, the related function is given in Equation 3.16. The Fresnel equations with magnetic flux density are simplified as Equations 3.17, 3.18, and 3.19, the reflection coefficient depends on the refractive indices of adjacent mediums through which the light moves[69].

$$B = \mu H \tag{3.14}$$

$$\frac{E_x}{B_y} = \frac{1}{\sqrt{\mu\epsilon}} = v \tag{3.15}$$

$$B_y = \frac{E_x n}{c} \tag{3.16}$$

$$r_{S-polarized} = \frac{n_1 \cos\theta_i - n_2 \cos\theta_t}{n_1 \cos\theta_i + n_2 \cos\theta_t} \tag{3.17}$$

$$r_{P-polarized} = \frac{n_1 \cos\theta_t - n_2 \cos\theta_i}{n_1 \cos\theta_i + n_2 \cos\theta_t} \tag{3.18}$$

$$r_{perpendicullar} = \frac{n_1 - n_2}{n_1 + n_2} \tag{3.19}$$

B represents the magnetic flux density (T) in the Equation 3.14.

The intensity or power of the reflected electromagnetic wave is a function of the reflection coefficient, which is given in Equation 3.20[69,70].

$$R = r^2 \tag{3.20}$$

3.2 Electromagnetic Spectrum

In 1900, the electromagnetic radiation theory, which is electromagnetic energy emitted from a radiator, has discovered by Planck. According to Planck, electromagnetic radiation carries distinct groups of radiant energy emitted from an object. According to the explanation, the radiation consists of photons, which are defined as the unit energy carrier particles of the wave[64,71,72]. The photon energy is given by Equation 3.21[61].

$$E_{photon} = \frac{hc}{\lambda} \tag{3.21}$$

In the equation, E_{photon} and h stands for the photon energy, and Planck constant (6.62×10^{-34} m^2kg/s), respectively.

According to Equation 3.21, the energy of a photon is dependent on its wavelength. The electromagnetic spectrum has been developed depending on wave energy and the frequency or wavelength relation of a photon and it demonstrates the distribution of electromagnetic waves regarding photon energy[73].

Electromagnetic waves are generated in various wavelengths or frequencies which affect the EM wave energy as described in Planck's formula. The distribution of electromagnetic waves based on their wavelength or matched frequency is designated in the electromagnetic spectrum which is provided in Figure 3.5.

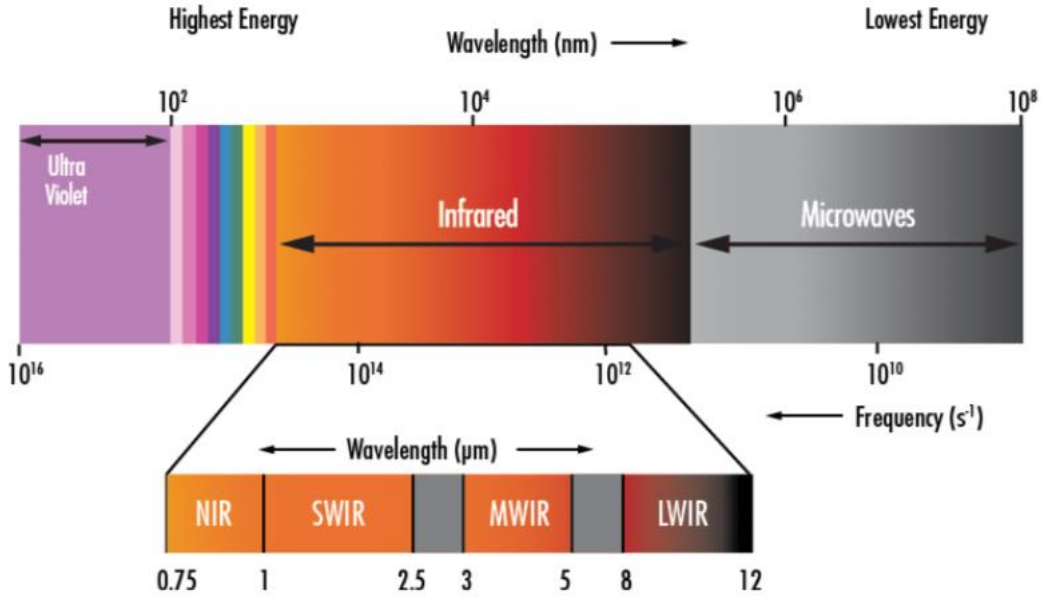

Figure 3.5 Electromagnetic Spectrum[74].

The infrared region in the electromagnetic spectrum extends from 700 nm to 1 mm wavelength. In the infrared ranges, 3-5 μm corresponds to MWIR, and 8-14 μm corresponds to LWIR, which are the tracing bands for detectors to detect air vehicles [72,74].

3.3 Infrared Radiation

Any object with a temperature higher than 0 K (-273.15 °C) emits infrared radiation. As a theoretical definition, an ideal black body is one that absorbs all incident radiation and emits all the energy it theoretically absorbs as radiation. A real or gray body is incapable of absorbing the electromagnetic wave completely, thus it is insufficient to radiate all the energy to which it is exposed[75,76].

3.3.1 Emissivity

Emissivity is the ratio of the radiation emitted by an object at a certain temperature to the radiation emitted by a black body at the same temperature. The emissivity value of the black body at all temperatures is accepted as 1. The emissivity value of each material is in the range of 0 to 1. This value changes depending on the material type, shape, size, surface condition, temperature and refractive index, and wavelength of the radiation [76].

According to the principle of conservation of energy and Kirchhoff's law, the magnitude of incident energy upon the surface equals to sum of transmission, reflection, and absorption energy rates from the surface. The related equation is provided below in Equation 3.22[76,77].

$$\frac{I_A}{I_0} + \frac{I_R}{I_0} + \frac{I_T}{I_0} = 1 \tag{3.22}$$

I_A, I_R and I_T are the absorbed, reflected, and transmitted wave intensities, respectively.

Kirchhoff's Law, which is obtained by the derivation of Planck's Law, states that the material emits as much radiation as it absorbs, for opaque materials at related wavelengths, transmission is negligible or accepted as 0. In this case, the absorbance

of a material equals emissivity. The relationship between absorbance and emissivity is expressed below in Equation 3.23[78].

$$\varepsilon = A = 1 - R \tag{3.23}$$

, where ε is emissivity, A is the absorbance of the object (I_A/I_0), E_{RB} and E_{BB} are radiation of the real body and blackbody, respectively. The emissivity is the ratio of the radiated energy from the ideal gray body to the blackbody, as given in Equation 3.24[78].

$$\varepsilon = E_{RB} / E_{BB} \tag{3.24}$$

3.3.2 Planck's Law

Planck's radiation formula describes the power emitted by the unit area of the blackbody depending on its wavelength and temperature. The radiation energy can be calculated at a given temperature and wavelength. Planck's formula for spectral radiance per unit area in blackbody is shown in Equation 3.25, and the spectral exitance between two wavelengths is expressed in Equation 3.26. The radiated power depending on wavelength and temperature is provided in Figure 3.6 [79].

$$dR(\lambda, T) = \frac{2\pi hc^2\lambda^{-5}}{\exp\left(hc/\lambda kT\right) - 1} \tag{3.25}$$

$$R_{\lambda a}^{\lambda b} = \int_{\lambda a}^{\lambda b} \frac{dR(\lambda, T)}{d\lambda} d\lambda \tag{3.26}$$

$dR(\lambda, T)$ represents the power emitted per unit area at a specified temperature and wavelength, k is Boltzmann's constant (1.38×10^{-23} J/K) and T is the temperature (K).

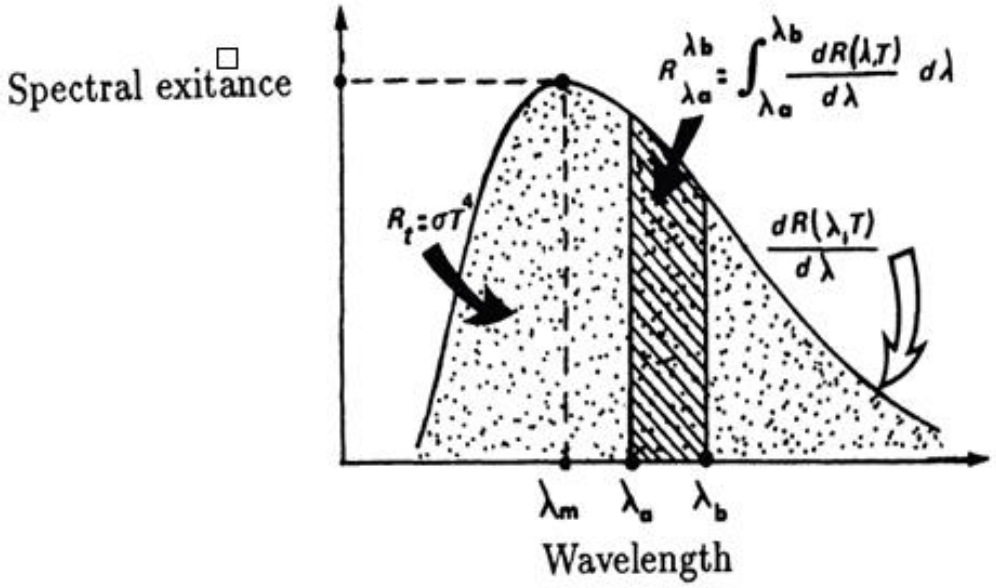

Figure 3.6 Infrared radiation diagram according to Planck's Law[77]

3.3.3 Wien's Displacement Law

Wien has stated that the radiated energy from a blackbody is formed in a curvature as a function of wavelength at certain temperatures. When the temperature of the object increases the curve peak becomes narrower and sharper. In Figure 3.7, the spectral distribution of radiation energy and displacement of curves in terms of peak wavelength depending on temperature is provided[80].

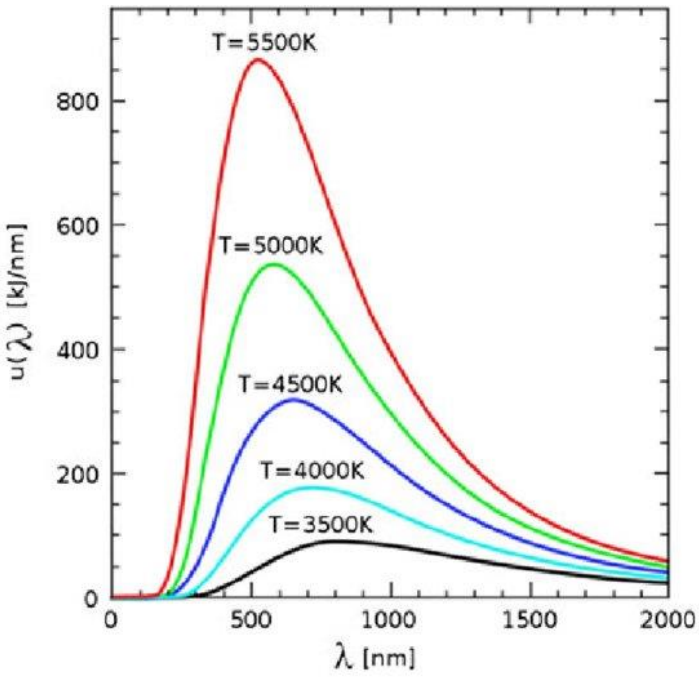

Figure 3.7 Wien Displacement Diagram (radiated energy vs wavelength at specified temperatures)[80].

Wien's Displacement equation is provided in Equation 3.27[80].

$$\lambda_{max} T = b \tag{3.27}$$

, where b is Wien's constant (2898 μm K) and λ_{max} is peak wavelength.

According to the formula, the wavelength of radiation at the maximum energy is inversely correlated with temperature. The peak wavelength of the radiation can be obtained depending on the temperature.

3.3.4 Stefan-Boltzmann Law

The Stefan-Boltzmann law is obtained through derivation from Planck's radiation law. It states that the total radiation energy emitted from the unit area increases with the temperature of the material regardless of the wavelength. It is directly

proportional to the emissivity value. Material with lower emissivity will have lower radiated energy[81].

Stefan-Boltzmann formula, provided in Equation 3.28, gives the total radiation energy emitted from the unit surface area [81].

$$E_t = \sigma \varepsilon T^4 \tag{3.28}$$

, where, E_t represents total radiated energy emitted per unit area and σ is Stefan-Boltzmann constant (5.67×10^{-8} W.m^{-2}.K^{-4}).

The emissivity of the material plays a significant role in infrared radiation characteristics at any temperature when considering the theoretical laws discussed in this chapter. The emissivity of the object is dependent on the energy that the object absorbs whether it is in the form of electromagnetic wave or heat. The thermal emissivity and EM absorbance capability of the sample will be evaluated separately to simulate the light-caused and the heat-caused radiation of the aircraft.

CHAPTER 4

LITERATURE RESEARCH

IR low-emissivity materials were investigated for the purpose of determining the candidate materials for emissivity analysis via FDTD. The different type of materials such as nanoparticles, microparticles, composite coatings with metal, metal oxide particles and photonic crystals were investigated during research.

4.1 Metallic Pigments

The use of metallic pigments in coatings provides optical and electronic advantages to materials, especially due to their high reflectivity and electrical conductivity [82]. Aluminum is the most common material that is used as a particle in a polymeric binder for IR low emissivity studies due to its high reflectivity, low cost, lightweight, processability and abundance [83].

Yuan et al.[84] investigated the change in infrared emissivity of a composite coating based on the shape, size, and loading ratio of Al pigment material distributed in an epoxy resin, and coated on tiplate substrate. The FTIR spectrometer was used to assess LWIR emissivity performance. SEM images of low content and high content composite coatings is provided in Figure 4.1 (a), (b).

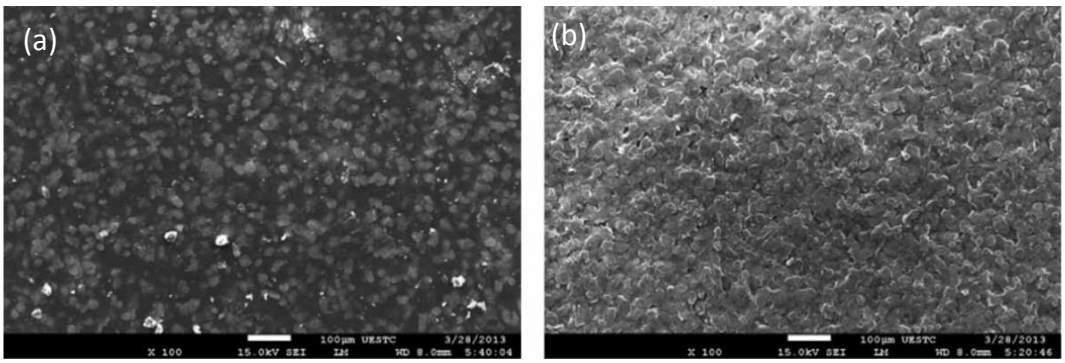

Figure 4.1 SEM images of coatings with (a) low-content, (b) high-content particles [84].

As seen in Figures 4.1 (a) and (b), the high-content coating formed an Al-densed surface, which caused high reflection, as stated. Change in emissivity of the composite with respect to particle size and particle loading ratio is illustrated in Figure 4.2.

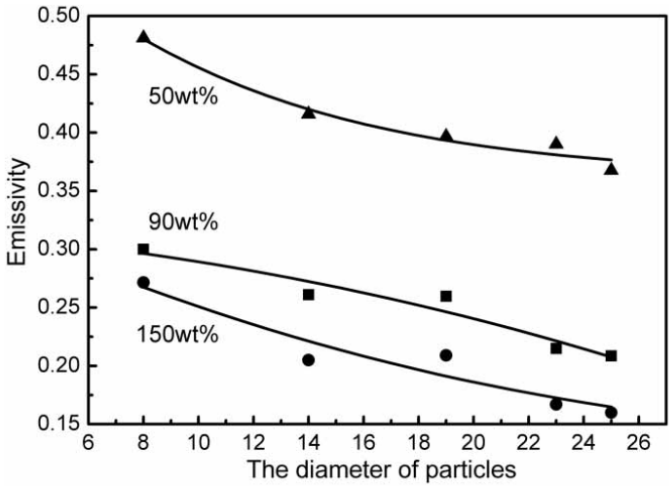

Figure 4.2 IR emissivity of coatings depending on particle size and particle loading ratio [84].

The results showed that the flaky-structured, 25 μm sized Al pigments had a minimum emissivity value of 0.16. The large-sized flaky structure and high-content ratio of Al pigments altered surface morphology and minimized roughness, which was explained as the cause of low infrared radiation.

Yu et al.[85] studied infrared emissivity and thermal stability of Al/polysiloxane composite paint. The material was synthesized by pre-treatment of Al particles by ball-mill, mixing with polysiloxane by ultrasonication, and coating on a tin substrate by spraying. The effect of particle content from 10 to 40 wt. % was investigated. Solidification temperature of the composite coating was between 150 and 450 °C and the thickness of the coatings was arranged between 20-70 μm. Effects of thickness, loading ratio, and surface morphology on infrared emissivity were systematically investigated. FTIR and IR-2 Emissometer were utilized for LWIR emissivity measurement, and the morphology of the material was observed by SEM. Figure 4.3 (a)-(d) show the SEM images of coatings with between 10% and 40% Al-content.

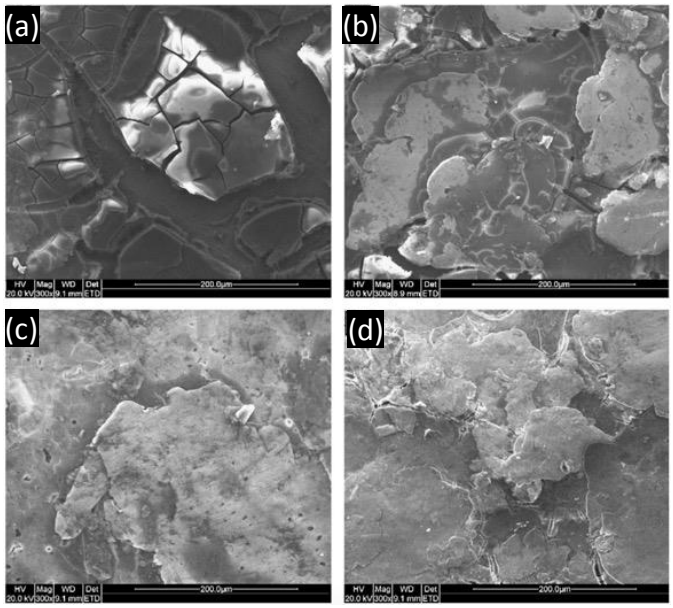

Figure 4.3 SEM images of composite coatings with (a) 10%, (b) 20%, (c) 30%, (d) 40% wt. Al-content [85].

As seen in the Figure 4.3, cracking was formed in 10% wt. content. In 20% particle loaded composite, particles overlapped. The coating with 30% wt. particle content had more smooth and coherent structure, when the content ratio increased to 40% wt., non-uniform structure was observed. The material with an Al content of 30 wt. % had the lowest emissivity, which also had the smoothest surface. The emissivity

was found to decrease with increasing temperature. As a result, the minimum emissivity value of 0.19 was obtained.

Yu et al.[86] have studied the infrared emissivity performance of Cu/EPDM (Ethylene-Propylene-Diene Monomer) composite coatings depending on particle shape, size, floating ability, and loading ratio into the binder. Cu pigments with sample sizes of 50 μm, 4 μm, 2 μm, 0.4 μm and in spherical, cubic and flake structures were investigated. The particle contents in the EPDM were prepared as 20, 30, 40, and 50 wt. %. Sputtering was used to deposit composites onto a tin substrate, with a 50 μm thickness. LWIR infrared emissivity was measured via IR-2 Infrared Emissometer device, and structural and chemical characterizations were performed via SEM and FTIR. The SEM images of composite films with leafing and non-leafing Cu partlices are provided in Figure 4.4 (a) and (b), respectively.

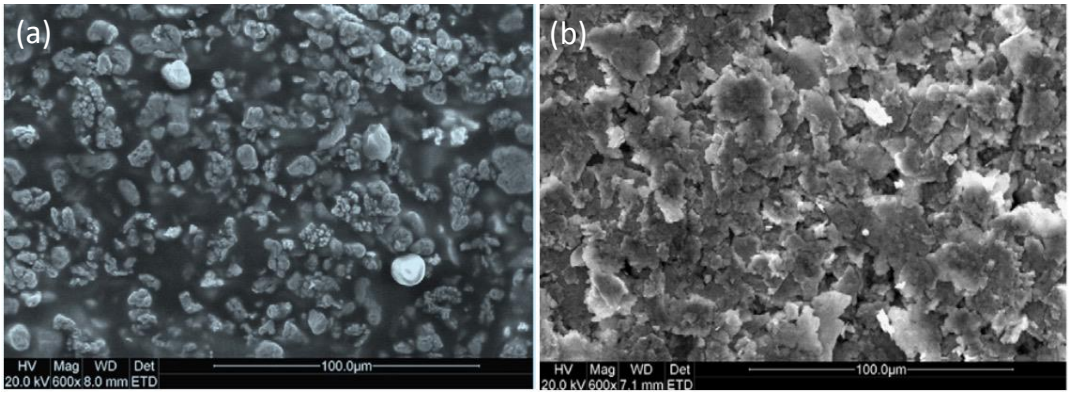

Figure 4.4 SEM images of composites with (a) non-leafing flaky-shaped, (b) leafing flaky-shaped particles[86].

As seen in the Figure 4.4, with non-leafing particles, the binder filled the gaps between particles, however, leafing structure formed more dense surface. The filler-content and leafing feature-dependence emissivity change is illustrated in Figure 4.5.

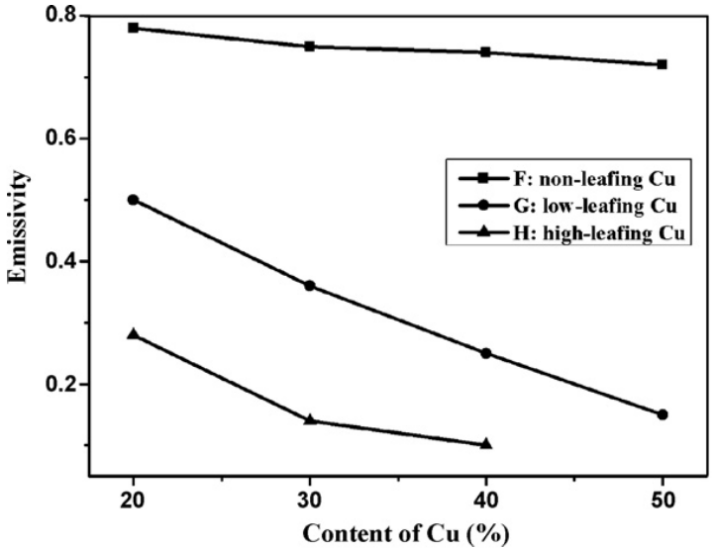

Figure 4.5 Change in LWIR emissivity with respect to Cu content (% wt.) and leafing features.

The figure shows that, leafing degree influenced emissivity value of the coating considerably. As a result, 4 μm flaky particles with high leafing features showed the lowest emissivity of 0.1 at a loading 40 wt.% . Yu stated that the floating degree and the leafing features of particles in the polymer were the main causes of the high reflectance in LWIR.

The effect of chemical composition, roughness, thickness, and temperature on the infrared emissivity of PU/Cu coating in 8-14 μm waveband were investigated by Yu et al.[87]. The composite was prepared by conventional mixing method in different contentration ratios and painted on a tin substrate by Doctor Blading and spraying techniques. IR emissivity characterization was performed via IR-2 Infrared Emissometer device from room temperature to 420 K. Moreover, the relation between conductivity and emissivity parameters was investigated for the material. When Polyurethane(PU)/50% Cu coating was applied, as the coating thickness increased, the emissivity remains at 0.1 as the minimum and this value does not change after 40 μm. The electrical conductivity increased, and the emissivity decreased with increasing temperature in the temperature range of 290-380 °K. For

temperatures higher than 380 °K, the electrical conductivity decreased, and the emissivity increased due to the formation of CuO.

Chou et al.[88] studied low LWIR emissivity of composite paints with micro and nano-sized Ag particles. Traditional mixing method was performed to obtain composite materials with different contents between 10 and 40 % wt. The paint was coated onto alumina substrates by the Doctor Blade method at a thickness of 140 μm. As a second technique, Ag nano-sized colloids with 25% wt. content were coated onto substrate by spin coating after inorganic binder was coated onto substrate. The cross-sectional SEM images of coated samples are provided in Figure 4.6.

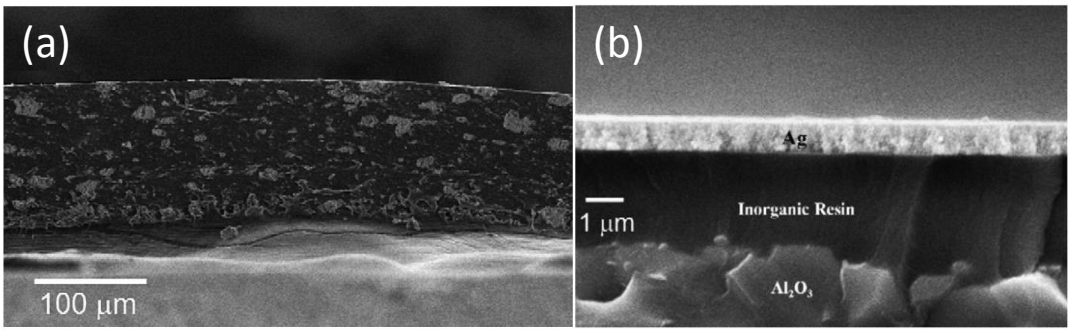

Figure 4.6 Cross-sectional SEM images of coatings performed by (a) Doctor Blade method with micro-sized Ag and acrylic resin, (b) spin coating method seperately with nano-Ag colloids and inorganic binder [87].

As seen in the figures, with the second method, metallic layer was placed at the top of the substrate surface. FTIR and a thermal camera were employed to measure the average and spectral emissivity of the materials. Because Ag nanomaterials have remarkably low emissivity compared to micro-sized materials the alternative coating was prepared. The second method was performed to prevent the Ag nanoparticles from sinking to the bottom of the coating layer. As a result, the composite with nano-Ag had the lowest emissivity of 0.04 with 250 nm thickness. Moreover, it was stated that heat treatment following coating has an influence on emissivity results since the smoothest surface was formed at a baking temperature of 150 °C.

Zhang et al.[89] prepared Ag/polyurethane (PU) composite coating with different Ag content in order to obtain low infrared emissivity in LWIR wavelengths. The reason for the use of micro-Ag in the composite coating is that Ag has high chemical stability and electrical conductivity compared to Al and Cu particles. Additionally, PU was selected as a matrix material because of its high stability against corrosion and ideal mechanical properties. PU/Ag composite material was prepared by conventional mixing method by sonication with different Ag/PU weight ratios of 1/9, 2/8, 3/7, and 4/6, then sprayed onto a steel substrate with a thickness of 40 μm. LWIR emissivity was measured by IR-2 Infrared emissometer and SEM was used to investigate the microstructure and morphology of the composites. The cross-section of microstructure model and cross-section SEM image of coating were provided in Figure 4.7 (a) and (b), respectively.

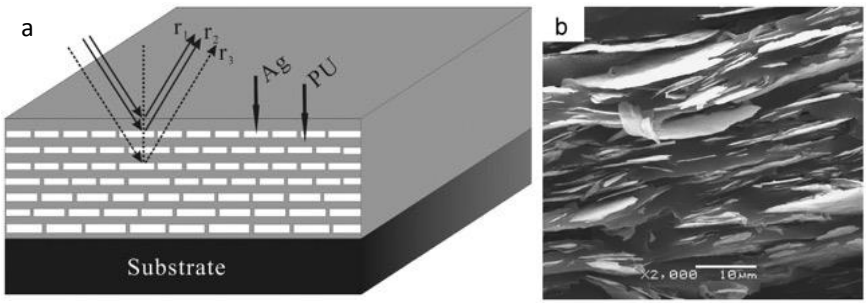

Figure 4.7 Cross-section image of (a) structural model and (b) SEM image of coating [89].

According to SEM images, it was observed that as prepared material has shown photonic crystal structure features. The simulation was performed to obtain the optimum content of Ag. The calculated emissivity of 0.088 nearly matched the prepared product's emissivity of 0.082 ratios had a minimum emissivity at a Ag loading of 20%.

Hu et al.[90] fabricated thermally resistive, aluminum pigment added epoxy-siloxane composite material with low long-wave infrared emissivity. They investigated the influence of content ratio, morphology, thickness and roughness on infrared emissivity. Micron-sized Al particles were mixed with epoxy-siloxane in different

concentrations by the conventional method after the pre-treatment of Al. The composite material was coated on a tin substrate by spraying. LWIR emissivity was measured by IR-2 infrared emissometer and FTIR. Considering the emissivity values according to different aluminum percentages, it was observed that emissivity reached its lowest value when Al was 40 wt. %. A more homogeneous structure was obtained when the aluminum ratio increased from 10 to 40% by weight. When the 50% level was reached, the aluminum particles were agglomerated and formed an inhomogeneous structure. It was observed that the emissivity increased with the increase in roughness. The lowest emissivity was obtained as 0.15 when the coating thickness reached 45 μm and did not change further with the thickness.

Although the use of metal pigments is the most common way to reach infrared low emissivity, pure metals increase the brightness of the material in the visible region and have a negative effect on radar stealth performance[91]. In addition, metallic pigments are not sustainable due to their poor corrosion resistance. For the ones with corrosion resistance, the application is not cost-effective[92]. An increase in the temperature will also result in the high absorbance of metallic materials[23].

4.2 Metal Oxide Pigments

The drawbacks of metallic particles such as oxidation at high temperatures and corrosion directed researchers to study oxide ceramic particles. Because of their high melting points, resistance to oxidation, and high visible light absorbance, metal oxide ceramic materials have attracted attention of numerous researchers[93,94].

Chen et al.[95] fabricated TiO_2/polyurethane nanocomposites for low emissivity between 8 and 14 μm. The size of TiO_2 nanoparticles were 30-35 nm. The composite material was fabricated through conventional dispersion of 0.3% by weight TiO_2 in the PU matrix. The surface composition and distribution of TiO_2 within PU matrix were investigated using XRD, TEM and SEM methods. LWIR infrared emissivity was monitored using FTIR spectra. It was stated that PU and TiO_2 components

possess higher infrared emissivity than the composite material. While the emissivity values of PU and TiO_2 were 0.945 and 0.925, the LWIR emissivity of the nanocomposite was measured as 0.538.

Yun et al.[96] fabricated low IR emissive and high visible absorbing nanocomposite systems using SiO_2-ZnO. The material was obtained in three consecutive steps, namely spin-coating, electrodeposition, and calcination processes. The material's radiation performance was investigated by varying the number of spin coating cycles, SiO_2 particle size (for the visible absorbance) and ZnO content (providing low emissivity as claimed). The UV-Vis spectrophotometer was used for visible absorbance measurements, and the infrared emissivity in the MWIR was measured by IR-2 Infrared Emissometer. According to the results, the addition of the ZnO into the structure had a positive effect on lowering the IR emissivity to 0.4, while SiO_2 protects the coating color.

Tengchao et al. [97] investigated the effect of morphology on the high-temperature MWIR emissivity for ZnO nanoparticles. They prepared needle, pencil, flat, and flower-shaped nanoparticles with an average size of 55 nm using hydrothermal, co-precipitation, and sol-gel methods. The characterizations of the nanopowders are performed by XRD and FESEM, infrared emissivity characteristics are investigated by IR-2 Emissometer between 100 and 800 °C. The SEM images of particles in different morphologies are provided in Figure 4.8 below.

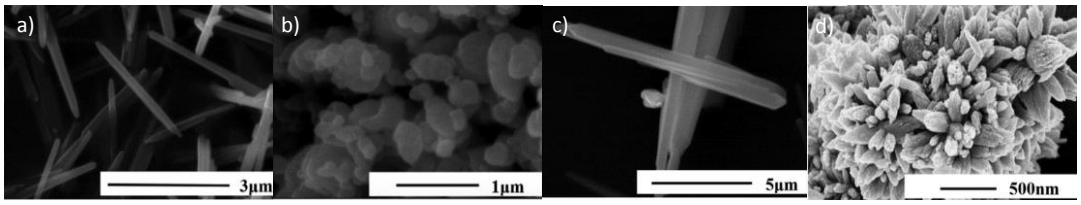

Figure 4.8 SEM images of ZnO nanoparticles in a) needle-shaped, b) flat-shaped, c) pencil-shaped, d) flower-shaped morphology [97].

Among the prepared particles, flat-shaped ZnO showed the lowest emissivity as 0.41 at 500 °C. The reason for the low emissivity of flat-shaped particles was explained as an increasing overlap region between particles that caused to more electric dipole

contact between particles which resulted in high dielectric constant. The flat-shaped particles had higher overlap area between particles, as stated.

Tengchao et al.[98] investigated high-temperature MWIR emissivity of Ce-doped ZnO oxide powder. Sol-gel method was used for the synthesis and a dopant fraction between 0.5 and 7% atom. was examined. The particle size of the samples were from 400 to 200 nm, as the Ce content was increased in the structure, particle size was reduced. The characterization of the material was performed by XRD, SEM and TEM. Electromagnetic features were analyzed by FTIR spectroscopy, UV-Vis spectroscopy, and IR-2 Emissometer between room temperature and 800 °C. The lowest emissivity was measured for 3%-doped particles at 500 °C as 0.329. This low emissivity was attributed to an increase in of the powder conductivity due to the increase in number of free carriers in the structure. After 500 °C, the lattice vibration become the major effect on IR radiation features of the material which increased infrared absorbance and caused to increase of emissivity in MWIR.

Shanshan et al.[99] investigated MWIR emissivity of Co-doped TiO_2 particles. The particles were synthesized by a solid-state reaction the effect of calcination temperatures between 900 and 1200 °C was investigated. The infrared emissivity was measured between room temperature and 800 °C. The materials were characterized by XRD to confirm doping and SEM to investigate the particle morphology. The infrared emissivity was measured by IR-2 Emissometer, and the visible absorbance feature was analyzed by UV-Vis spectroscopy. According to the results, the absorbance in the visible region was increased with the Co-doping at an annealing temperature of 1200 °C. Maximum infrared emissivity of 0.332 was reported at an annealing temperature of 1100 °C. It was stated that the vibration in the lattice, promoted by the increase in lattice defects due to the change in calcination temperature, is the main effect on infrared emissivity at high temperatures.

Haiti et al.[100] investigated the thermal radiation characteristics of vanadium (IV) oxide (VO_2). The phase transformation of VO_2 occuring at 68 °C was the main reason for the study. Upon phase transformation, the infrared emissivity of the

material changes. Nanopowders of VO_2 was synthesized through the hydrothermal method and nanopowders were compacted into pellets for measurements. The average particle size was reported as 68 nm. XRD, TEM, and SEM were utilized for the structural characterization of the synthesized material. The XRD pattern of the material was obtained between 20 and 100 °C to verify the phase transition. The infrared emissivity of the material was calculated using the data obtained from FTIR alaysis. The thermal imaging was performed from 40 to 100 °C to observe the effect of phase transition on the thermal emissivity. The thermal images at 40 and 75 °C and the change in radiation temperature with background temperature are provided in Figure 4.9 (a), (b) and (c), respectively.

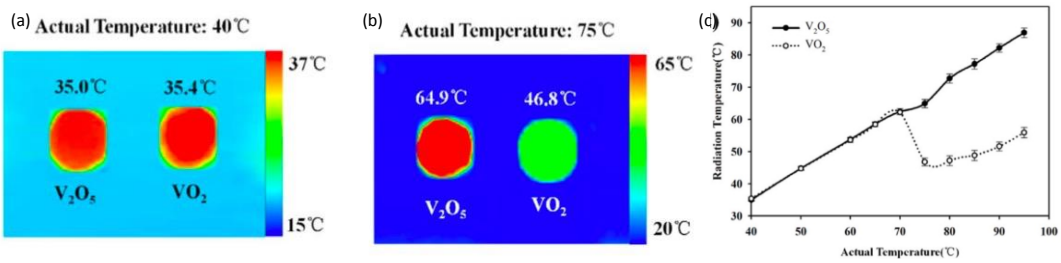

Figure 4.9 (a) Thermal image at 40 °C background temperature, (b) thermal image at 75 °C background temperature, (c) change in radiation temperature with actual temperature [100].

In thermal imaging, V_2O_5 was used as a reference sample. Phase transition was observed at 68 °C and this transition affected the emissitivy of the sample. When the critical temperature was exceeded, the change in the emissivity was measured as 0.34 and 0.46 in MWIR and LWIR ranges, respectively.

Although the metal oxide pigments will provide improvements in chemical and thermal resistance to the component that will be used as low-emissivity coating especially at high temperatures and MWIR band, in general, they have poor IR emissivity performance.

4.3 Photonic Crystals and Multilayered Thin Films

Photonic crystals are multilayered structures consisting of at least two different materials. The material offers a wide-range of optical features by adjusting the periodicity and thickness of the layers[101]. In this way, low IR emissive, nearly perfect reflector can be selectively obtained in both MWIR and LWIR bands. In addition, the high rate of radiation can be shifted to atmospheric absorbance ranges by the photonic crystals[16].

Zhang et al.[102] studied on LWIR and MWIR multiband low emissivity coating by developing Ge/TiO_2//Si/SiO_2 one-dimensional photonic crystal. The main purpose of the study was to reduce the infrared radiation in 3-5 and 8-14 μm wavebands and increase the emissivity in 5-8 μm by structural and composition arrangements in the material. In this way, the heat can be released in the infrared range that cannot be detected by the seekers. Theoretical calculations were performed to determine the thicknesses of each layer by considering the optical thickness. Additionally, the periodicity of the photonic crsytal was determined as 5. The material was deposited using high vacuum electron beam deposition onto the quartz substrate. The cross-sectional SEM image of photonic crystal and modeled structure are provided in Figure 4.10 (a) and (b), respectivley.

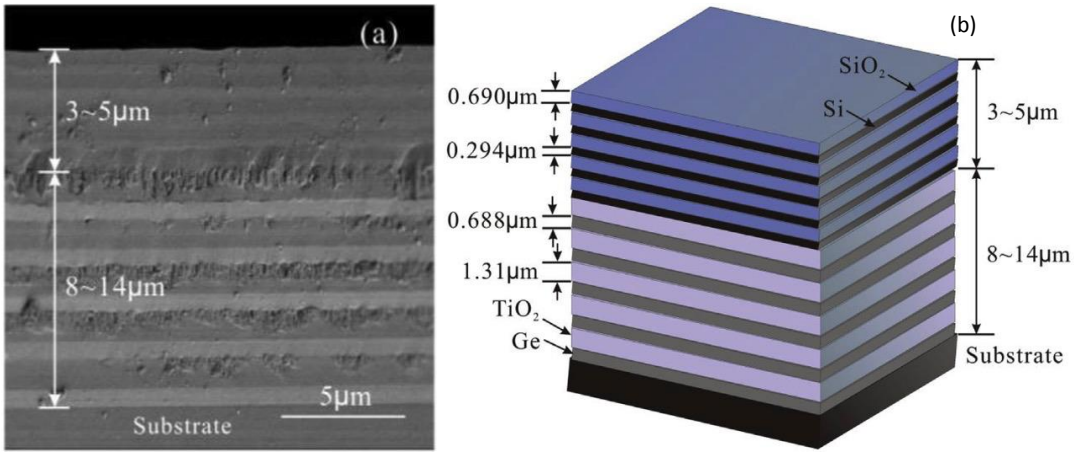

Figure 4.10 Cross-sectional (a) SEM image, (b) model [102].

The SEM image show that the periodically stacked multilayered structure was obtained. FTIR spectroscopy was used to determine the emissivity of the photonic crystal. Calculated and measured emissivity values are provided in Figure 4.11 (a) and (b), respectively.

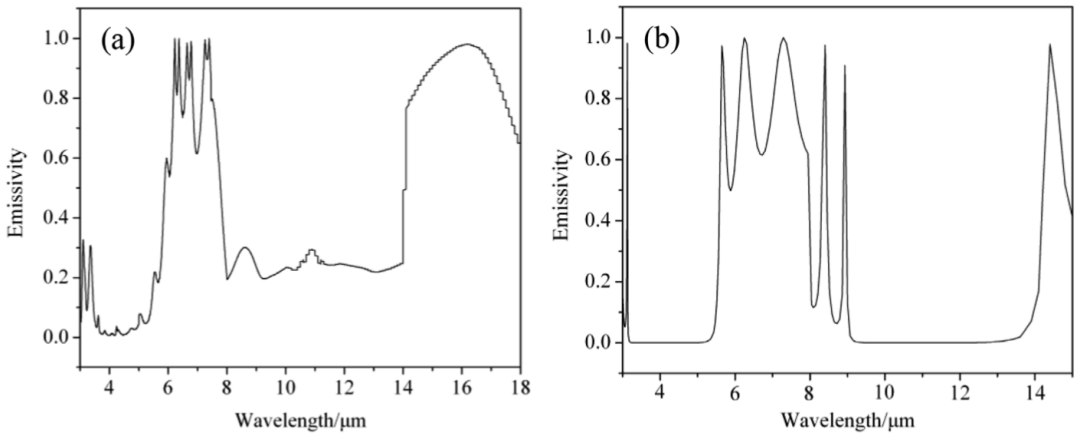

Figure 4.11 Spectral emissivity of photonic crsytal (a) measured and (b) calculated [102].

As seen in the Figure 4.11, the calculated and measured emissivities were nearly matched with each other in LWIR band. As a result, the lowest emissivity values in MWIR and LWIR were obtained as 0.060 and 0.239, respectively. The 5-8 μm band emissivity reached 0.562.

Qi et al.[103] have investigated MWIR emissivity and visible absorbance performance of one-dimensional ZnS/Ge photonic crystals with a periodicity of 4. The effect of ZnS top layer thickness was changed to obtain different colors in the visible range and low radiation in MWIR wavebands. The IR radiation and visible reflection spectra was calculated and compared to the experimental results. The samples were prepared by magnetron sputtering on quartz substrates. A spectrophotometer was used to measure visible reflection spectra. FTIR was used to obtain IR radiation characteristics and an infrared emissometer was used to measure the average emissivity. 4 photonic crystals with different colors in the visible spectrum were prepared and the an average minimum emissivity value of 0.054 was obtained, which was in agreement with the theoretical calculations.

Pan et al.[104] studied on stealth technology in MWIR, LWIR, and visible bands with photonic crystals. The main purpose of the study was to shift the IR radiation in MWIR and LWIR bands to the atmospheric absorbance range. The structure was formed using combination of Au, $Ge_2Sb_2Te_5$, and Si with thicknesses of 200, 220, and 30 nm, respectively. Design and numerical analysis of the material were performed via Lumerical software by the FDTD method. The films were deposited using ultra-high vacuum magnetron sputtering method onto glass substrates. Spectral absorbance of the films was measured at room temperature using a FTIR spectrometer. The emissivity was measured by a thermal camera between temperature of -20 and 250 °C (Figure 4.12).

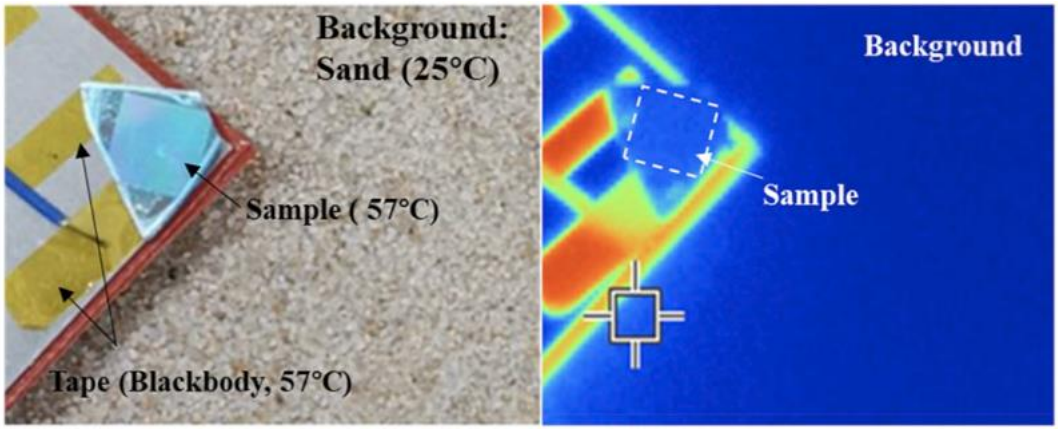

Figure 4.12 Visible and thermal imaging of the photonic crystal [104].

As seen in the Figure 4.12, the sample's thermal image was similar with background. The emissivity values of 0.56 and 0.27 were obtained in the MWIR and LWIR ranges, respectively. The highest emissivity was obtained as 0.77 in the atmospheric absorption band.

Photonic crystals and multilayer thin-film coatings have been studied due to their high performance in visible range high absorption and infrared low radiation properties, providing optimization possibilities in the respective bands.[17]. However, due to complex preparation procedures, high cost, and requirement for specialized process equipment of photonic crystals, it is difficult to manufacture on a large scale and apply them over large areas [105].

4.4 Core/shell and Composite Pigments

A composite material is a combination of two or more materials, and the resulting assembly has qualities that are better than those of the individual components [106]. At the micro-scale, filler particles are preferred to be added to the base (matrix) material to improve microstructural, thermal, electrical and optical properties[107]. Core/shell particles are a class of particles that comprise both a core and a shell, as their name suggests. Depending on its construction, the core and shell can be made of different materials or of the same materials. Core/shell particles are prepared to combine desired properties for a synergistic effect, to form stable particles, or to strengthen weak properties of various materials and structures[108].

Yunfeng et al.[109] argued that the use of metallic pigments for infrared low-visible coatings increases the brightness in the visible region and negatively affects the radar absorbing performance. In their work, Al/Co_3O_4 magnetic composite pigments were produced by thermal cracking and hot-flowing methods. Co_3O_4 was used due to its high stability and magnetic properties. Al flakes (size of 23 μm) was coated with Co_3O_4. The Co_3O_4 thickness was controlled by the process temperature and the amount of Co_3O_4 added to the process. SEM characterization was conducted with pure Al and composite pigments which are synthezied at different reaction temperature and had different Co_3O_4 content (Figure 4.13).

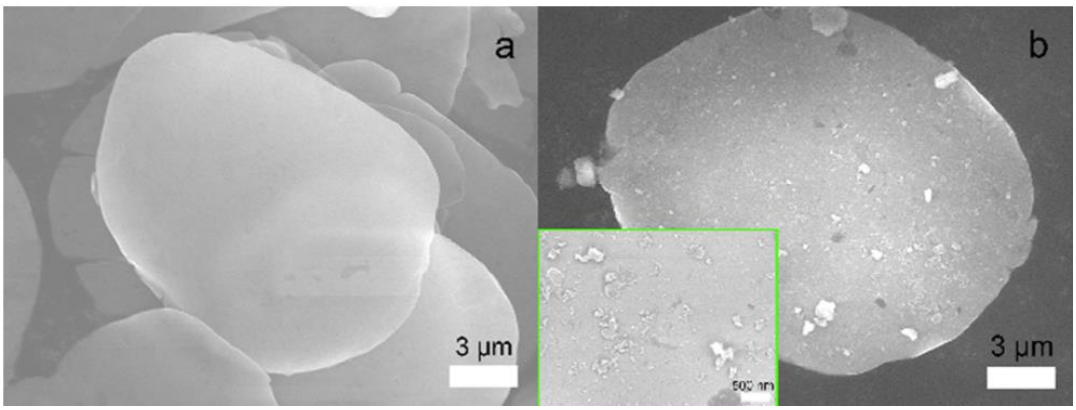

Figure 4.13 SEM images of (a) pure Al, (b) Al/Co_3O_4 particles [109].

CO_3O_4 particles were formed on Al particles, as seen in the Figure 4.13. The composite coating was prepared with 20% wt. core/shell particle and 80% wt. lacquer and thinner mixture. FTIR spectrometer was used to determine the emissivity of the composite coating. UV/VIS/NIR spectrophotometer was used to determine the reflectance. VSM (Vibrating Sample Magnetometer) was used to evaluate the magnetic properties of coatings. The effect of Co_3O_4 content and synthesis temperature were investigated on the IR emissivity and a minimum of 0.45 was measured. The visible region reflectance was observed as a minimum of 69.2%. Visible reflectance of Al particles were reduced by Co_3O_4. The VSM results showed that the material was not reached the saturation magnetization. It was stated that, although saturation magnetization was not reached with core/shell powders, magnetic Al/CO_3O_4 could improve the radar-absorbing performance of the structure.

Yuan et al.[110] synthesized and analyzed Al/Fe_3O_4 core/shell pigment in the study that aims for LWIR low emissivity, low visible reflectance, high radar absorbing capability. The reason for using Fe_3O_4 as a shell was that the material has absorbing features in visible and microwave ranges. The reflectance was measured with the FTIR spectrometer, and the emissivity was calculated according to the Planck function, the visible (UV/VIS/NIR) reflectance spectra are measured with UV/VIS/NIR spectrophotometer and the magnetic properties were measured with the VSM (Vibrating Sample Magnetometer). As stated, the synthesis parameters of temperature and solvent type affected the shell structure and morphology. The shell morphology determined the electromagnetic radiation and optical characteristics of material. The FTIR reflectance results and the photograf of flake Al and core/shell pigments provided in Figure 4.14 (a) and (b).

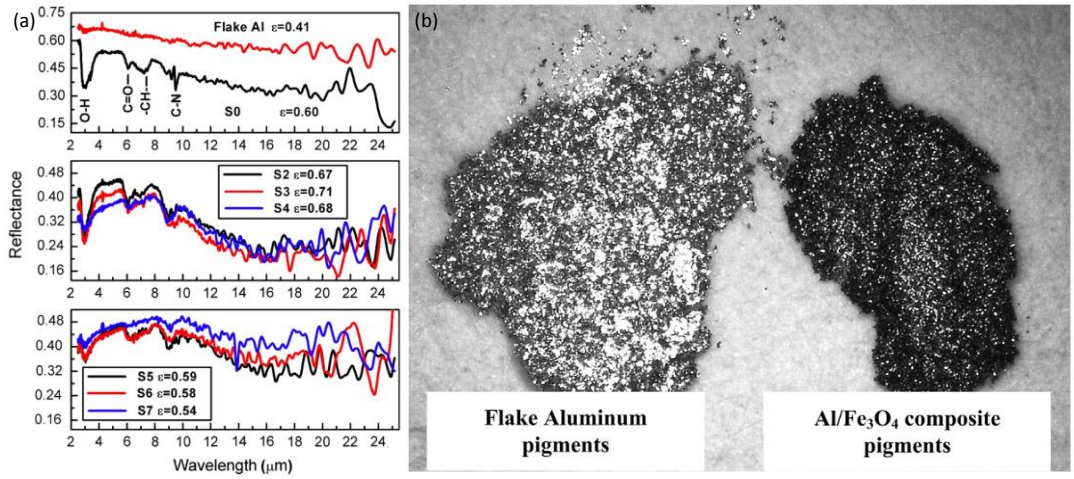

Figure 4.14 (a) FTIR reflectance results and (b) the photograf of flake Al and core/shell pigments [110].

As seen in the Figure 4.14, IR reflectance was reduced with core/shell pigments. The minimum emissivity value was calculated as 0.56, which was 0.13 higher than that of pure Al pigment. Average visible reflectance (380-790 nm) value reduced by 63.46% compared to pure Al powder . The smooth and homogenous shell structure was formed at the highest reaction temperature and darkened the pigment while IR emissivity increased slightly. VSM measurement showed that the core-shell powder which had the lowest emissivity showed the highest saturation magnetization of 25.9 emu/g. Radar absorbance features was also improved with core/shell material.

Luping et al. [26], fabricated Al-SiO_2 nanocomposite films using magnetron co-sputtering technique. Nanocomposite thin films with an average thickness of 160 nm was prepared and IR and visible reflectance of the composite films were analyzed. by varying the SiO_2 content ratio in the material as 4.6%, 6.9%, and 14.6% by volume. The electromagnetic simulation was performed via Lumerical software Simulation and characterization results showed that the increase in the volume content of SiO_2 causes the rise of infrared emissivity. Thermal imaging of nanocomposite films are shown in Figure 4.15.

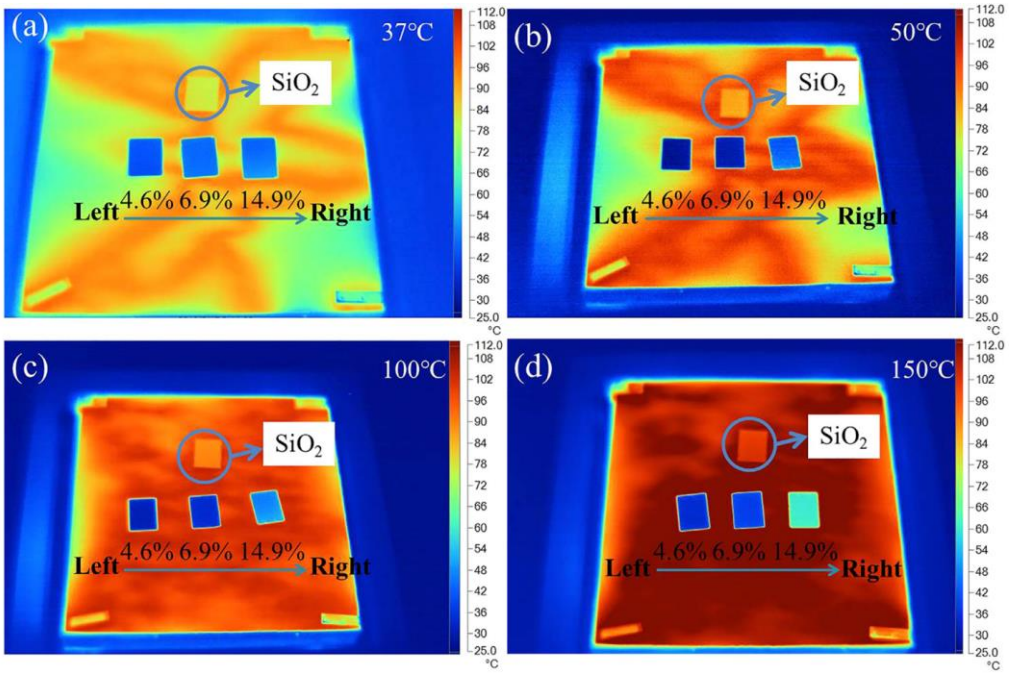

Figure 4.15 Thermal imaging of Al-SiO_2 nanocomposite films at different background temperatures [26].

As seen, the increase in SiO_2 volume ratio resulted in high radiation of composite film. The visible and IR reflectance of samples are provided in Figure 4.16.

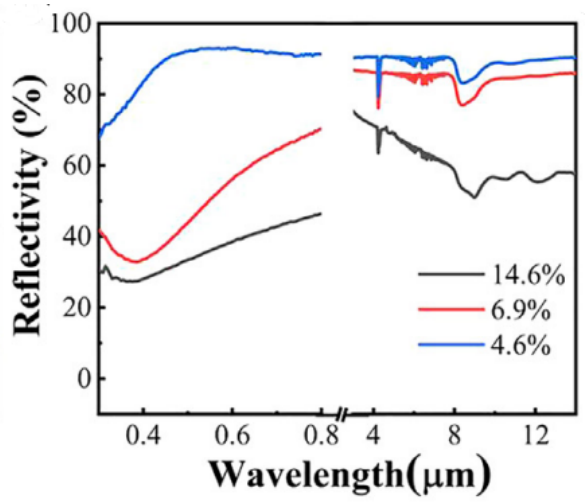

Figure 4.16 Reflectivity of nanocomposites in visible and IR bands [26].

A visible reflectivity and IR emissivity of 0.33 and 0.12 was measured for the material with 6.9% SiO_2, respectively. The IR reflectance was similar to the 4.6% SiO_2-filled nanocomposite yet visible reflectivity was lower by 61%.

Yong et al. [111], prepared polyurethane-coated TiO_2/MnO_2 nanorod core/shell structures to investigate low-observable characteristics in the LWIR range. The material was prepared by deposition of TiO_2 on MnO_2 nanorods, and the PU grafting, sequentially. Nanocomposite with calcinated TiO_2 showed the best IR emissivity of 0.652, which was less than the emissivity values of individual components.

Xiaoyun et al. [112] investigated the composite material formed of polyurethane, nano-Ag and ZnO nanorods in terms of infrared emissivity. ZnO nanorods were synthesized on stainless steel substrates, Ag was deposited afterwards onto ZnO nanorods by immersing the ZnO into $AgNO_3$ solution, followed by PU addition by spin coating to the nanocomposite. SEM images of ZnO nanorods and ZnO/Ag were provided in Figure 4.17 (a) and (b), respectively.

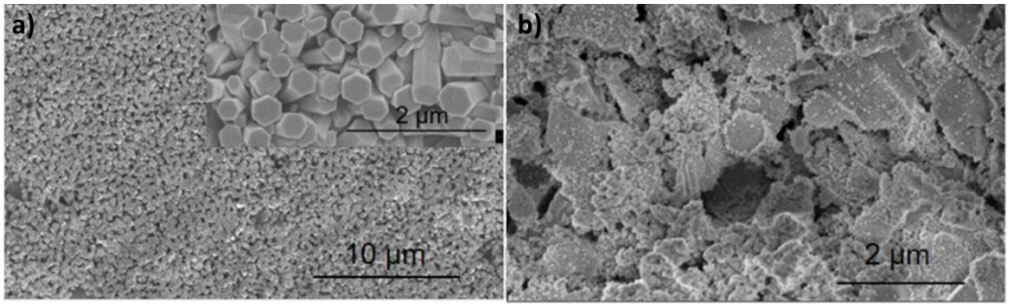

Figure 4.17 SEM images of (a) ZnO and (b) ZnO/Ag at different magnifications [112].

As seen in the Figure 4.15, Ag was deposited on the ZnO nanorods successfully. The performance of the material was analyzed depending on the content ratio of both Ag and ZnO. Infrared emissivity was reduced by increasing the density of ZnO nanorods on the substrate which caused to increase in the Ag amount deposited on the nanorods. A minimum emissivity value of 0.68 was obtained from the fabricated composite material.

Lan et al. [113] studied multiband (RF-IR) stealth material with ZnO/SnO_2 core/shell structure. The SnO_2-coated ZnO nanomaterial was prepared by the hydrothermal method. SEM image of ZnO/SnO_2 and emissivity comparison of ZnO, SnO_2 and ZnO/SnO_2 are shown in Figure 4.18 (a) and (b).

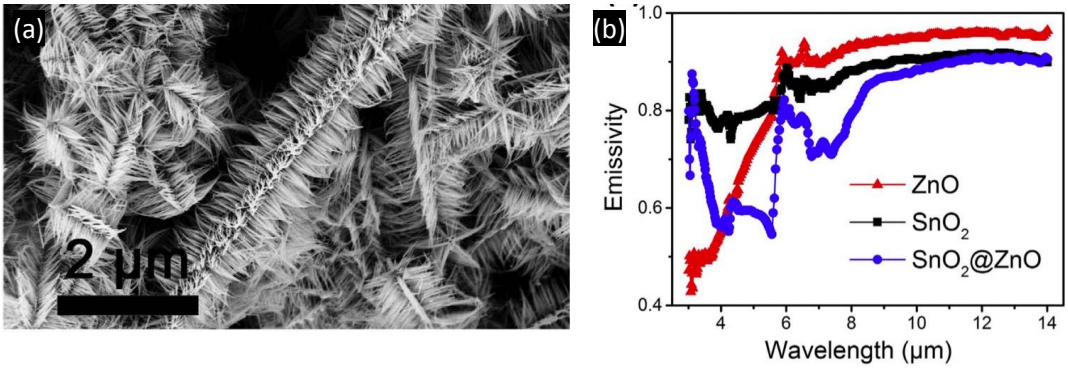

Figure 4.18 (a) SEM image of ZnO/SnO_2, (b) Spectral IR emissivity of ZnO, SnO_2 and ZnO/SnO_2 [113].

As seen in SEM image, SnO_2 nanowires covered the ZnO nanorods. 8.0–12.4 GHz reflection/transmission was measured with vector network analyzer and Infrared emissivity was measured at 50 °C using a spectrum radiometer and compared to that obtained from pure ZnO and SnO_2, the powder was molded for the measurements. The core/shell material has the lowest emissivity in both MWIR and LWIR ranges with average values of 0.65 and 0.89, respectively. The minimum reflection loss of core/shell was measured as −23.51 dB which was lower than that of ZnO and SnO_2. It was indicated that the radar-stealth performance was improved with core/shell when comparing ZnO and SnO_2.

Metallic particles are the most reflective materials in visible and radar bands. Covering the metallic particle with a metal oxide shell prevents the direct interaction of metallic particles with electromagnetic waves in radar and visible bands. If metallic particles were mixed with metal oxide particles, electromagnetic waves could be reflected from metallic surfaces. Therefore, compared to metallic particles, core/shell structures can offer higher absorbance in the radar and visible bands and comparable reflectance in the LWIR band.

The literature review shows that the emissivity of composite coatings are influenced significantly by particle size, shape and filler fraction. The particles determined the emissivity features of coatings due to their optical and IR radiation characteristics. The literature also indicates that the core/shell and composite pigments are highly useful for low infrared emissivity with the advantages of low visible reflectance and radar absorbing characteristics. The core/shell and composite pigments are reported to provide lower thermal radiation compared to the oxide materials and higher absorbance in the visible and radar regions compared to the metallic materials. In core/shell particles, shell morphology, thickness and content determine the IR radiation features of the materials [26].

CHAPTER 5

MATERIAL DETERMINATION

Material determination was made by researching the literature on low-emissivity materials in the LWIR range. In the literature, aluminum (Al) and silver (Ag) were widely used metallic particles for IR radiation reduction studies due to their similar high reflectance features in IR bands. Al was chosen as the core material of the particle due to its cost, abundance, and outstanding reflective characteristics. Fe_3O_4, SiO_2, TiO_2, and ZnO were determined as candidate shell materials since they have relatively LWIR low emissivity and high absorbance compared to metallic particles in visible and radio frequencies. The reflectance characteristics of the pure Al and the core/shell particles with Al core and candidate shell materials were analyzed in the LWIR band.

5.1 Material Design

The core/shell material determination was carried out by core/shell particle modeling in a virtual environment and analyzing EM wave reflectance features of these particles in the LWIR range. The modeling and analysis were performed by FDTD method via Ansys Lumerical software. The software fundamentally utilizes Maxwell's Equations to solve the electromagnetic behaviors of the materials which are exposed to EM radiation.

5.2 Finite-Difference Time-Domain Method

Finite-Difference Time-Domain (FDTD) is a computational method that provides the approximate solution of Maxwell equations by separating time and space varieties of electric and magnetic field intensities in finite differences. The method

was first introduced in 1966 by Kane Yee as an algorithm known as Yee algorithms[114].

As a fundamental principle, the algorithm is employed based on grinding the specified area into unit cells, which is called Yee cell. Numerical solving of the magnetic and electric field components of Maxwell equations are performed separately in time and space derivatives of the propagating electromagnetic wave. For each adjacent cell, the variables are updated based on the results for the prior cell, the process is repeated to obtain the result for the determined region[115]. A schematic illustration of the Yee cell is shown in Figure 5.1.

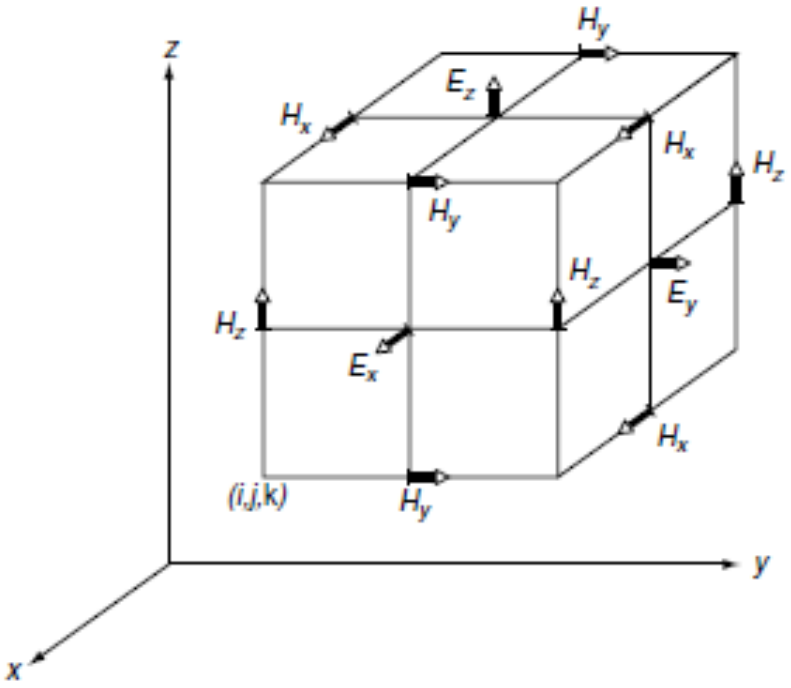

Figure 5.1. Schematic illustration of Yee Cell[116].

FDTD method was used to investigate the propagation of transmitted light, wave scattering, discontinuity in the media, and the radiation features of an object. The main advantage of the FDTD in solving electromagnetic wave behaviors, is the capability to analyze the structures in complex shapes and the material in different types by means of radiation characteristics. By utilizing the FDTD method, the

interaction of the electromagnetic wave with different types of materials (conductive, dielectric, magnetic, etc.) or the interaction of complex structures with electromagnetic waves can be calculated[117]. The models of the structures can be created in the analysis region, thanks to simulation software available on the market. Despite the advantages of the FDTD in solving the electromagnetic wave behaviors in the object, the major challenge for FDTD simulation is defining the material's structural characteristics such as discontinuities, defects, roughness, etc. features[118].

5.3 FDTD Analysis

Determination of core/shell particles in terms of shell type and thickness was performed by the FDTD method via *ANSYS Lumerical* software, which provides a numerical solution of the FDTD method using Fresnel equations. The refractive index data of Al[119], Fe_3O_4[120], SiO_2[121], TiO_2[121], and ZnO[120] are used as the simulation input.

The candidate shell material covering Al core particles were analyzed in the LWIR band on the software and spectral reflectance in 8-14 μm was obtained. The average emissivity values of the particles depending on shell type and thickness were calculated. For each sample, the core was adjusted as a spherical shape with a constant size of 10 μm in diameter. The plane wave source was used at a steep angle to -Z-direction on the simulation since it is representing the real conditions. The boundary conditions were adjusted as periodic in the X and Y-direction, and PML (Perfectly Matched Layer) in the Z-direction. When a plane wave was used in the simulation, periodic boundary conditions were suggested by the product owner in the X and Y directions. Otherwise, it was stated that the wave would be absorbed in the relevant directions in other conditions. The PML boundary absorbed all energy sent to it and prevented them to reflect into the simulation region. In this way, the noise that could be occurred due to mirrored waves at the boundary was avoided.

The maximum mesh step size or cell size was set to half of the shell thickness to place at least one solution point in the shell region and to calculate the shell response. FDTD simulation region was adjusted as 100 μm in the Z-direction, and to the particle diameter in the X and Y-directions. The mid-point of the region was placed at the (X, Y, Z) coordinates of (0,0,0). The top monitor was located at (0,0,45), and the source was placed at (0,0,40) in the XYZ system. In order to verify the simulation setup, an Al plate with a thickness of 20 μm was placed at -30 μm in the Z direction, and the reflectance analysis was performed in the LWIR range. The simulation resulted with a 0.99 reflectance as average in the LWIR range for the Al plate. After verification, the plate was removed, and the particle was placed to the plate's location in the Z-direction and centered in the X and Y-directions. FDTD simulation setup for Al core and Al/metal oxide shell particles are shown in Figures 5.2. and 5.3. below, respectively.

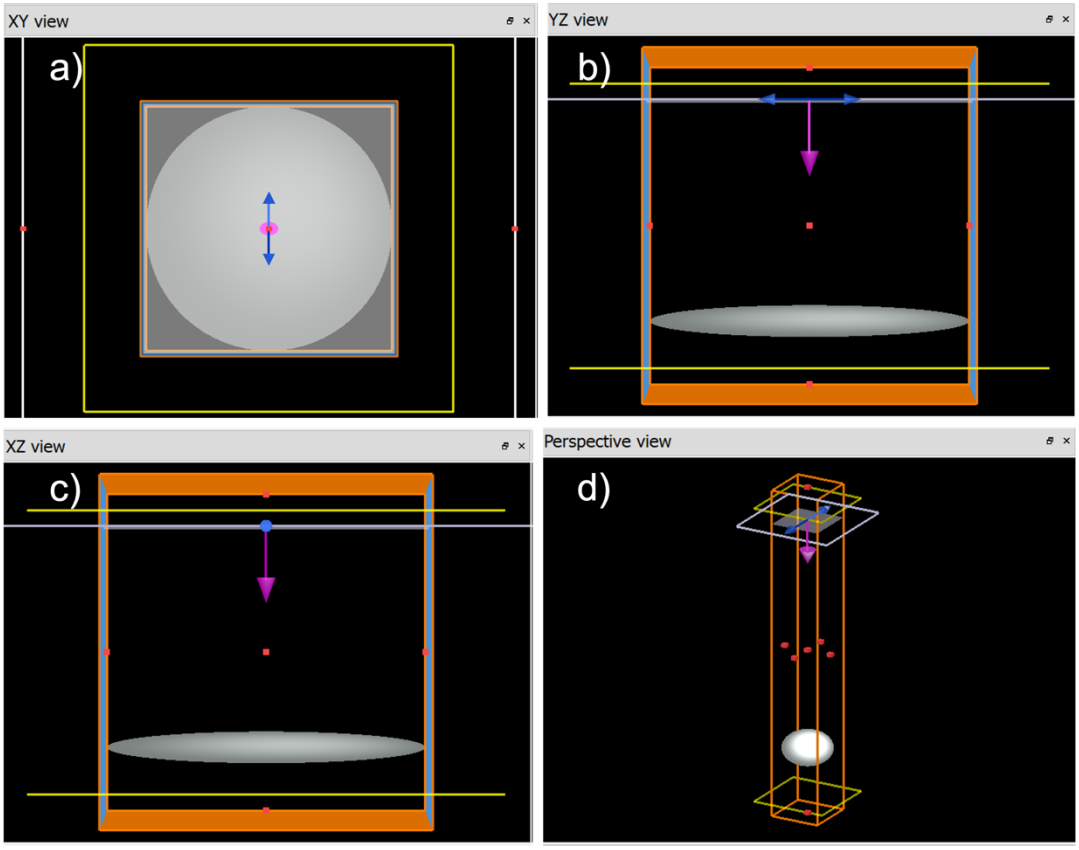

Figure 5.2. Simulation setup for Al core particle from a) XY view, b) YZ view, c) XZ view, d) perspective view.

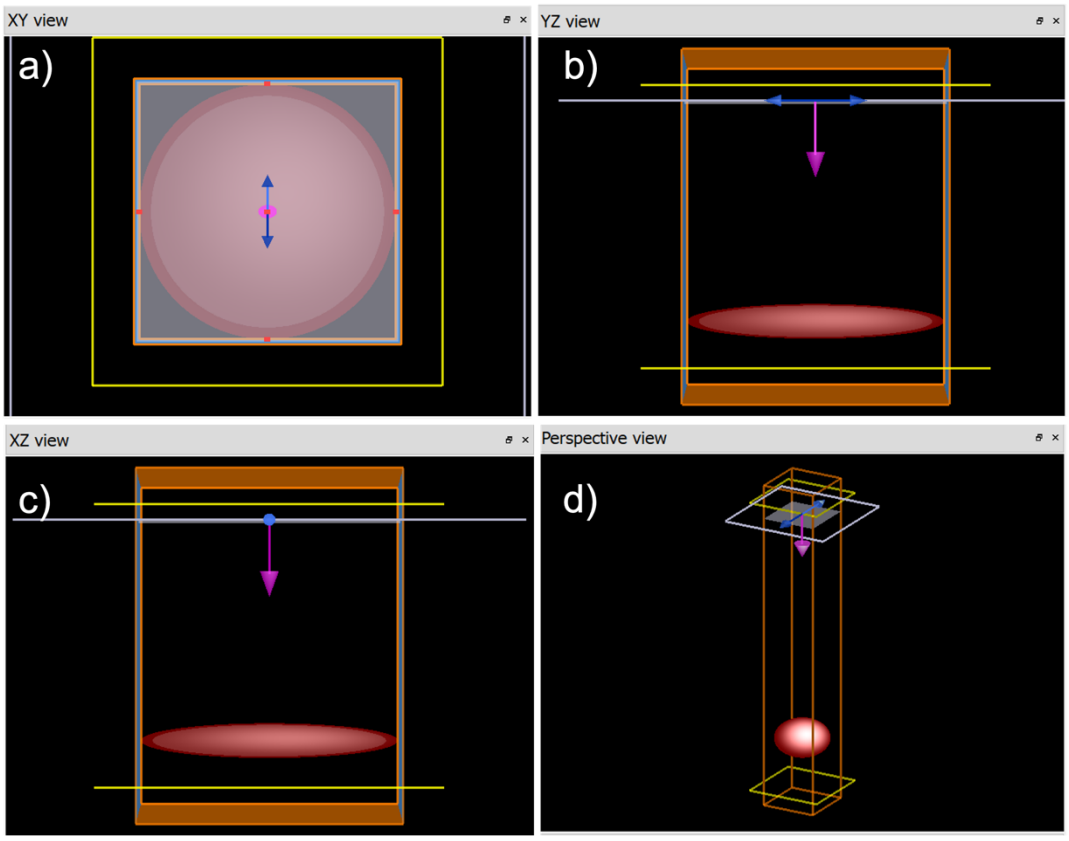

Figure 5.3 Simulation setup for Al/metal oxide core/shell particle from a) XY view, b) YZ view, c) XZ view, d) perspective view.

The varied input parameters for the simulation on the software are defined in Table 5.1 below.

Table 5.1 FDTD input parameters.

Shell Thickness (μm)	Mesh Step Size (μm)	FDTD region (X, Y) size (μm)
0.5	0.2	11
0.4	0.15	10.8
0.3	0.12	10.6
0.2	0.08	10.4
0.1	0.05	10.2

The analysis was operated in the range of 8-14 μm plane wave source wavelength range and the results were obtained from the top monitor which collected the specular reflectance data of the particles.

5.4 FDTD Simulation Results

The spectral and average reflectance results of pure Al and core/shell with Al core particles were obtained by the FDTD method via *Ansys Lumerical* software. Pure Al spherical particle reflectance depending on the wavelength is given in Figure 5.4.

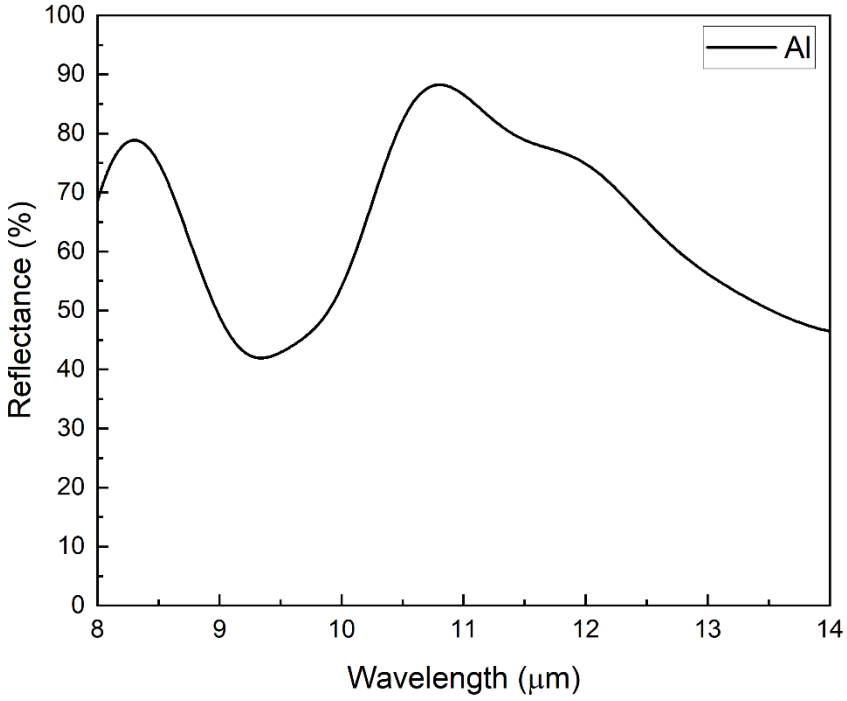

Figure 5.4 FDTD Simulation result on the spectral reflectance for spherical Al particle.

The spectral reflectance of particles with respect to shell thicknesses of 100, 200, 300 and 400 nm are provided in Figure 5.5 (a) – (d), respectively. The core/shell particles were Al/Fe_3O_4, Al/TiO_2, Al/SiO_2, and Al/ZnO.

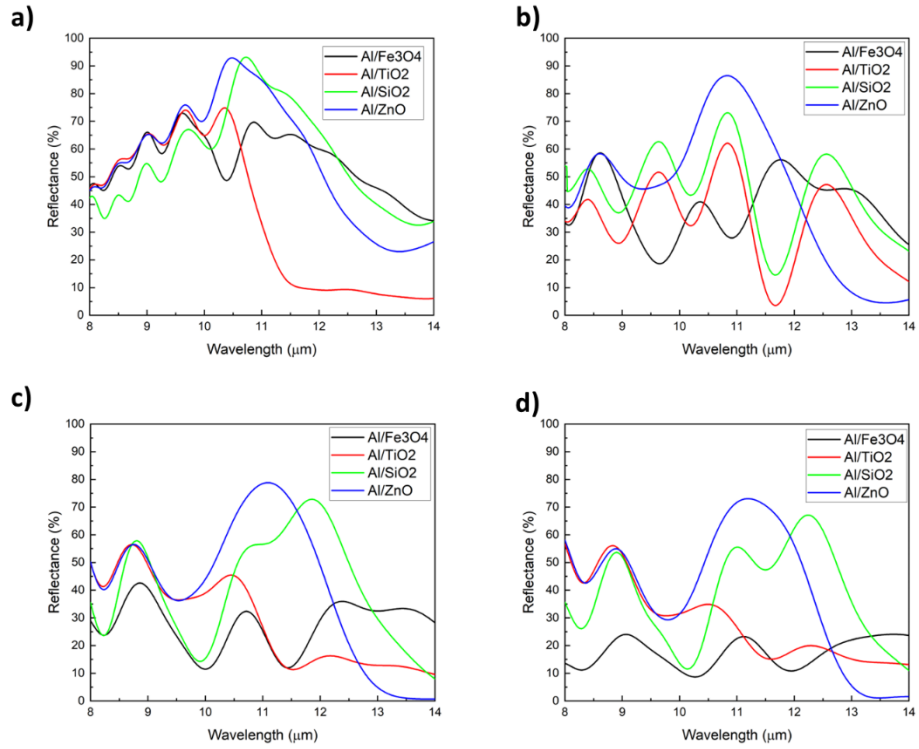

Figure 5.5 FDTD Simulation result for spectral reflectance for core/shell particles with a)100, b)200, c)300 and d)400 nm shell thicknesses.

As seen in the figures, the reflectance characteristics of Al particle were significantly influenced by the shell type and thickness. The results showed that the average reflectance of spherical pure Al particle was the lowest average reflectance when compared to core/shell particles at all shell thicknesses, as expected. The oxide shell structures decreased the reflectance of Al particle. Average reflectance of spherical pure Al was calculated as 65% in 8-14 μm waveband. The average reflectance values of the particles in LWIR range are provided in Table 5.2.

Table 5.2 FDTD simulation result for reflectance of core/shell particles.

Shell Thickness	Reflectance (%)			
	Fe_3O_4	SiO_2	TiO_2	ZnO
100 nm	56.71	57.02	42.17	59.50
200 nm	39.47	41.40	34.76	48.51
300 nm	27.46	40.51	32.88	44.57
400 nm	16.95	37.83	32.39	42.81

It can be seen from Table 5.2 that the average reflectance values of core/shell particles decreased with an increase in the shell thickness. Among core/shell materials with specified thicknesses, Al/ZnO particle had the highest reflectance at each shell thickness.

ZnO shell showed the highest performance from the point of average reflectance compared to other shell materials for all thicknesses. As a material input, the refractive index determined the reflectance features. Therefore, Al/ZnO core/shell particles were decided to be synthesized for this study.

CHAPTER 6

EXPERIMENTAL PROCEDURE

Based on the results obtained from FDTD analysis, it was determined that Al/ZnO core/shell particles would be synthesized.

6.1 Materials

6.1.1 Aluminum (Al)

Aluminum is the most common metallic material on earth. It is widely used in industry for different purposes due to its low weight-to-volume ratio, high thermal and electrical conductivity, high reflectance, and resistance against corrosion by forming native oxide on the surface. The crystal structure of aluminum is face-centered cubic, the molecular mass is 26.99 g/mol, and the density is 2.699 g/cm3[122].

In the nanoparticle form, aluminum is used for combustion in rocket engines because of its high reactivity and calorific density. In the aerospace and automotive industry, aluminum and its alloys are used as a structural material due to their high specific strength and formability characteristics. In recent years, the reflectance of aluminum especially in the infrared region have drawn attention in stealth technology and it has become the critical component of stealthy coatings [21,123].

6.1.2 Zinc Oxide (ZnO)

Zinc oxide is a semiconducting metal oxide material with a direct band gap of 3.4 eV. Because of the unique structure especially at the nanosize, it is used in various applications such as solar cells, photocatalysis, biomaterials, optical coatings, photoluminescence applications, and magnetic structures[124,125]. ZnO with hexagonal wurtzite crystal structure is intensely studied due to its high thermodynamic stability, and outstanding optical and electrical features[125].

In recent years, besides its usage in the scope of IR low radiation, ZnO is studied for the purpose of radar absorbance. In a various studies, ZnO is investigated for enhancing radar absorbance while providing chemical stability to materials known as radar-absorbing materials such as FeCo[126], FeSiAl[127]. Because of the oxidation problem of metallic magnetic materials, ZnO has become preferable with its high abundance and simple fabrication routes. ZnO can also be doped with various metals to improve its magnetic and optoelectronic [124].

ZnO nanoparticles are generally synthesized by wet-chemical methods such as sol-gel[128] and hydrothermal/solvothermal[129] synthesis. Hydrothermal/solvothermal methods are environmentally friendly and allow particle size and morphology control [130].

6.2 Experimental Details

6.2.1 Materials Used

In the synthesis, the Al-micropowder with 10-20 μm size and >99.9% purity obtained from Nanografi Nano Technology Inc., Turkey was used. The zinc acetate dihydrate ($Zn(CH_3COOH)_2$) and sodium hydroxide from Merck, IsoLab GmbH absolute ethanol with >99.9% purity supplied from Sesim Kimya, Turkey. The

polyurethane with aerospace standard of MIL-PRF 85-285 was provided from TAI Inc., Turkey.

6.2.2 Solvothermal Synthesis

Solvothermal synthesis is one type of wet-chemistry method used for the synthesis of nanoparticles. The process is performed in the presence of organic solvents in which the chemical reaction, nucleation, and growth occur. The reaction is performed in an autoclave in which the precursors are placed into a solution placed in a sealed teflon container. The reaction takes place by supplying heat for a certain time in a furnace to the autoclave which generates autonomous-pressure[131]. When an aqueous solution is used instead of an organic solvent in the reaction, the process is defined as the hydrothermal synthesis. Organic solvents protect the precursors from harmless effects of water such as oxidation and provide lower reaction temperatures [131,132].

The main parameters for the process are reaction time, temperature, pH, pressure, and the type and concentration of precursors. When compared with other processes, solvothermal reaction allows synthesis of particles with high homogeneity, controlled size, shape and morphology in the particles without the need for post-treatment [133]. Synthesis takes place usually at a low temperature, besides it is environmentally friendly.

The process route for the hydrothermal synthesis of ZnO nanoparticles begins with the dissolution of Zn salt, zinc acetate dihydrate ($Zn(CH_3COOH)_2$) in an aqueous solution and preparing the aqueous alkaline solution with sodium hydroxide (NaOH) separately. The process continues with mixing the Zn salt solution with the alkaline solution, and the solution is processed in the autoclave for the hydrothermal reactio. During the process, the reactions are given below lead to the formation of ZnO nanoparticles[134]. Reaction (1) occurs when the Zn solution is introduced to an alkaline solution, and reaction (2) takes place during the autoclave process[135].

$$Zn(CH3COOH)_2 + 2NaOH \rightarrow Zn(OH)_2 + H_2O \quad (1)$$

$$Zn(OH)_2 \xrightarrow{\Delta T} ZnO + 2H_2O \quad (2)$$

The schematic illustration of process steps in the order of mixing, placing into autoclave, heating, centrifuging, separating, and drying, respectively, is shown in Figure 6.1.

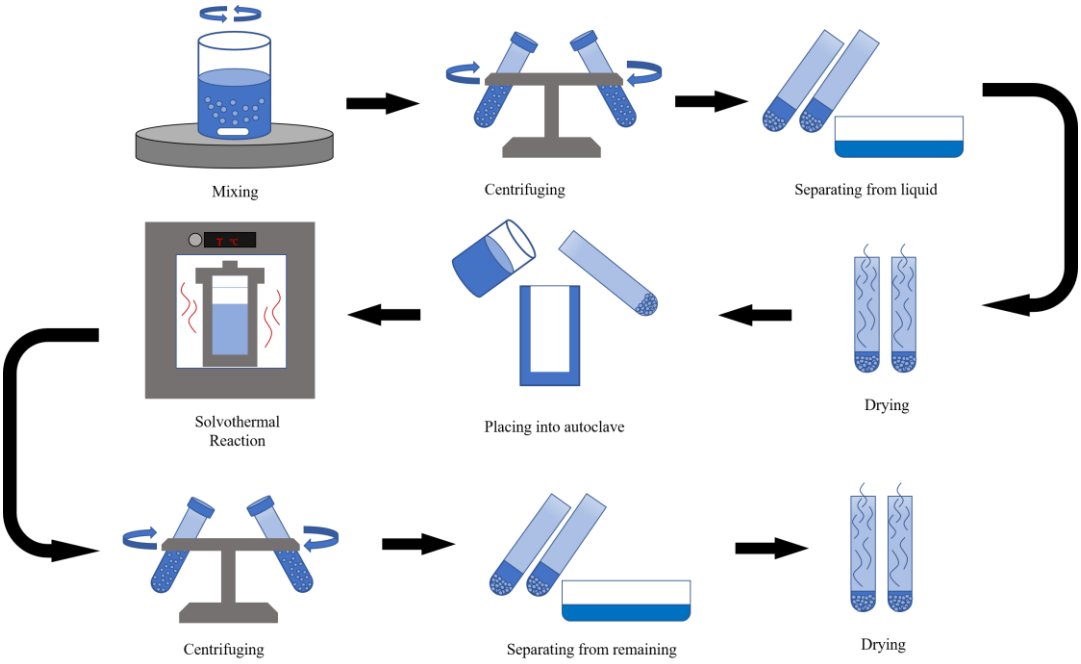

Figure 6.1 A schematic illustration of core/shell synthesis route.

The water-based solutions are highly aggressive for aluminum to form a native oxide on the surface[136]. Because of this situation, a solvothermal reaction was planned based on the procedures mentioned above in this study. In this regard, water was superseded by ethanol as the reaction solvent. The Al microparticles were added to the process at the dissolution step of Zn salt. As a Zn salt, zinc acetate dihydrate was used and the alkaline solution was prepared through dissolution of NaOH in deionized water.

6.2.3 Precursor Preparation

The synthesis was initiated by weighing the reactants according to the determined values shown in Table 6.1 below. $Zn(CH_3COOH)_2$ and NaOH were dissolved in 10 ml of deionized water separately using a magnetic stirrer at room temperature. Following the dissolution of zinc acetate dihydrate, Al microparticles were added into the solution under magnetic stirring. When the dissolution of NaOH was completed, 40 ml ethanol was added to the solution and stirred vigorously to obtain a homogenous colorless solution. The colorless solution was added into the Al-Zn^{2+} suspension slowly at a constant stirring rate until a homogenous honey-like mixture was formed. In this way, it was expected that the Al microparticles would be surrounded by Zn precursors and the organic compound would prevent Al oxidation. The suspension was centrifuged 3 times with ethanol at 6000 rpm for 6 minutes to separate the particles from the solution and placed in the oven at 80 °C overnight to eliminate the rest of the moisture and organic compounds. Finally, when drying was completed, the precursor of Al/ZnO core/shell particles was prepared. The process steps are shown in Figure 6.2, respectively.

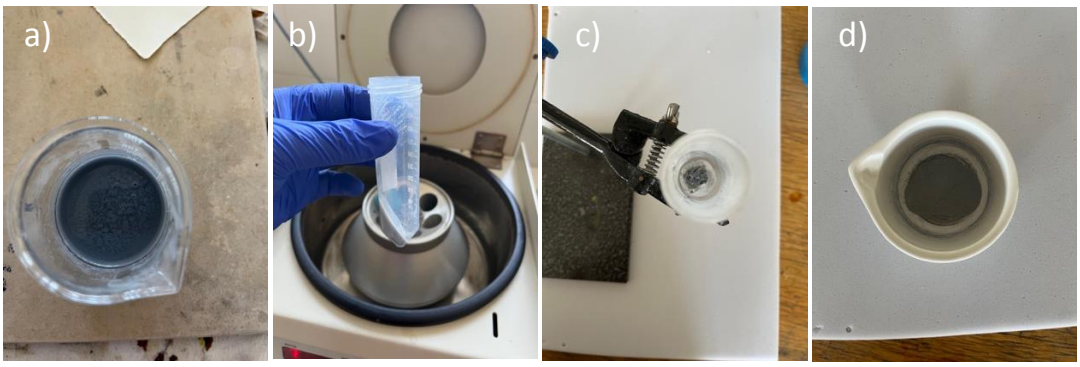

Figure 6.2 Photographs of the process steps for precursor preparation, a) forming of honey-like suspension, b) first centrifuge to obtain core/shell precursor, c) after drying, d) crushed with mortar.

In the natural environment, native oxide is found to form on the Al surface. The native oxide on the surface of Al particles could be dissolved in alkaline solutions

[137]. Therefore, NaOH solution was used as an alkaline solution within the precursor preparation step to remove the native oxide on the surface of Al particles.

Table 6.1 The sample nomenclature depending on molar and temperature parameters

Sample	Weight $Zn(CH_3COOH)_2$ (g)	Mole $Zn(CH_3COOH)_2$	Weight NaOH (g)	Mole NaOH	Reaction Temperature (°C)
S.1A	1.1	0.005	0.4	0.1	130
S.1B	2.2	0.01	0.8	0.2	130
S.1C	3.3	0.015	1.2	0.3	130
S.2A	1.1	0.005	0.4	0.1	150
S.2B	2.2	0.01	0.8	0.2	150
S.2C	3.3	0.015	1.2	0.3	150
S.3A	1.1	0.005	0.4	0.1	170
S.3B	2.2	0.01	0.8	0.2	170
S.3C	3.3	0.015	1.2	0.3	170

6.2.4 Solvothermal Reaction and Core/shell Powder Synthesis

The solvothermal reaction process was carried out with stainless steel autoclave with a Teflon container of 100 ml volumetric capacity. The dried precursor of Al/ZnO powder was first ground in a mortar to achieve finer particles and break the agglomeration. The crushed material was placed in the container, and as a reaction solvent, 75 ml of ethanol was filled into the vessel. The autoclave was heated in the oven at 150 °C, the temperature was kept constant for 8 hours, and cooled to room temperature. After the reaction was completed, the centrifugation process was performed 3 times with ethanol at 6000 rpm for 6 minutes to separate particles from

organics and dissolved residuals. The powder was dried in the oven at 80 °C for overnight to extract moisture and organics from the core/shell particles. Finally, the Al/ZnO core/shell particles were obtained. Photographs of the process steps are provided in Figure 6.3.

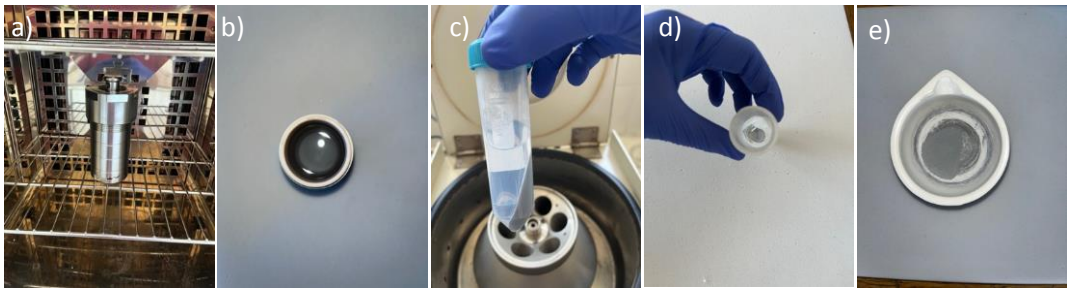

Figure 6.3 Photographs of process steps for core/shell particle synthesis a) autoclave reaction, b) after solvothermal synthesis, c) after centrifugation to seperate core/shell material, d) dried core/shell particles, e) powder ground in mortar.

Photographs of the synthesized powders (notated in Table 6.1 by varying the reaction temperature and Zn^{2+} ratio) are provided in Figure 6.4.

Figure 6.4 Photographs of the core/shell powder samples.

6.2.5 Tape Casting (Doctor Blade) Method

One of the commonly utilized methods for coating the materials as thin films is tape casting or the Doctor Blade process. It provides the ability to apply the coating on large surfaces. The method is initiated by placing the paste of ceramic particles suspended in a solution with other ingredients on the coating surface. The blade is moved from one substrate edge to the opposite edge. There is a gap between the substrate coating surface and the bottom of the equipment. When the process is completed, the material is coated on the substrate. The measure of the gap determines the wet coating thickness[138]. Doctor Blade method is schematically illustrated in Figure 6.5 below. The method provides a thin, dense film on the surface with one or more layers. By the application direction, the orientation of the particles can be regulated[139,140].

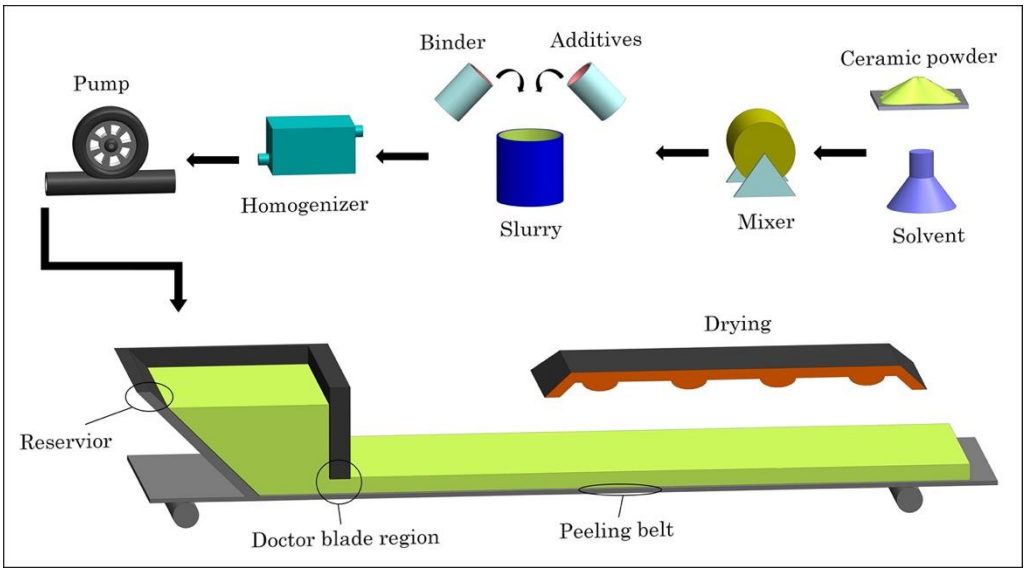

Figure 6.5. Schematic representation of Dr. Blade method[139].

Al/ZnO core/shell powders were mixed with the polyurethane binder and then tape casting method was used to deposit the prepared mix as a thin film on aluminum plates.

6.2.6 Sample Coating by Tape Casting

Bare aluminum and glass substrates were prepared by cutting, and cleaning with the size of 7 x 12 cm and 2.5 x 2.5 cm, respectively. The wet coating thickness was determined as 60 μm. The thickness of the AIRTECH adhesive tape was verified by calibrated micrometer as 60 μm. The periphery of the substrates was taped such that the coating area was 3 x 7 cm on the aluminum substrate and 2 x 2 cm on the glass substrate.

Each synthesized powder sample and the pure Al powder were mechanically mixed separately with PU-based polymer with an aerospace standard of MIL-PRF-85285, which is used as a topcoat on the aircraft fuselage, by 1/1 weight ratio. The mixing was continued until a homogeneous mixture of powders in polymer matrix was obtained. After mixing, the mixture was poured onto one substrate edge. The flat and smooth glass was drawn from one edge along the tape on both sides to the opposite

edge, in this manner the tape thickness created a gap between the substrate and the glass lamella. The mixture filled the gap during the process and the material was coated on the substrate in this way. Following the coating, the samples were held for 30 minutes for flash-off and placed into the oven for 3 hours at 65 °C with natural cooling. In addition, the PU without any filler was coated on the glass and aluminum substrates by the same method for comparison and the use of baseline in the characterization stages. Photographs of the process steps are shown in Figure 6.6.

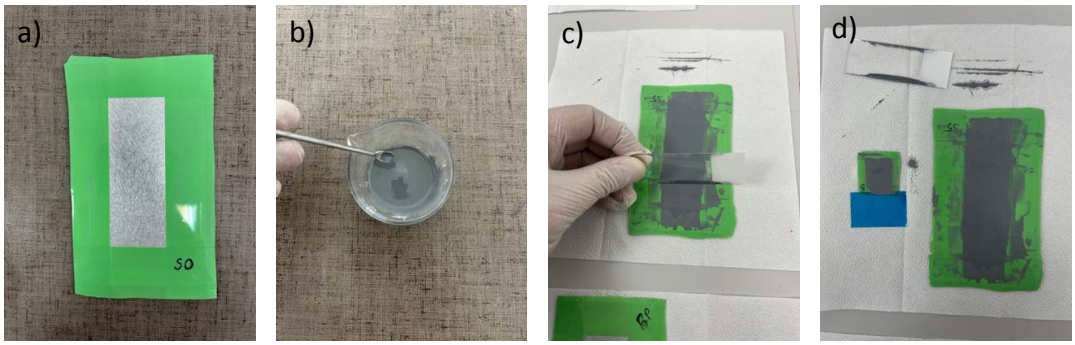

Figure 6.6 Photographs of tape casting process steps a) Taped aluminum substrate, b) powder mixing with binder, c) Tape casting, d) Drying before oven.

The photographs of coated samples of composites on aluminum plates are given in Figure 6.7 and 6.8 for reference materials as Al/PU and PU, and core/shell-filled PU composites, respectively. The coatings on the glass substrates are given in Figure 6.9 and 6.10 for reference coatings and core/shell-contained coatings, respectively.

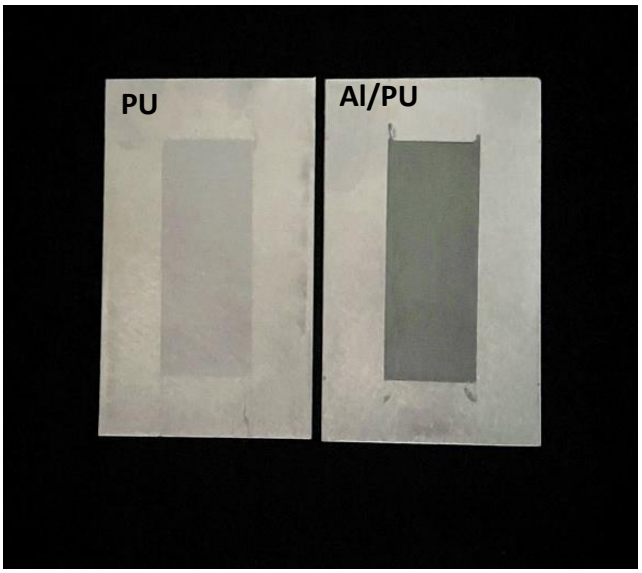

Figure 6.7 Photographs of PU and Al/PU coated samples.

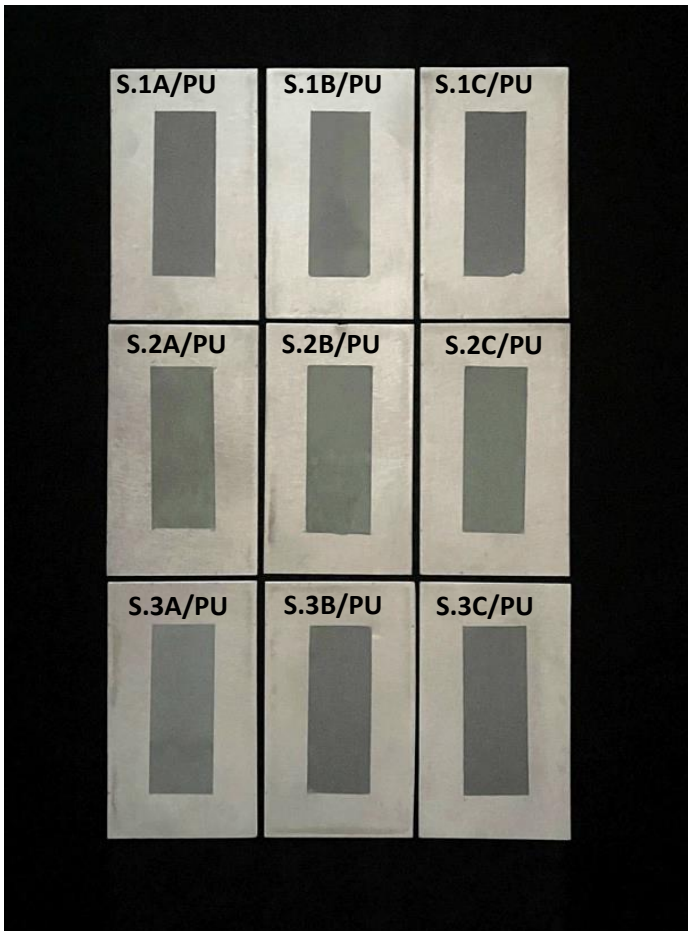

Figure 6.8 Photographs of core/shell/PU composite coatings on aluminum substrate.

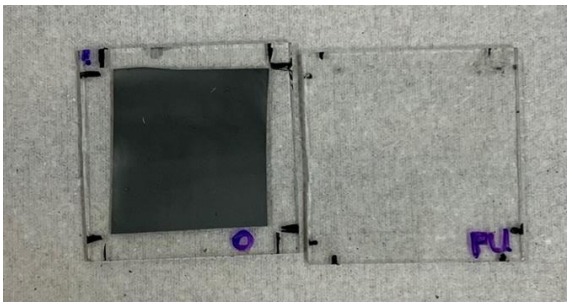

Figure 6.9 Photographs of Al/PU and PU coated glass substrates.

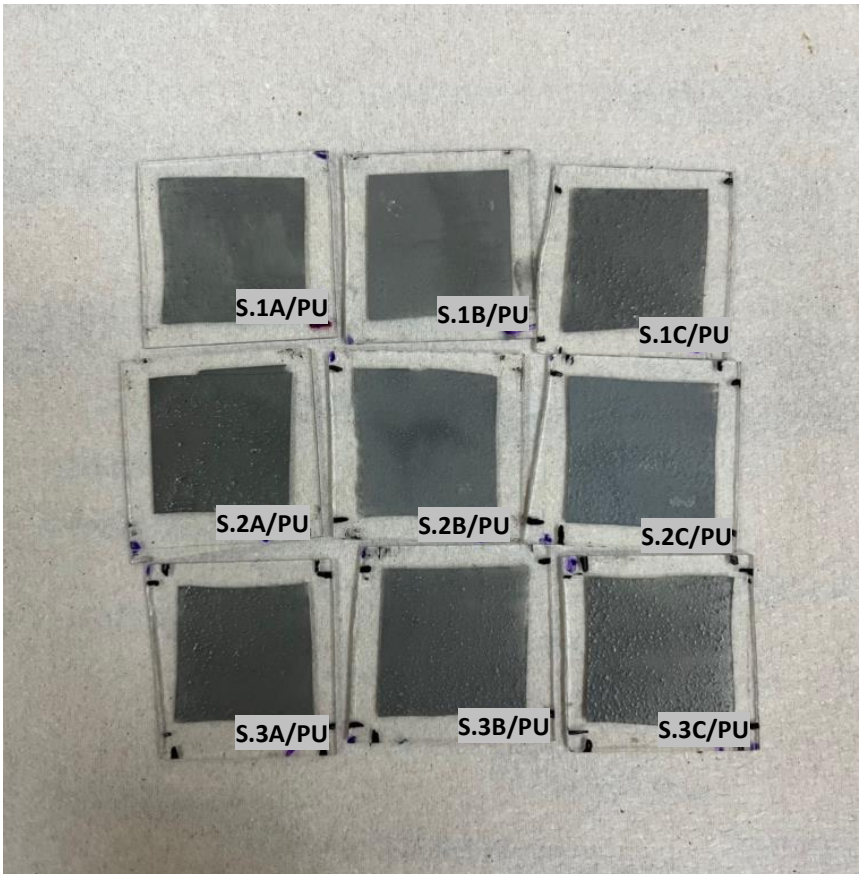

Figure 6.10 Photographs of core/shell/PU coated glass substrates from S.1A to S.3C

The core/shell sample of S.2A was mixed with PU binder by varying the filler fraction (filler/binder) from 0.5 to 2 by increasing 0.5 to investigate the effect of filler fraction on LWIR emissivity of the material. The reason for the use of S.2A in this application is discussed in detail in Chapter 7.5. In order to compare with pure-Al,

Al/PU composite coatings were prepared equal weight ratios with core/shell composites. Photographs of the prepared coatings are given in Figure 6.11.

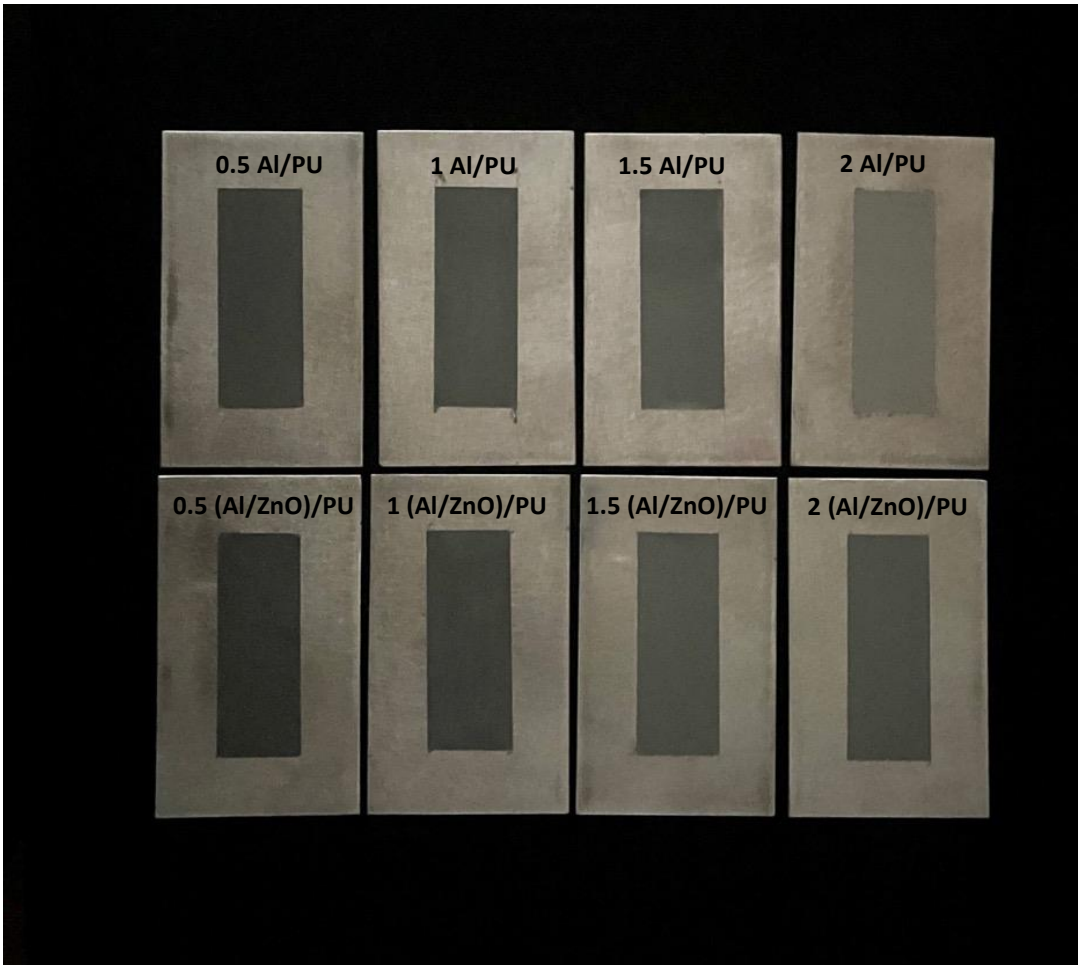

Figure 6.11 Photographs of Al/PU and S.2A/PU coated aluminum substrates with different filler contents.

6.3 Characterization

6.3.1 X-ray Diffraction (XRD)

The crystal structure analysis of the synthesized core/shell particles was performed using XRD method. The instrument used for characterization was Rigaku Ultima-IV X-ray Diffraction Device in METU Central Laboratory. The equipment conducts the

analysis from the surface of the sample under CuKα radiation at the wavelength of 1.5406 Å. The characterization was conducted to observe the chemical composition and crystalline structures of the powders depending on the reaction temperature and the Zn content. The analysis was carried out between the angles of 2θ=10-90°, and the scanning rate of 1°/min.

6.3.2 Scanning Electron Microscopy (SEM)

The pure Al powder, the synthesized Al/ZnO core/shell powders, and S.2A/PU core/shell composite coating on glass substrate at 2/1 filler fraction were subjected to SEM analysis to compare the morphological differences between bare Al and the Al/ZnO particles. In addition, shell morphology and distribution of the ZnO in core/shell particles were compared in core/shell powders. The Al/ZnO powder samples and composite coating were coated with a gold layer with 5-10 nm thickness to conduct the SEM analysis. The analysis of powders was carried out with QUANTA 400F Field Emission SEM instrument in METU Central Laboratory. The applied accelerating voltage during the characterization was 30 kV. The coating SEM analysis was conducted with FEI Nova Nano SEM 430 instrument in METU Metallurgical and Materials Engineering department.

6.3.3 Energy Dispersive X-Ray (EDX) Spectroscopy

EDX spectra and EDX mapping were obtained during SEM analysis to monitor the present elements and their weight ratios at the atomic scale in the powder and whether the core/shell structure in the prepared powders consists of Al, Zn, and O.

6.3.4 Fourier-Transform Infrared Spectroscopy (FTIR)

FTIR analysis was performed in the wavelength range of 8-14 μm with Bruker Vertex 80 Fourier-Transform Infrared Spectroscopy integrated Attenuated Total

Reflectance (ATR) and reflectance equipment. The characterization was carried out to measure and compare spectral absorbance/reflectance characteristics of pure Al and synthesized powders, and composite coatings including PU with Al and Al/ZnO coated substrate. The ATR equipment was used for the powder and composite coating samples on glass substrates. In addition, the composite coatings on the aluminum substrates were analyzed. The reflectance instrument was utilized to measure the reflectance of the composite films coated on the aluminum substrate at an oblique angle.

6.3.5 UV-Vis Spectrophotometry

Total reflectance (specular and diffuse) of PU-matrixed composite coatings with Al and Al/ZnO particles on the glass substrates were obtained with Shimadzu UV-1800 model UV–Vis spectrophotometer. The optical measurement was conducted in the visible band of 380-720 nm. Before the absorbance analysis, the PU-coated glass sample was used as a baseline. The reflectance spectra were obtained by the surface of the samples.

6.3.6 Thermal Imaging

The IR radiation characteristics of the samples of PU, Al/PU and Al/ZnO/PU was measured by the thermal camera at 60, 80, and 100 °C background temperatures. The setup was prepared with a calibrated hot plate and a thermal camera. The thermal camera was fixed with a clamp 50 cm above the hot plate and focused on the hot plate. The hot plate was heated to 60, 80, and 100 °C, and the temperature value on the screen of the hot plate was verified by a thermocouple placed on the hot plate. At the same time, the temperature of the hot plate was measured by the IR camera. It was observed that the actual temperature seen on the screen and the temperature of the hotplate was in good agreement. Therefore, the hotplate surface was accepted as the blackbody with an emissivity value of 1. The IR temperature measurement was

conducted by placing the samples on the hot plate. It was waited for the hot plate to reach the constant temperature of 60, 80 and 100 °C, for approximately 10 minutes. The process was repeated for each sample. A photograph of the measurement setup is provided in Figure 6.12.

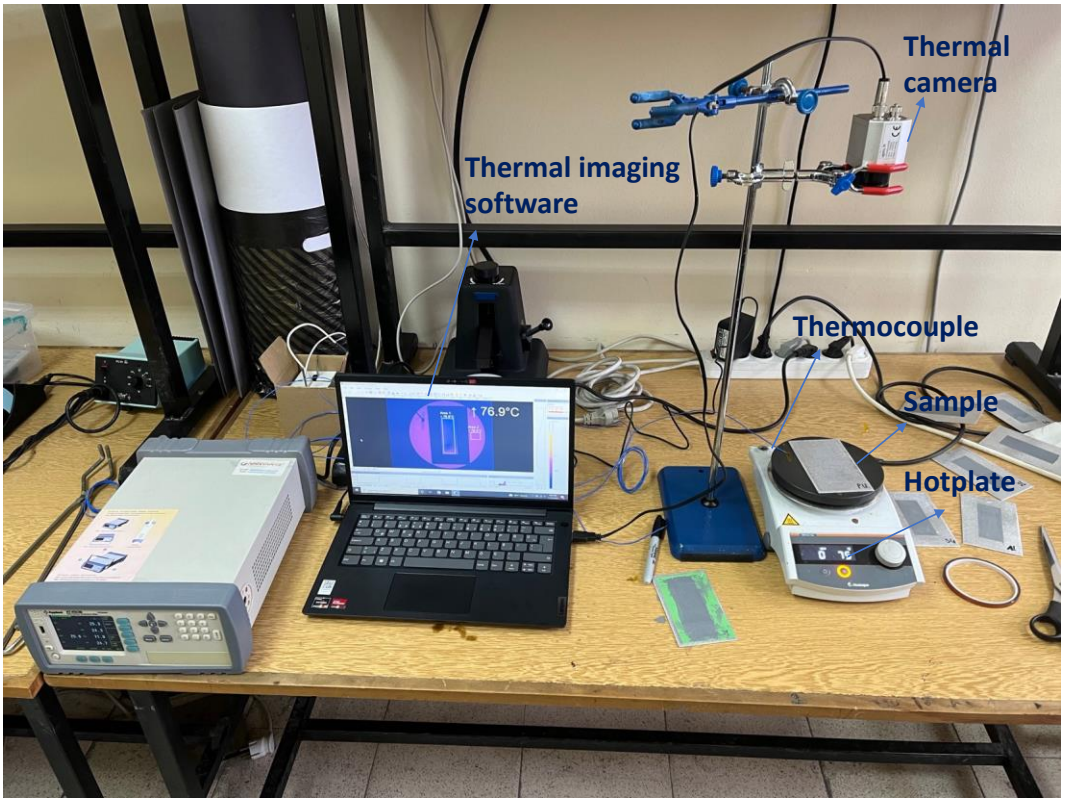

Figure 6.12 A photograph of the thermal imaging setup used in this work.

6.3.7 Radar Absorbance Measurement

In order to examine the radar absorbance performance of core/shell powders, the PU-matrixed composite material with core/shell particles were coated on a glass substrate with the size of 1x2 cm. To compare the performance of core/shell filled composite, pure-Al/PU coating was also prepared. The weight ratio of filler to binder was adjusted as 2/1, since the lowest emissivity obtained in this fraction by thermal

imaging (Chapter 7.5). The test was conducted with KEYSIGHT ENA Network Analyzer between the frequencies of 8.2-12.2 GHz, named as X-band[141] and utilized in radars for air-defense. Photographs of the test samples are provided in Figure 6.13.

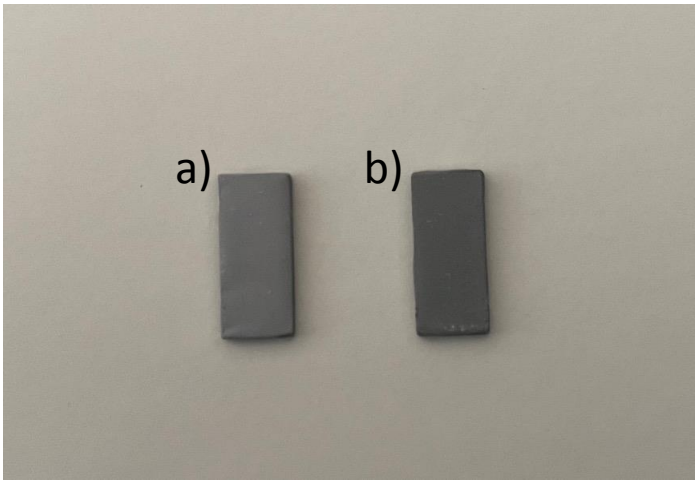

Figure 6.13 Photographs of a) Al/PU and b) (Al/ZnO)/PU samples for X-band radar absorbance measurements.

CHAPTER 7

RESULTS

The characterization and performance test results of the prepared samples are provided and explained in this chapter.

7.1 X-Ray Diffraction

The XRD patterns of the 9 samples of Al/ZnO core/shell powders with different ZnO molar ratios and reaction temperatures are given in Figure 7.1. The XRD peak intensities were normalized based on the highest peak among all samples. The Al and ZnO peaks were observed in the XRD pattern for each sample without any impurities. In the XRD pattern of each sample, the presence of Al and ZnO diffraction peaks indicates that crystal-structured ZnO has formed on the Al micro-powders, and the Al particles were protected from oxidizing.

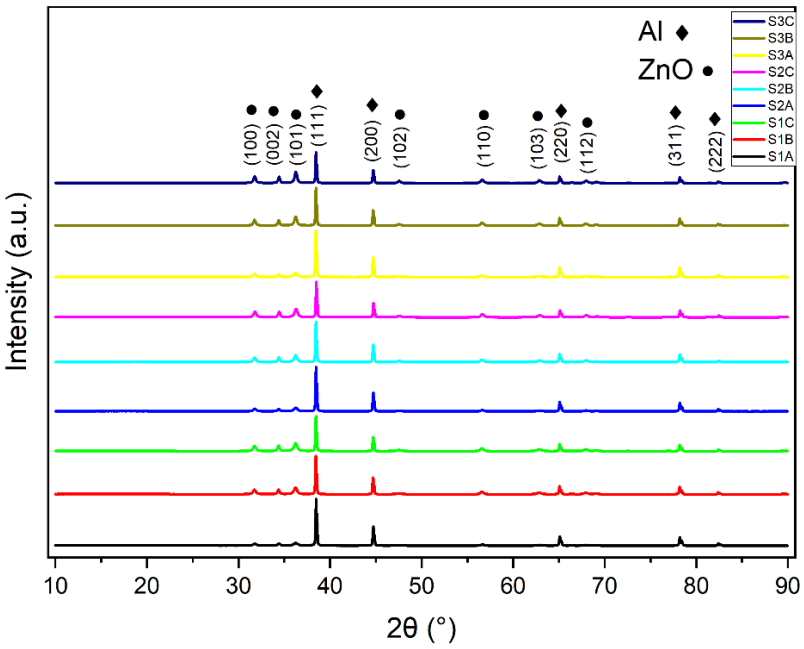

Figure 7.1 XRD patterns of core/shell powders.

In the figure, the FCC crystal-structured Al characteristic peaks represent the miller indices of (111), (200), (220), (311) and (222). The XRD pattern of Al was verified from the literature[142,143]. XRD pattern of ZnO demonstrated formation of the hexagonal wurtzite structured crystalline ZnO. The first 3 strongest diffraction peaks specify the (100), (002), and (101) miller indices of ZnO, respectively. The peak positions of ZnO were consistent with the literature[144,145].

The increase in the reaction temperature and the molar content ratio of Zn^{2+}/Al resulted in the rise of the peak intensity of ZnO in the XRD spectra. Observation of the strong peaks at high temperatures can be explained as the promotion of crystallization [146]. On the other hand, the change in the molar ratio of Zn^{2+}/Al, or ZnO-content in the powder, influenced the peak intensity more than the changes in the reaction temperature.

The crystallite size of ZnO structures on the shell layer were calculated by Scherrer Equation[147] 7.1 expressed below.

$$D = \frac{K\lambda}{\beta\cos\theta} \quad (7.1)$$

where, D (nm) represents the crystallite size, K specifies the shape factor, which is given as 0.9, λ (0.15406 nm) is the wavelength of utilized X-ray (CuKα 1.5406 Å), β (rad) is the full width at half-maximum, and θ (rad) is Bragg angle.The calculated mean size of nanoparticles are shown in Table 7.1.

Table 7.1 Calculated crystallite size of samples.

Sample	Crystallite Size
S.1A	27.96
S.1B	28.33
S.1C	29.59
S.2A	31.45
S.2B	34.71
S.2C	35.96
S.3A	37.26
S.3B	40.26
S.3C	41.94

It can be seen that the crystallite size of samples increases as the reaction temperature rises.

7.2 SEM-EDX Characterization

SEM images of starting pure Al and prepared powder samples varying the reaction temperature and ZnO-content are given in Figures 7.2 and 7.3 (a)-(i). It can be seen that regardless of temperature and molar ratio differences, SEM images of particles demonstrated the formation of core/shell particles. The ZnO nanoparticles were homogeneously grown to the surface of Al particles.

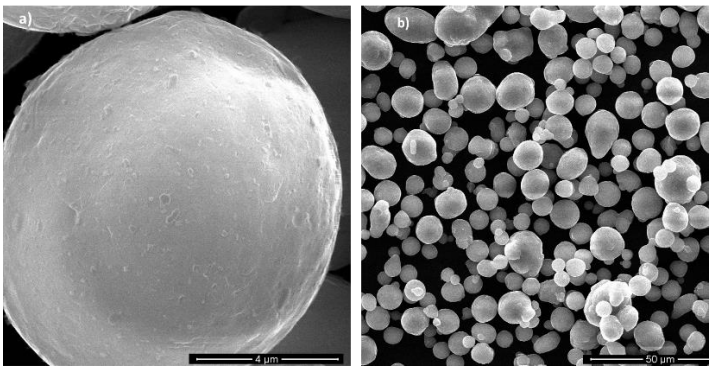

Figure 7.2 SEM images of pure Al particles under different magnifications.

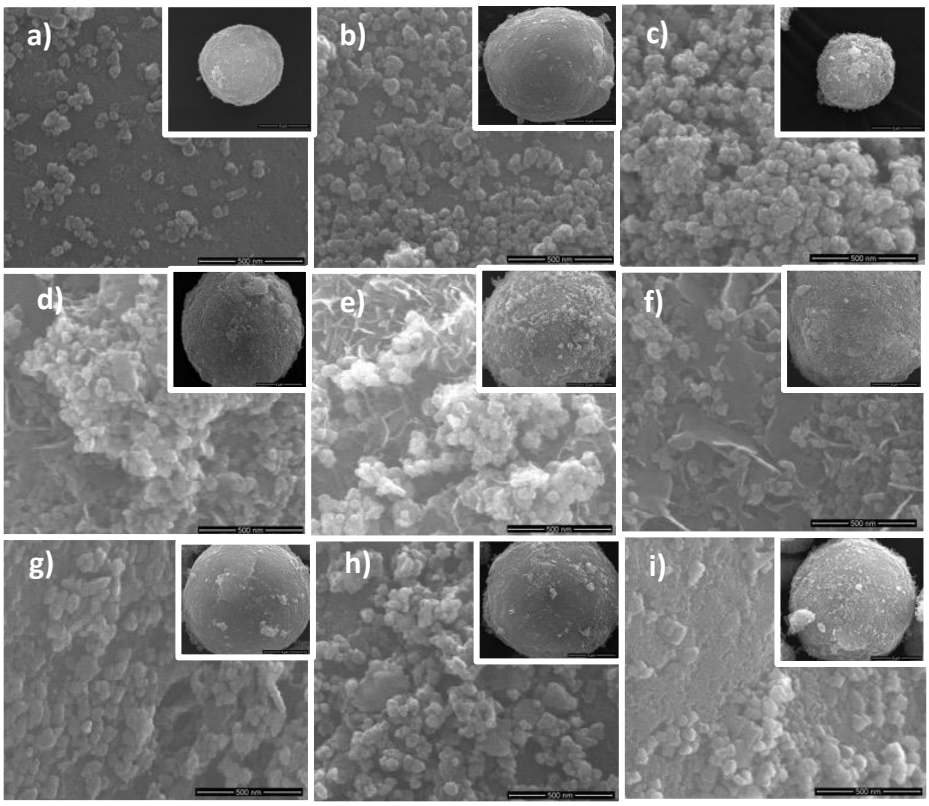

Figure 7.3 SEM images of core/shell particles of a) S.1A, b) S.1B, c) S.1C, d) S.2A, e) S.2B, f) S.2C, g) S.3A, h) S.3B, i) S.3C at different magnifications.

As seen from the inset images, pure Al particles were coated by ZnO nanostructures. In Figures 7.3 (a), (b) and (c), ZnO nanoparticles with spherical morphology covered the Al particles. When the reaction temperature is increased to 150 °C, flaky nanostructures of ZnO begin to form as can be seen in Figures 7.3 (d), (e), and (f). In addition, it is seen that some of the spherical structures still remain in the structure.

With the further increase of reaction temperature, agglomerated regions are observed on the shell structure, which can be seen in Figures 7.3 (g), (h) and (i).

During SEM analysis, the EDX maps were acquired for a composite particle to investigate the elemental distributions on its surface. SEM image and EDX maps of S.2A core/shell particle is provided in Figures 7.4 (a)-(d), for Al, Zn and O elements, respectively.

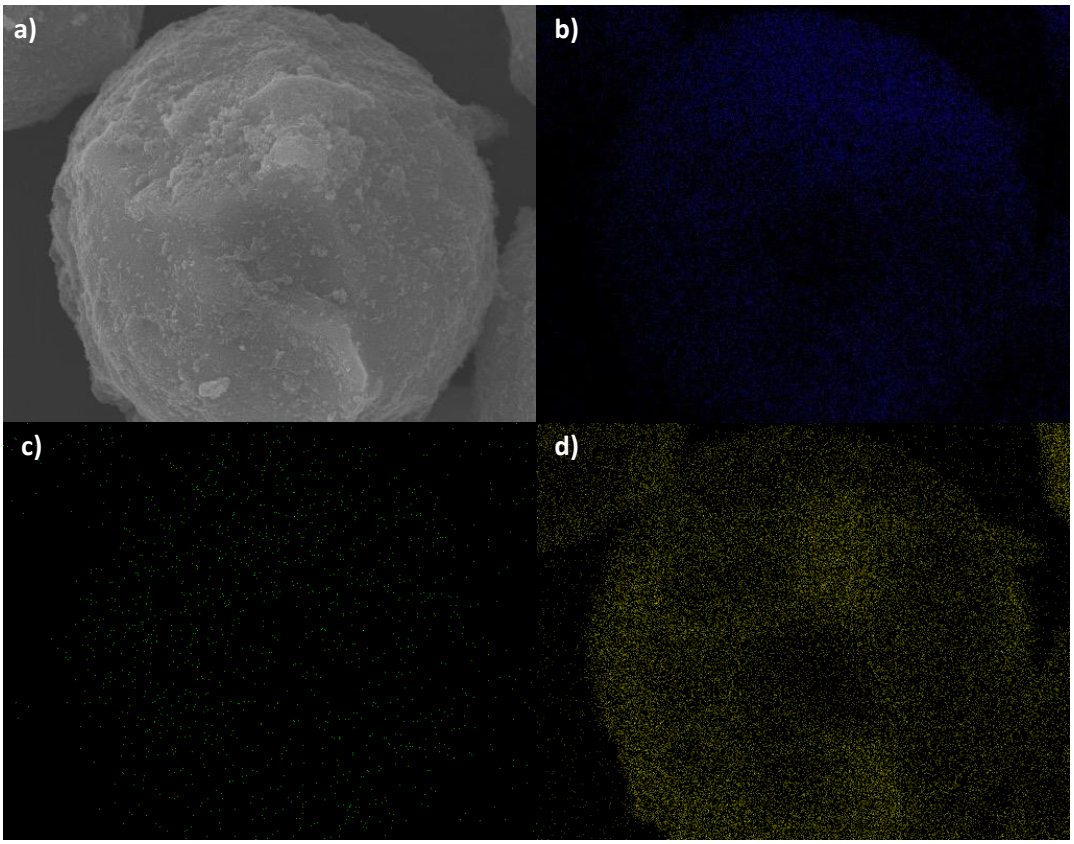

Figure 7.4 EDX maps of an Al/ZnO core/shell particle. a) SEM image of the selected S.2A particle and b) Al , c) O and d) Zn distribution map.

As can be seen in the figures, presence of the Zn and O elements were verified on the Al particle, and Zn and O are distributed homogenously on the Al particle. These images showed that the ZnO has covered the Al particle. EDX spectra of samples were obtained to analyze the elemental distribution of the materials and compare the Zn variations with the change in an atomic ratio in experiments. The EDX spectra of the S.2A, S.2B, and S.2C samples are shown in Figure 7.5 (a)-(c).

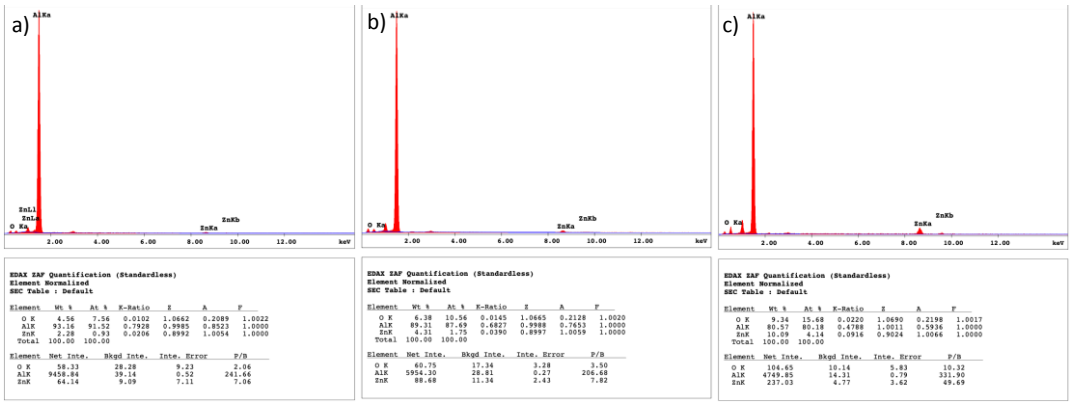

Figure 7.5 EDX spectra for a) S.2A, b) S.2B and c) S.2C samples.

Al, Zn and O peaks are seen on all the spectra. The atomic ratio of Zn in the structure is increased with the molar ratio of Zn-salt used in the synthesis. Additionally, stoichiometric mismatches between Zn and O were observed in all results due to the higher atomic content of O than that of Zn. The reason for this can be explained as the native oxide layer could be formed on uncovered surfaces of Al particles, or the results could be influenced by testing environment.

To investigate the particle distribution in PU binder, cross-sectional SEM images of S.2A/PU core/shell composite with a filler fraction of 2/1 on glass substrate were obtained. Cross-sectional SEM images of the coatings are provided in Figures 7.6 (a)-(c).

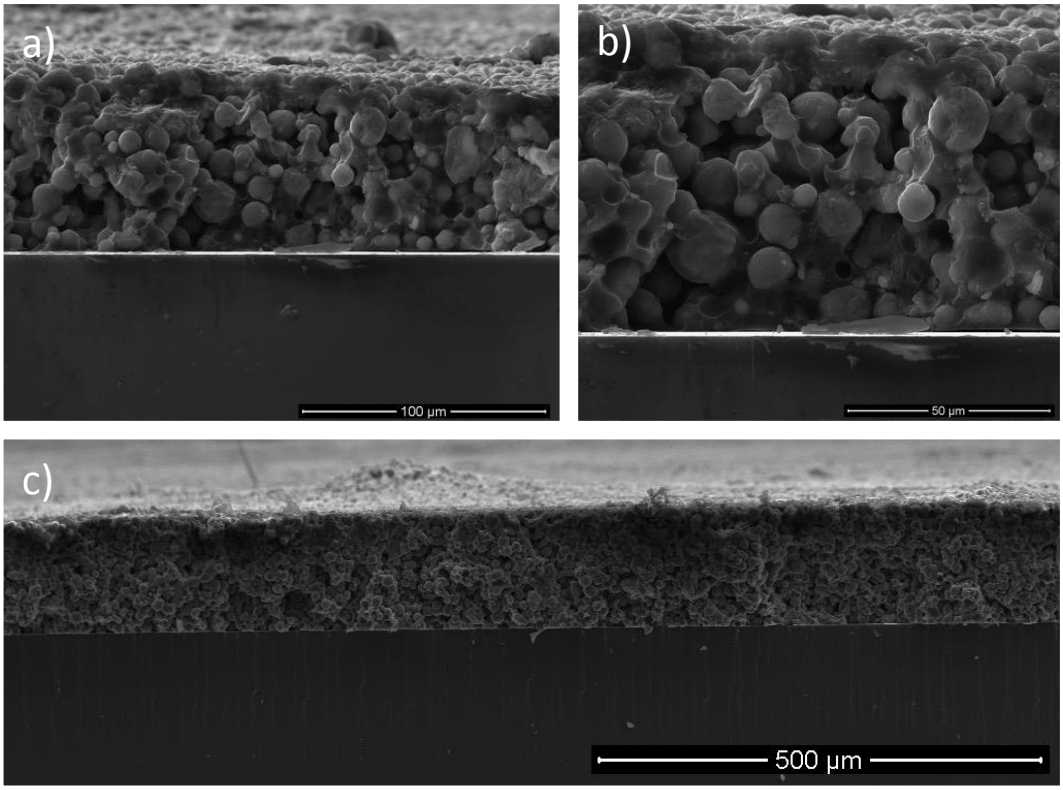

Figure 7.6 (a), (b), (c), Cross-sectional SEM images of S.2A/PU core/shell composite coating at a filler fraction of 2/1 on glass substrate at different magnifications.

As seen in the figures, the Al/ZnO (S.2A) core/shell particles were found to be homogenously distributed in the PU polymer matrix.

7.3 FTIR Spectroscopy

The FTIR transmittance spectra of pure Al and synthesized core/shell powders and coatings with PU matrix on the glass were obtained in the LWIR band with ATR equipment to investigate the absorption features of the samples. In addition, the reflectance of the coatings on aluminum substrates were investigated with a reflectance instrument at oblique incidence. The spectral transmittance of the powder is shown in Figure 7.7.

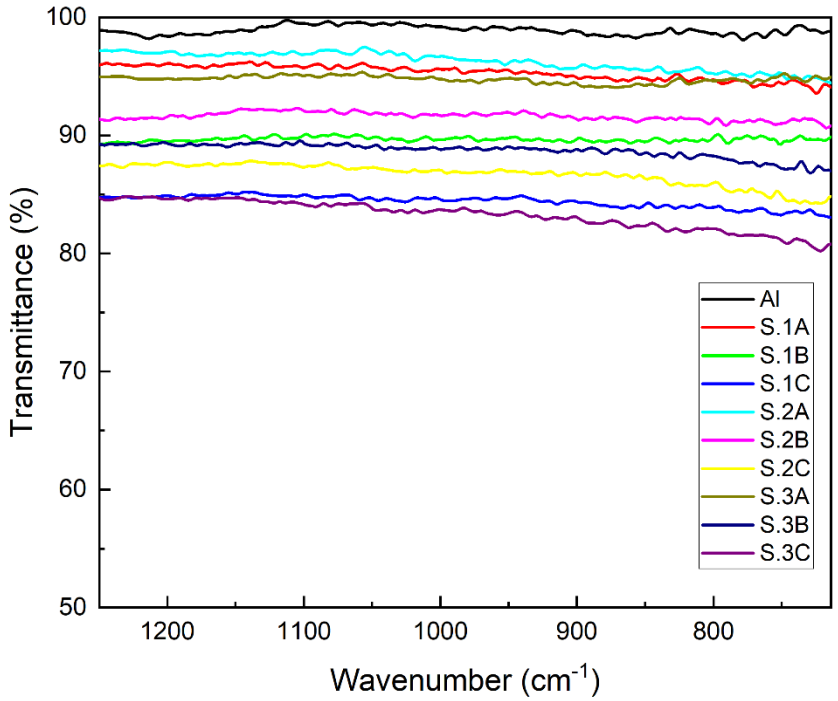

Figure 7.7 FTIR spectral absorbance of powders samples.

As can be seen in the spectrum, the Al and Al/ZnO powders showed similar spectra with different transmittance and no sharp peaks are observed within the 714-1250 cm^{-1} wavenumber (8-14 μm) range. Throughout the spectra, the lowest absorbance was observed on the Al powder. Among the core/shell powders, S.2A, S.1A and S.3A showed lower, S.2C, S.1C and S.3C had higher absorbance spectra, respectively. The ZnO-content in the core/shell powders and the synthesis temperature affected the absorbance characteristics of the samples. When the samples containing an equal ZnO content were compared, the shell morphology become dominant parameter for the absorbance characteristics. Therefore, the powders with flaky-shaped shell structure had lower absorbance than the powders with spherical morphology for each powder with equal ZnO content. When the particles with similar shell structure and equal ZnO content investigated, the crystallite size influenced the absorbance features of the samples. Among them, the powders have larger crystallites had higher absorbance. As explained in Chapter 3,

if an opaque material has low absorbance, its reflectance is high. High reflectance in defined wavelength range provides low emissivity. The material's low emissivity offers low radiation in the specified waveband. The average absorbance values of samples were calculated with spectral transmittance data obtained from samples according to principle of conservation of energy.

Among the core/shell samples, S.2A, which contains a low-content and partially flake-shaped ZnO shell, displayed the lowest absorbance value of 0.04 as average. On the other hand, S.3C showed the highest absorbance due to its high molar ratio, spherical ZnO morphology and higher crystallite size. As discussed above, increasing the Zn molar ratio in the powder causes the sample's IR absorbance to increase. As a result, the shell molar ratio, morphology, and crystallite size influenced absorbance features of the powders, respectively.

The FTIR transmittance spectra of coated glass substrates with Al/PU and Al/ZnO /PU composites were obtained by ATR equipment. The spectral transmittance within the 714-1250 cm^{-1} wavenumber (8-14 μm) is provided in Figure 7.8.

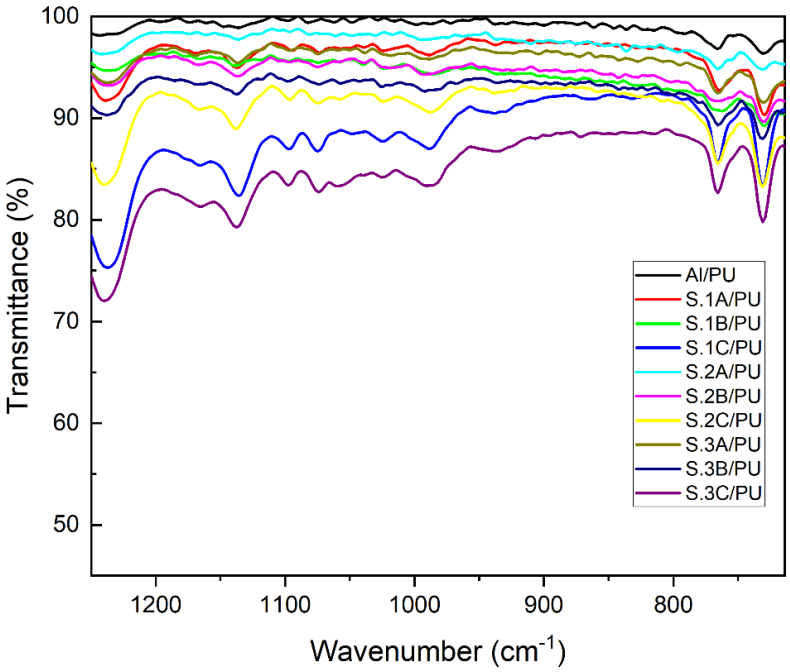

Figure 7.8 FTIR spectral transmittance of composite materials coated on glass substrate.

In the spectrum, although it was observed additional peaks, the coatings displayed consistent spectra with the powders. The peaks that come from PU binder at the bands 1200-1250 cm^{-1} (C-H and N-H), 1100-1150 cm^{-1} (C-O-C), 950-1050 cm^{-1} and 714-800 cm^{-1} (N-H and C-O) were observed in the spectrum. The PU-related peaks were verified from the literature[148,149]. The 2 lowest absorbances were observed in Al/PU and S.2A Al/ZnO/PU coatings, respectively. The average absorbance was calculated as 0.04 in S.2A/PU. The average absorbance characteristics of composite coatings with PU matrix are in good agreement with powders. In this way, it was observed that the particle absorbance features are also effective in the form of composite coating.

The spectral reflectance of the samples on aluminum substrates were obtained using a reflectance instrument in FTIR at oblique incidence (Figure 7.9).

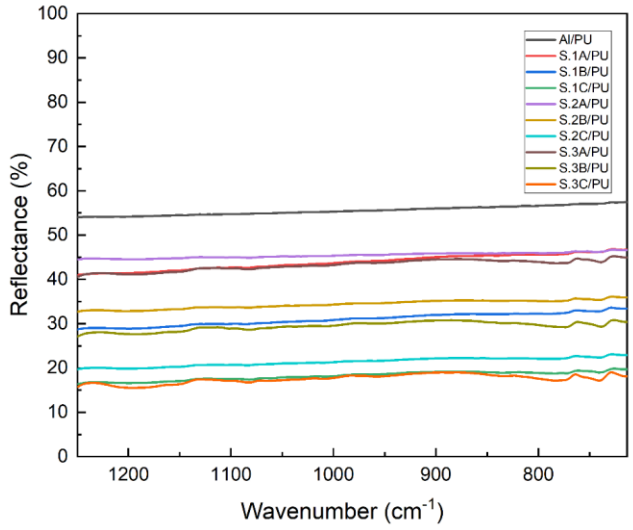

Figure 7.9 FTIR reflectance of composite coatings with respect to wavenumbers.

Samples showed linear and nearly constant reflectance without any sharp peaks. In the reflectance spectra, the Al/PU sample had the maximum reflectance along the waveband, the closest one is S.2A/PU to Al-containing sample. The average reflectance values of the samples are provided in Table 7.2.

Table 7.2 Average FTIR reflectance of coatings on aluminum substrates.

Sample	Average reflectance (%)
Al/PU	55.52
S.2A/PU	45.45
S.1A/PU	43.89
S.3A/PU	43.21
S.2B/PU	34.38
S.1B/PU	31.00
S.3B/PU	29.43
S.2C/PU	21.38
S.1C/PU	18.21
S.3C/PU	17.55

The sample with the highest reflectance was measured as the Al/PU composite. Among the core/shell composites, S.2A had the highest reflectance, while the S.3C was the one with the highest absorbance.

When the core/shell composite coatings compared with each other in terms of LWIR absorbance/reflectance characteristics, ZnO content in the core/shell influenced significantly the average reflectance features. At an equal content, the morphology and the crystallite size of shell determined the reflectance features of the samples, respectively. The average reflectance values in visible band and the FTIR transmittance results in LWIR were in clear accordance. The lowest reflectance in S.2A sample was attributed to low-content ZnO and flaky-shaped shell structure in the powder. As the literature stated, flaky-structured ZnO nanomaterials have the lowest absorbance rate as average by comparing with spherical nanoparticles[97]. As a result, the highest average reflectance was observed in Al/PU with 55.52%, as expected. As a result of using Al/ZnO core/shell powder instead of Al powder in the composite coating, a minimum decrease of 10.07% was observed in the average reflectance, with an average reflection rate of 45.45% of S.2A.

7.4 UV-Vis Spectrophotometry

In order to investigate and compare average visible reflectance of the composite coatings on the glass substrate, the total (specular and diffuse) reflectance within 380-720 nm wavelengths were obtained using a UV-Vis spectrophotometer. The spectral reflectances of the samples are provided in Figure 7.10.

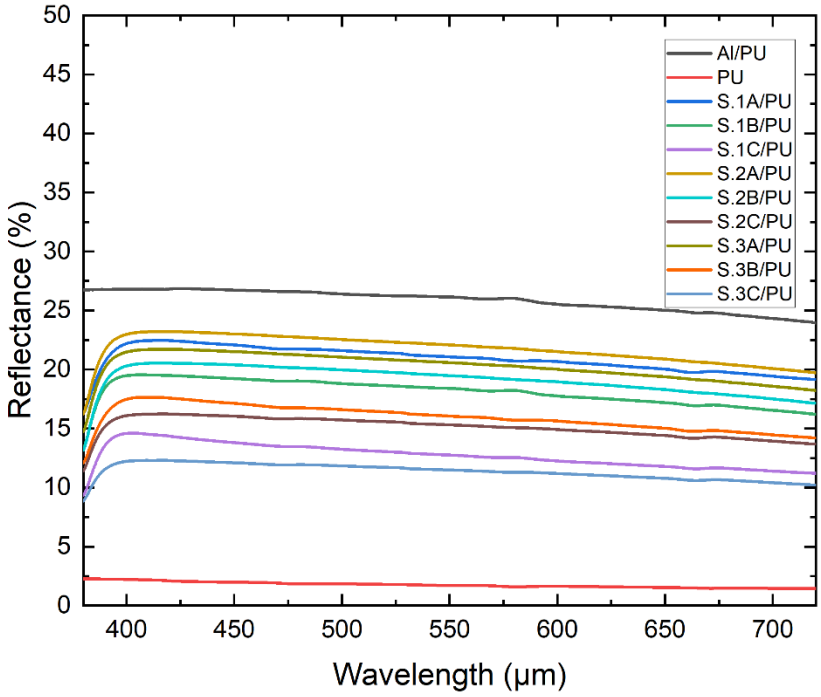

Figure 7.10 Visible reflectance of the samples.

According to the spectrum, the composite film with Al particles has the highest reflectance for each wavelength, without any sharp peaks at any specific wavelength, as expected. A sharp decline was observed for the core/shell composite samples when the wavelength approaches to 380 nm. The ZnO-containing particles with strong absorbance at approximately 380 nm were due to the band gap of the ZnO[150]. It was observed that more ZnO gave a higher absorbance in the visible band. The reflectance properties of the materials were affected by differences in content, morphology and crystallite size of the shell structure in the powders, similar with IR reflectance results. Therefore, the composite coating of S.2A/PU has the highest reflectance among core/shell composites. When the core/shell composites with spherical-shaped shell structures compared at equal ZnO content, higher crystallite size in the shell structure caused to lower reflectance in visible range. As literature stated, sheet-like ZnO nanoparticles has higher absorbance than spherical-shaped

nanoparticles[151]. The visible average reflectance values of the samples are tabulated and provided in Table 7.3.

Table 7.3 Average visible reflectance of coatings on glass substrate.

Sample	Average reflectance (%)
Al/PU	25.88
S.2A/PU	21.78
S.1A/PU	20.91
S.3A/PU	20.28
S.2B/PU	19.17
S.1B/PU	18.12
S.3B/PU	15.95
S.2C/PU	15.13
S.1C/PU	12.73
S.3C/PU	11.38
PU	1.76

According to results, while the lowest reflectance was measured for the sample of S.3C/PU, the Al/PU composite coating had the highest reflectance of 25.88%. Low reflectance in the visible band was caused by the high crystallinity and spherical form, as well as its high ZnO concentration. As low reflectance in the visible range is desired for the coating, S.3C/PU demonstrated the highest performance. However, it cannot be preferred as main powder because of having poor performance in the IR range. Although S.2A/PU had the highest reflectance among the core/shell composites, it was observed that the average reflectance was decreased by 4.10% when compared to Al/PU. The core/shell powders provided lower reflectance of the coating in the visible region, as desired.

7.5 Thermal Imaging

A thermal imaging setup was prepared to investigate the emissivity of the composite materials with PU-matrix with a 1/1 weight ratio of Al and Al/ZnO particles coated on an aluminum plate. The IR temperatures of the materials were obtained and compared to that of the background temperatures (60, 80 and 100 °C). The thermal images of the samples with background temperatures of 60, 80 and 100 °C are provided in Figures 7.11 (a) – (c), respectively.

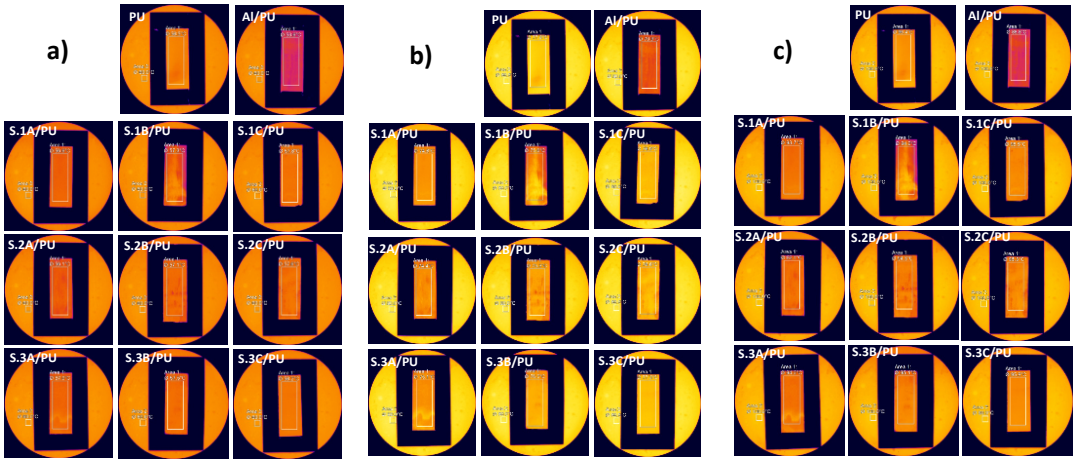

Figure 7.11 Thermal images of samples at a) 60, b) 80, c)100 °C background temperatures.

The change in the IR measured temperatures of samples are plotted and provided as bar chart in Figures 7.12 (a) and (b).

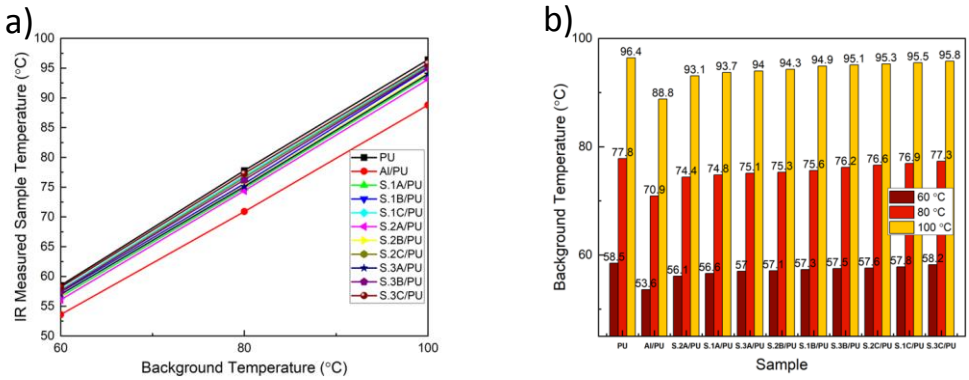

Figure 7.12 IR measured temperature of samples at 60, 80, and 100 °C background temperatures. a) plot. Lines are for visual aid., b) bar chart.

According to the figures, the temperatures of the samples were increased with the background temperature. The coldest material was observed as the Al/PU composite material, as expected.

According to the results, at each background temperature, the Al/PU composite had the lowest temperature. S2.A/PU had the lowest IR temperature among the composite materials with core/shell particles. The changes in the emissivity of the samples at 60, 80 and 100 °C background temperatures are provided in Figure 7.13.

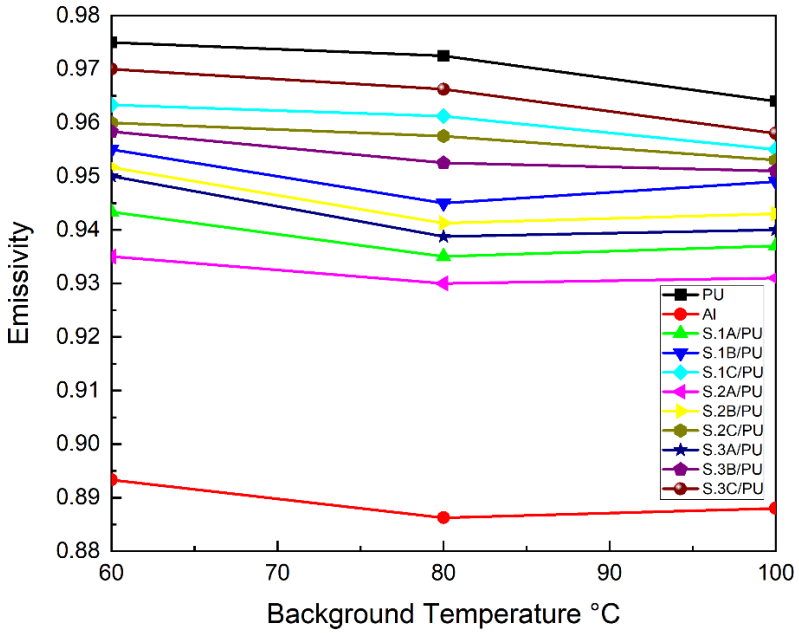

Figure 7.13 Changes in the emissivity of samples depending on the background temperature. Lines are for visual aid.

The emissivity value was calculated by dividing the IR temperatures of the materials by the background temperature since the emissivity is explained as the ratio of the gray (real) body radiation energy to the blackbody radiation energy at equal conditions, as Planck and Stefan-Boltzmann Laws stated. The emissivity values of the samples are tabulated and provided in Table 7.4 below.

Table 7.4 Emissivity values of samples at specified background temperatures.

Sample	Emissivity		
	60 °C	80 °C	100 °C
Al	0.893	0.886	0.888
S.2A	0.935	0.930	0.931
S.1A	0.943	0.935	0.937
S.3A	0.950	0.939	0.940
S.2B	0.952	0.941	0.943
S.1B	0.955	0.945	0.949
S.3B	0.958	0.953	0.951
S.2C	0.960	0.958	0.953
S.1C	0.963	0.961	0.955
S.3C	0.970	0.966	0.958
PU	0.975	0.973	0.964

According to emissivity values, while the bare-PU had the highest, the Al/PU sample had the lowest emissivity. The samples included core/shell structures were lined-up between Al/PU and the bare PU samples. Within the core/shell nanocomposites, the closest one to the Al/PU in terms of emissivity was S.2A. The sequencing for emission was similar to the one obtained in FTIR results. It is observed that the morphology and the ZnO content of shell structure in the core/shell influenced the IR emissivity value.

The composite coatings with Al and Al/ZnO core/shell particles with the two lowest emissivity values were compared depending on the filler to the binder weight ratio. The IR temperatures of the samples prepared at 0.5/1, 1/1, 1.5/1 and 2/1 particle (Al, Al/ZnO)/binder (PU) ratio by weight were measured at 60, 80 and 100 °C background temperatures (Figure 7.14).

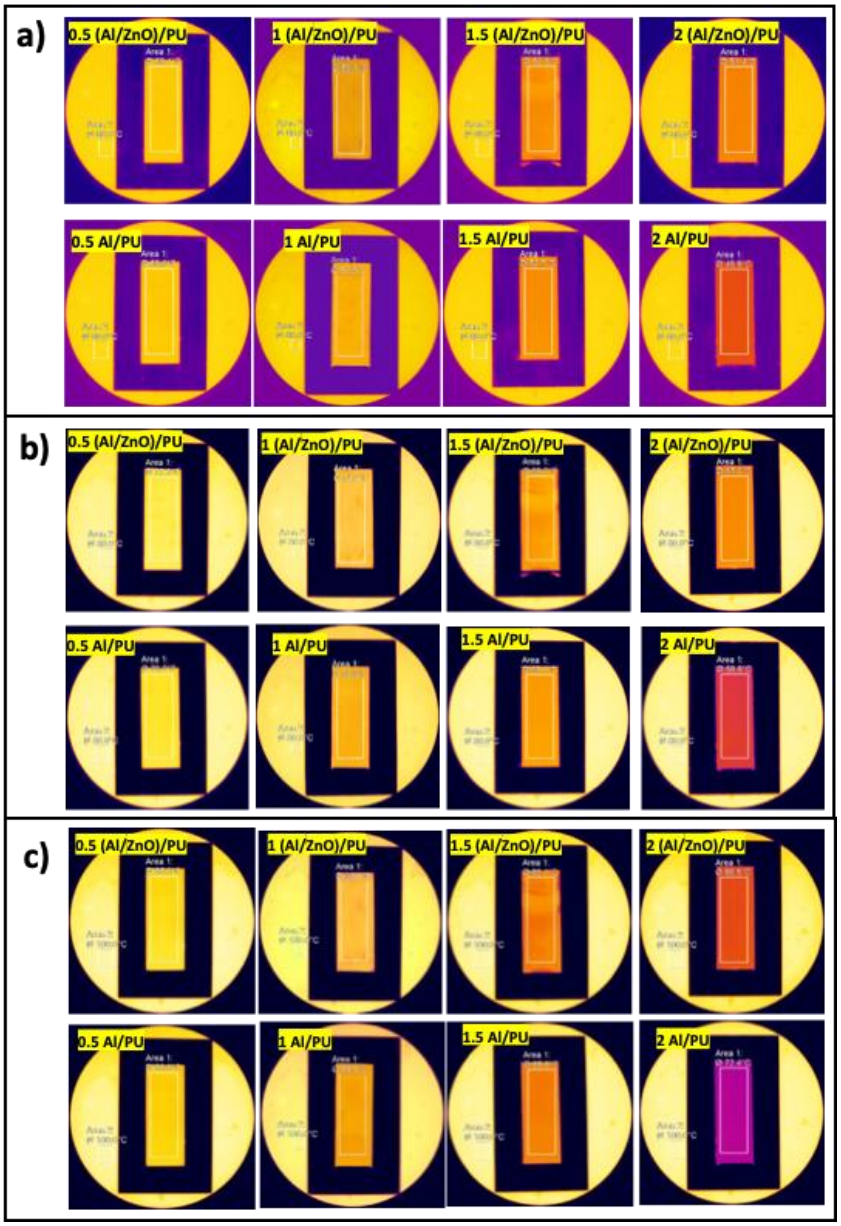

Figure 7.14 Thermal images of samples at background temperatures of a) 60, b) 80 and c) 100 °C with different filler fraction.

As can be seen in the figure, the filler content affects the measured IR temperature of the samples. It was observed that the material was colder than it was as the filler content increased the measured temperatures with thermal camera at background temperatures of 60, 80 and 100 °C is tabulated and provided in Table 7.5.

Table 7.5 IR measured temperatures of samples at specified background temperatures.

Sample	IR Measured Temperature (°C)		
2.0 Al/PU	45.9	58.8	72.4
2.0 (Al/ZnO)/PU	51.4	67.2	80.5
1.5 Al/PU	52.7	69.1	85.8
1.5 (Al/ZnO)/PU	52.9	69.2	86.1
1.0 Al/PU	53.6	70.9	88.8
1.0 (Al/ZnO)/PU	56.1	74.4	93.1
0.5 Al/PU	57.5	76.2	93.8
0.5 (Al/ZnO)/PU	58.1	77.3	95.3

The table shows that the lowest temperatures were obtained by the high-content composite coatings at each background temperature. The 2.0 Al/PU composite coating has the minimum temperature with 45.9, 58.8 and 72.4 °C at 60, 80 and 100 °C background temperatures, respectively. The IR-measured temperature of high-content core/shell composite was lower than that of 1.5 Al/PU material. By arranging the content ratio, it can be stated that the similar IR temperature of Al-filled composite can be achieved with the core/shell composites. IR measured temperatures with respect to background temperatures of the coatings are provided in Figure 7.15.

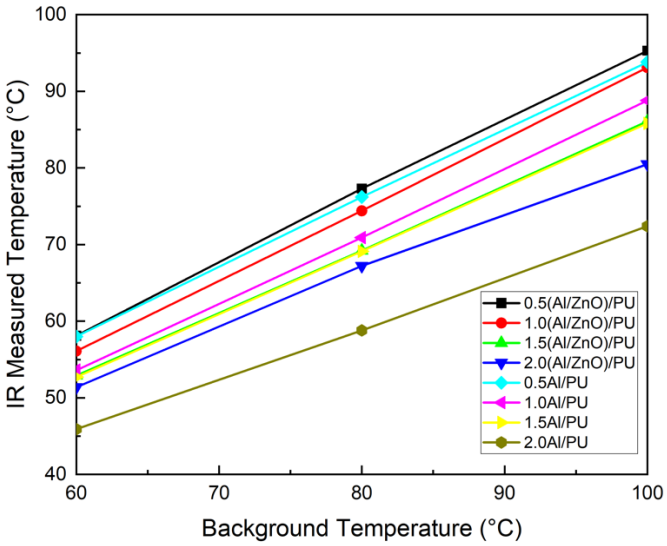

Figure 7.15 IR measured temperatures of core/shell/PU and Al/PU samples with respect to filler content ratio. Lines are for visual aid.

According to the figure, the IR temperatures of the samples increased nearly linearly with the background temperature. The filler type and content in the polymer matrix determined the differences in IR temperatures. The emissivity values of samples with respect to the background temperature are tabulated and provided in Table 7.6.

Table 7.6 Emissivity values of samples with respect to the background temperatures.

Sample	**Emissivity**		
	60 °C	**80 °C**	**100 °C**
2.0 Al/PU	0.765	0.735	0.724
2.0 (Al/ZnO)/PU	0.856	0.840	0.805
1.5 Al/PU	0.878	0.863	0.858
1.5 (Al/ZnO)/PU	0.881	0.865	0.861
1.0 Al/PU	0.893	0.886	0.888
1.0 (Al/ZnO)/PU	0.935	0.930	0.931
0.5 Al/PU	0.958	0.953	0.938
0.5 (Al/ZnO)/PU	0.968	0.967	0.953

The lowest emissivity was obtained for 2.0 Al/PU as 0.724. The second lowest emissivity was calculated for 2.0 (Al/ZnO)/PU as 0.805 and the value was lower than that of 1.5 Al/PU composite. The composite coatings with core/shell particles showed lower emissivity at a higher filler fraction than Al/PU sample. This proves that by increasing the filler ratio of the core/shell powder in the composite, equal emissivity with Al particles can be achieved. The change in emissivity values of composite coatings depending on background temperature are provided in Figure 7.16.

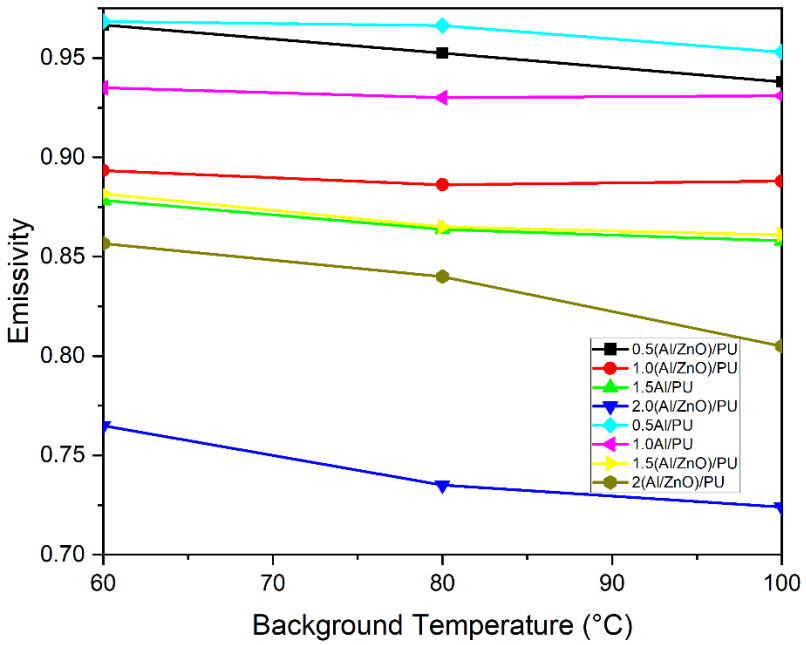

Figure 7.16 Change in thermal emissivity of samples with respect to particle content ratio. Lines are for visual aid.

The figure showed that a slight change was observed in the emissivity of samples as the background temperature increased. The emissivity values of the samples were nearly linear with respect to the background temperatures. The lowest emissivity was observed for 2.0 Al/PU composite material at each temperature, and the closest one was 2.0 (Al/ZnO)/PU. When the filler fraction is increased by 0.5, the emissivity of composite coatings with core/shell materials is lower than that of Al/PU.

7.6 Radar absorbance

The X-band radio frequency absorption and reflection losses were obtained via KEYSIGHT ENA Network Analyzer in the range of 8.2-12.4 GHz. The samples used for the tests had a filler to binder by weight of 2/1, this fraction is used in this chapter. The reflection loss and the transmission loss results were converted into reflectance and transmittance using Fresnel equations. The absorbance was obtained based on the principle of conservation of energy. The reflectance and absorbance of the samples are provided in Figures 7.17 (a) and (b), respectively.

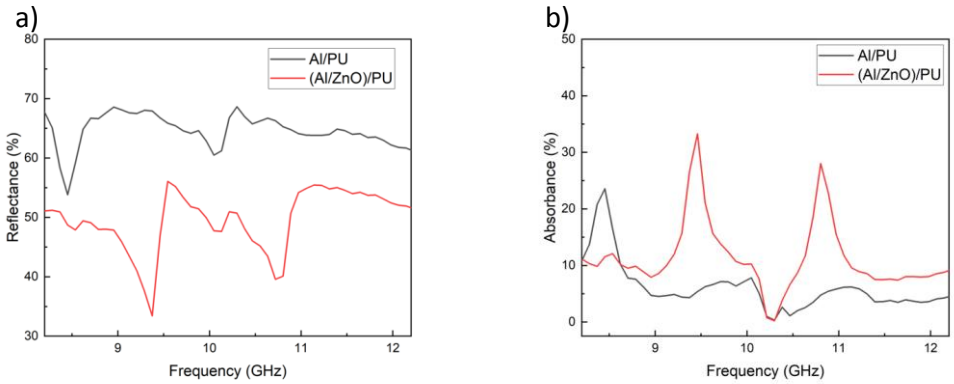

Figure 7.17 X-band radio frequency a) reflectance and b) absorbance spectra of Al/PU and core/shell/PU samples.

As seen in the figure, the samples had similar spectral reflectance behavior, while the core/shell composite had lower reflectance within the investigated 8.2 to 12.4 GHz range. In the absorbance spectra, core/shell composite had broad peaks around 9.4 and 10.8 GHz, while the Al/PU composite had one peak at 8.4 GHz. The average absorbance and reflectance of samples are tabulated and provided in Table 7.7.

Table 7.7 Average reflectance and absorbance of samples in X-band frequency.

Material	Reflectance (%)	Absorbance (%)
Al/PU	61	4
(Al/ZnO)/PU	51	10

As seen in the table, the average absorbance was found to increase by 6% with the addition of core/shell particles into the PU matrix. The reflectance of core/shell composites was raised by 10%. The main parameter taken into consideration was the reflectance, since the transmitted waves will be absorbed by the radar absorbing coating on the aircraft. As a result, with Al/ZnO core/shell structure, by decreasing in the X-band reflectance by 10%, the radar absorbance features of composite coating were considerably improved.

CHAPTER 8

CONCLUSIONS AND FEATURE RECOMMENDATIONS

8.1 Conclusions

In this study, the LWIR low emissivity core/shell particles were investigated. The core/shell materials with high performance on low emissivity were determined as Al, Al/Fe_3O_4, Al/TiO_2, Al/SiO_2, and Al/ZnO from the literature. For a simulation, the particle size was determined as 10 µm and shell thicknesses were investigated between 100 to 400 nm. The pure Al and Al/ZnO core/shell particles were analyzed depending on the shell thickness via FDTD simulation software operating based on the Fresnel Equations. The lowest reflectance was obtained from Al/ZnO as 59.50%, at the shell thickness of 100 nm.

The Al/ZnO core/shell material was synthesized by the solvothermal method for the first time in the literature by changing the Zn molar ratio and the reaction temperature. 9 different samples were synthesized, and detail materials characterization was conducted using XRD and SEM-EDX methods. Crystal structure, morphology and chemical composition of the synthesized materials were analyzed. Results revealed that nanostructured ZnO particles with different morphologies were obtained with the same hexagonal wurtzite crystal structure. The powder samples were mixed with aerospace-standard PU at a weight ratio of 1/1 and homogenously coated onto aluminum and glass substrates by the tape casting method.

The transmittance of powders and composite coatings were examined by FTIR spectroscopy in LWIR band. The results showed that the core/shell structure of S.2A with low-content ZnO and partially flake-shaped shell morphology demonstrated relatively lower absorbance in LWIR band, the highest transmittance spectra was observed in the Al powder. The minimum absorbance of the core/shell composite

coatings on the glass substrate was observed in S.2A/PU, which was hardly more than that of the Al/PU coated sample with an absorbance. Kirchhoff's Law indicates that for an opaque body, absorbance equals emissivity, as discussed in Chapter 3. In the literature, the average emissivity of core/shell materials were calculated by measuring the total reflectance of the material by FTIR with an integrating sphere attachment in LWIR band. To compare with literature, the average absorbance or emissivity of core/shell powders and composite coatings with core/shell particles were calculated by measuring transmittance by FTIR-ATR equipment in this study. The absorbance was calculated using measured transmittance data according to the principle of conservation of energy. The absorbance was accepted as the emissivity of the sample at room temperature.

The LWIR emissivity comparison at room temperature of the Al/ZnO core/shell powders and Al/ZnO/PU composite coatings with the lowest emissivity and core/shell materials in the literature is shown in Table 8.1.

Table 8.1 shows the LWIR emissivity comparison of core/shell materials at room temperature with the lowest emissivity in the literature and Al/ZnO core/shell powders and Al/ZnO/PU composite coatings developed in this study.

Table 8.1 Room temperature emissivity comparison of Al/ZnO with core/shell materials in the literature.

Material	**Emissivity**	**Measurement method**
Al/ZnO/PU	0.03	FTIR transmittance (ATR)
Al/ZnO	0.04	FTIR transmittance (ATR)
Al/Fe_3O_4 [110]	0.54	FTIR reflectance (integrating sphere)
Al/Co_3O_4/lacquer [109]	0.45	FTIR reflectance (integrating sphere)
Al/MnO_2/lacquer[152]	0.3	FTIR reflectance (integrating sphere)
Al/SiO_2 [26]	0.12	FTIR

The results showed that Al/ZnO core/shell powder and composite coating provided the lowest emissivity at room temperature compared to core/shell materials in the

literature. The ZnO shell had a much smaller impact on the LWIR emission of Al particles than that of shell materials in the literature.

The visible reflectance values of the coatings were measured with UV-Vis spectrophotometer, and the results showed that the highest reflectance rate was obtained from Al/PU as 25.88%, while that for S.2A was 21.77%. While the IR absorbance of composite coatings with core/shell and pure Al particles were very close to each other with a small difference, the visible reflectance was decreased by 4.1% with S.2A/PU. At the oblique angle, the minimum reflectance was obtained from S.2A/PU among core/shell composites. The specular reflectance from the surface of the Al/PU and S.2A/PU coatings on the aluminum substrates was measured as 55.52% and 45.45%, respectively. As a result, the FTIR results obtained from powder, composite coatings on glass and composite coatings on Al plate were consistent with each other. Sample S.2A demonstrated comparable IR absorption/reflection characteristics to Al in powder and composite coating form besides providing lower visible reflectance.

According to the thermal imaging results, the minimum thermal emissivity value was obtained from S.2A/PU as 0.93, which was slightly more than that of the Al/PU (0.89) at 100 °C background temperature. Al/PU and S.2A/PU emissivity comparisons were performed based on the particle filler fraction. The minimum emissivity was measured on a 2/1 particle-to-binder ratio by weight. The thermal emissivity of the core/shell composite coating was measured as 0.80 and the coating with the Al powder was 0.72. X-band radar absorbance test was carried out for low-emissivity core/shell composite. The Al-containing sample was used as a reference with equal loading ratio. The average radar reflectance was found to increase by 10% through the use of the core/shell particles.

The simulation was performed to determine the main core/shell material. A single, smooth, and perfectly shaped particle with no defects or failures was used in the simulation. Under experimental conditions, the results were obtained from the powder and coating samples. Particle size, shape and surface morphology were varied in powder and composite coating samples that contain very high amount of

particles. Therefore, the results obtained from the simulation and experiments were not compared with each other.

In conclusion, Al/ZnO core/shell particles were designed and analyzed on virtual conditions, followed by the synthesis. Then characterization and performance tests were conducted. The results revealed that the amount of shell material and shell morphology had a strong influence on the reflectance/absorption features of the core/shell. The Al/ZnO core/shell that have flaky-shell structure resulted in a slight decrease in the IR stealth performance of pure Al. However, in the coating form, when the filler fraction of core/shell composite increased compared to Al/PU, favorable results were obtained in terms of emissivity. Additionally, the visible and radar region absorbance was increased considerably with composite core/shell coatings.

8.2 Future Recommendations

In this study, nanocomposite coatings with high IR reflectance using core/shell particles and PU matrix were simulated and developed. Solvothermal method was used to synthesize core/shell particles. A large-scale method can be developed for the controlled and large-scale synthesis of uniform core/shell particles.

The synthesized Al/ZnO core/shell particles reflectance values were close to that of Al particles, with high visible absorbance. It was observed that the reflectance features of the particles were related to the morphology of the shell layer. Fully flake-shaped and thickness-optimized shell structure might be investigated to determine its effect on reflectance.

Although the core/shell powder composites with PU matrix had similar thermal emissivity values with the Al-filled composite, the thermal emissivity values were found to increase considerably upon mixing the particles with the binder. In this case, it can be said that the polymer binder causes high emissivity. Therefore, a low emissivity binder can be studied to develop low-emissivity material in the LWIR range.

REFERENCES

1. Wilson, J. (2004). Basic Sensor Technology. In Sensor technology handbook. (pp. 1–15). Elsevier.

2. Ou, J., Zhang, J., & Zhan, R. (2020). Processing technology based on radar signal design and classification. International Journal of Aerospace Engineering.

3. Akan, V., & Yazgan, E. (2020). Antennas for Space Applications: A Review. Advanced Radio Frequency Antennas for Modern Communication and Medical Systems.

4. Siemens, A. O. N., & van Hecke, M. (2010). Jamming: A simple introduction. Physica A: Statistical Mechanics and Its Applications, 389(20), 4255–4264.

5. Hoehn, J. R., Gallagher, J. C., & Sayler, K. M. (2022). Defense Primer: Military Use of the Electromagnetic Spectrum.

6. Carlos, C., & Valle Rosa, E. (2020). Elements of Air and Space Power Theory for Developing Air Forces.

7. Stelly, J. M. (2007). Price vs. Performance: The Value of Next Generation Fighter Aircraft.

8. Kapur, V. (2014). Stealth technology and its effect on aerial warfare (pp. 14-33). New Delhi, India: Institute for Defence Studies and Analyses.

9. Zohuri, B. (2020). Radar Energy Warfare and the Challenges of Stealth Technology. Radar Energy Warfare and the Challenges of Stealth Technology.

10. Nellis, A. F. B. (2000). IR Fundamentals. In Electronic Warfare Fundamentals (pp. 105-141)

11. Kumar, N., & Vadera, S. R. (2017). Stealth Materials and Technology for Airborne Systems (pp. 519–537). Springer, Singapore.

12. Ahmad, H., Tariq, A., Shehzad, A., Faheem, M. S., Shafiq, M., Rashid, I. A., Afzal, A., Munir, A., Riaz, M. T., Haider, H. T., Afzal, A., Qadir, M. B., & Khaliq, Z. (2019). Stealth technology: Methods and composite materials—A review. Polymer Composites, 40(12), (pp. 4457–4472.)

13. Feng, L., Liu, Y., Yao, L., Sun, R., & He, J. (2021). Infrared Stealth and Multi-Band Compatible Stealth Materials. Progress in Chemistry, 33(6), 1044.

14. Sun, K., Zhou, W., Tang, X., & Luo, F. (2016). Application of indium tin oxide (ITO) thin film as a low emissivity film on Ni-based alloy at high temperature. Infrared Physics & Technology, 78, 156–161.

15. Zhu, Y., Zhang, L., Wang, J., Feng, B., Feng, M., Gui, B., Wang, J., Xu, C., & Qu, S. (2022). Microwave-infrared compatible stealth via high-temperature frequency selective surface upon Al2O3-TiC coating. Journal of Alloys and Compounds, 920, 165977.

16. Tong, H., Li, H., Huang, H., Wu, A., Cao, T., & Guo, D. (2022). Achievement of low infrared emissivity photonic crystal design on [CdSe/SiO2]N periodic films. Optics & Laser Technology, 156, 108557.

17. Zhang, W., & Lv, D. (2020). Preparation and characterization of Si/SiO2 one-dimensional photonic crystal with ultra-low infrared emissivity in the 3–5 μm band. Optik, 202, 163738.

18. Fang, K. Y., Zhao, Y. C., & Fang, F. (2021). Infrared stealth nanofibrous composite with thermal stability and mechanical flexibility. Journal of Alloys and Compounds, 855, 157418.

19. Qi, L., Weng, X., Wei, B., Yuan, L., Huang, G., Du, X., Wu, X., & Liu, H. (2020). Effects of low-melting glass powder on the thermal stabilities of low infrared emissivity Al/polysiloxane coatings. Progress in Organic Coatings, 142, 105579.

20. Yan, X., & Xu, G. (2012). Influence of silane coupling agent on corrosion-resistant property in low infrared emissivity Cu/polyurethane coating. Progress in Organic Coatings, 73(2–3), 232–238.

21. Wu, G., & Yu, D. (2013). Preparation and characterization of a new low infrared-emissivity coating based on modified aluminum. Progress in Organic Coatings, 76(1), 107–112.

22. Zhang, W., Jiang, S., & Lv, D. (2020). Fabrication and characterization of a PDMS modified polyurethane/Al composite coating with super-hydrophobicity and low infrared emissivity. Progress in Organic Coatings, 143, 105622.

23. Wang, L., Xu, G., Liu, C., Hou, H., & Tan, S. (2019). Surface-modified CeO2 coating with excellent thermal shock resistance performance and low infrared emissivity at high-temperature. Surface and Coatings Technology, 357, 559–566.

24. Li, E., Bai, Y., Dong, H., Jia, R., Zhao, X., Wang, R., Bao, M., & Ma, W. (2021). Infrared radiation and thermal properties of Al-doped SrZrO3 perovskites for potential infrared stealth coating materials in the high-temperature environment. Ceramics International, 47(16), 23124–23133.

25. Wang, Y., Zhou, H., Gao, Y., Zhang, Z., Liu, S., Zhong, S., Yu, M., Liu, J., & Wang, C. (2022). Low-infrared-emissivity Al@SiO2/EPDM composite coating compatible with low dielectric loss and antistatic property. Infrared Physics & Technology, 121, 104025.

26. Chen, L., Ren, Z., Liu, X., Wang, K., & Wang, Q. (2021). Infrared–visible compatible stealth based on Al-SiO2 nanoparticle composite film. Optics Communications, 482, 126608.

27. Wongsuntirad, N., Rakkwamsuk, P., & Harnnarongchai, W. (2018). Development of low-thermal emissivity coating. Materials Today: Proceedings, 5(3), 9603–9608.

28. Liu, F., Shao, X., Han, P., Xiangli, B., & Yang, C. (2014). Detection of infrared stealth aircraft through their multispectral signatures, 53(9), 094101.

29. Zikidis, K., Skondras, A., Lt, H., & Tokas, C. (2014). Low Observable Principles, Stealth Aircraft and Anti-Stealth Technologies. Journal of Computations & Modelling, 4(1), 1792–8850.

30. Hines, N., & Mavris, D. (2000). A parametric design environment for including signatures analysis in conceptual design.

31. Rao, G. A., & Mahulikar, S. P. (2005). New criterion for aircraft susceptibility to infrared guided missiles. Aerospace Science and Technology, 9(8), 701–712.

32. Baranwal, N., & Mahulikar, S. P. (2019). Review of Infrared signature suppression systems using optical blocking method. Defence Technology, 15(3), 432–439.

33. Todd Fisk, C., Reiss Oltman, C., Fleming Thompson, C., Andrew Ward, C., Carter Kunz, C., Rebecca Scott, C., Bret Laxton, C., & Heinrich Bornhorst, C. (2015). Integrating Stealth.

34. Lothes, R. N., Szymanski, M. B., & Wiley, R. G. (1990). Radar vulnerability to jamming. Norwood.

35. Howe, D. (1991). Introduction to the Basic Technology of Stealth Aircraft: Part 2—Illumination by the Enemy (Active Considerations). Journal of Engineering for Gas Turbines and Power, 113(1), 80–86.

36. Saville, P. (2005). Review of Radar Absorbing Materials. Defence Research and Development Atlantic Dartmouth (Canada).

37. Howe, D. (1991). Introduction to the Basic Technology of Stealth Aircraft: Part 1—Basic Considerations and Aircraft Self-Emitted Signals (Passive Considerations). Journal of Engineering for Gas Turbines and Power, 113(1), 75–79.

38. Gaitanakis, G.-K., Vlastaras, A., Vassos, N., Limnaios, G., & Zikidis, K. C. (2019). InfraRed search & track systems as an anti-stealth approach. Scienpress.Com, 9(1), 1792–8850.

39. Martinic, G. (2015). Jet fighter aircraft: five'generations' later, and still counting. Headmark.

40. Bongers, A., & Torres, J. L. (2014). Technological change in U.S. jet fighter aircraft. Research Policy, 43(9), 1570–1581.

41. Mahulikar, S. P., Sonawane, H. R., & Arvind Rao, G. (2007). Infrared signature studies of aerospace vehicles. Progress in Aerospace Sciences, 43(7–8), 218–245.

42. Richardson, M. A. (2008). Low-cost PC-based high-fidelity infrared signature modelling and simulation.

43. Mahulikar, S. P., Potnuru, S. K., & Arvind Rao, G. (2009). Study of sunshine, skyshine, and earthshine for aircraft infrared detection. Journal of Optics A: Pure and Applied Optics, 11(4), 045703.

44. Mahulikar, S. P., Rao, A. G., Sonawane, H., Mahulikar, S. P., Rao, G. A., Sonawane, H. R., & Prasad, H. S. S. (2009). Infrared Signature Studies of Aircraft and Helicopters.

45. Rao, G., aircraft, S. M.-J. of, & 2005, undefined. (2005). Effect of atmospheric transmission and radiance on aircraft infared signatures.

46. Knott, E. F., Shaeffer, J. F., & Tuley, M. T. (1985). Radar cross section: Its prediction measurement and reduction.

47. Knott, E. F. (1990). Radar cross section. In M. I. Skolnik (Ed.), Radar Handbook (2nd ed., pp. 283–316). McGraw-Hill Professional.

48. Sheehan, D. P. (2012). Infrared Cloaking, Stealth, and the Second Law of Thermodynamics. Entropy 2012, Vol. 14, Pages 1915-1938, 14(10), 1915–

49. Min, Y. (1981). Infrared Homing Guidance. Foreign Technology Div Wright-Patterson Afb Oh.

50. Ting Li Chang, by. (1994). The IR missile (spin-scan and con-scan seekers) countermeasures. Naval Postgraduate School Monterey Ca.

51. Srivastava, H., Limbu, Y., Saran, R., Journal, A. K.-D. S., & 2007, undefined. (2007). Airborne infrared search and track systems.

52. Missirian, J.-M., & Ducruet, L. (1997). IRST: a key system in modern warfare. In Infrared Technology and Applications XXIII (Vol. 3061, pp. 554-565). SPIE.

53. Rao, G. A., & Mahulikar, S. P. (2002). Integrated review of stealth technology and its role in airpower. The Aeronautical Journal, 106(1066), 629–642.

54. Baranwal, N., & Mahulikar, S. P. (2016). IR signature study of aircraft engine for variation in nozzle exit area. Infrared Physics & Technology, 74, 21–27.

55. Paszko, M. (2017). Infrared signature suppression systems in modern military helicopters. Prace Instytutu Lotnictwa, Nr 3 (248).

56. Sweetman, B. (1990). Stealth aircraft-history, technology and outlook. Turbo Expo: Power for Land, Sea, and Air, 79054.

57. Kopp, C. (2010). Evolving technological strategy in advanced air defense systems. Joint Force Quarterly, 57, 86–93.

58. Vass, S. (2003). Stealth technology deployed on the battlefield. Informatics Robotics, 2(2), 257–269.

59. Cui, J. F., Ma, Y., Yang, B. P., Guo, J. H., & Zhou, Y. P. (2013). Preparation of infrared stealthy coatings. Applied Mechanics and Materials, 275, 1934–1937.

60. Kao, M.-S., & Chang, C.-F. (2020). EM Wave Propagation. In Understanding Electromagnetic Waves (pp. 51–103). Springer International Publishing.

61. Ida, N. (2015). Electromagnetic waves and propagation. In Engineering electromagnetics (3rd ed., pp. 597–665).

62. Musa, S. M. (2020). Light waves. In Optics: An Introduction. (pp. 1-75)

63. Pathak, P., & Burkholder, R. (2021). Electromagnetic Radiation, Scattering, and Diffraction. John Wiley & Sons.

64. Fitzpatrick, R. (2010). Maxwells equations and the principles of electromagnetics. (pp. 107-156). Laxmi Publications.

65. Mahatme, A. v. (2015). Electromagnetic wave propagation. In Fundamentals of Electromagnetics (pp. 264–315).

66. Wolski, A. (2011). Theory of electromagnetic fields. CAS 2010 - CERN Accelerator School: RF for Accelerators, Proceedings, 15–65.

67. Mahatme, A. v. (2015). Waves at boundary between two media. In Fundamentals of Electromagnetics (1st ed., pp. 84-118).

68. Lee, Y. H. (2013). Time-Harmonic Electromagnetic Waves. In Introduction to engineering electromagnetics (pp. 385–462).

69. Sharma, K. K. (2006). Light Waves. In Optics: principles and applications (pp. 1–77).

70. Jenkins, F. A., & White, H. E. (1957). Geometrical Optics. In Fundamentals of optics (4th ed., pp. 1–215).

71. Tilley, R. J. D. (2010). Light and Colour. In Colour and the optical properties of materials: an exploration of the relationship between light, the optical properties of materials and colour (pp. 1–49).

72. Zwinkels, J. (2015). Light, Electromagnetic Spectrum. Encyclopedia of Color Science and Technology, 1–8.

73. Herter, C. A. Jr. (1985). The Electromagnetic Spectrum: A Critical Natural Resource. Natural Resources Journal, 25.

74. Mouahid, A. (2018). Infrared thermography used for composite materials. MATEC Web of Conferences, 191, 00011.

75. Wake, L. v., & Brady, R. F. (1993). Formulating Infrared Coatings for Defence Applications. Materials Research Labs Ascot Vale (Australia).

76. Cengel, Y., & Boles, M. (2003). Fundamentals of Thermal Radiation. In Heat Transfer: A Pratical Approach (2nd ed., pp. 561–604).

77. Gaussorgues, G., & Seweryn, C. (1993). Thermal Emission By Matter. In Infrared Thermography (Vol. 5, pp. 11–52).

78. Bass, M., Stryland, E. W. van, Williams, D. R., & Wolfe, W. L. (1995). Radiometry and Photometry. In Handbook of Optics Volume II Devices, Measurements, and Properties (2nd ed., Vol. 3, pp. 972–1014).

79. Papas, C. H. (2014). Radio-astronomical antennas. In Theory of electromagnetic wave propagation (pp. 109–168).

80. Johnson, C. (2012). Planck-Stefan-Boltzmann Laws. In Mathematical Physics of BlackBody Radiation (pp. 17–27).

81. Bramson, & Abramovic, M. (1968). Blackbody Radiation Laws. In Infrared radiation. A handbook for applications (1st ed., Vol. 1, pp. 41–55).

82. Topp, K., Haase, H., Degen, C., Illing, G., & Mahltig, B. (2014). Coatings with metallic effect pigments for antimicrobial and conductive coating of textiles with electromagnetic shielding properties. Journal of Coatings Technology and Research, 11(6), 943–957.

83. Wang, K., Wang, C., Yin, Y., & Chen, K. (2017). Modification of Al pigment with graphene for infrared/visual stealth compatible fabric coating. Journal of Alloys and Compounds, 690, 741–748.

84. Yuan, L., Weng, X. L., Xie, J. L., & Deng, L. J. (2015). Effects of shape, size and solid content of Al pigments on the low-infrared emissivity coating.

85. Hu, C., Xu, G., & Shen, X. (2009). Preparation and characteristics of thermal resistance polysiloxane/Al composite coatings with low infrared emissivity. Journal of Alloys and Compounds, 486(1–2), 371–375.

86. Yu, H., Xu, G., Shen, X., Yan, X., Shao, C., & Hu, C. (2009). Effects of size, shape and floatage of Cu particles on the low infrared emissivity coatings. Progress in Organic Coatings, 66(2), 161–166.

87. Yu, H., Xu, G., Shen, X., Yan, X., & Cheng, C. (2009). Low infrared emissivity of polyurethane/Cu composite coatings. Applied Surface Science, 255(12), 6077–6081. https://doi.org/10.1016/J.APSUSC.2009.01.019

88. Chou, K. sen, & Lu, Y. C. (2007). The application of nanosized silver colloids in far infrared low-emissive coating. Thin Solid Films, 515(18), 7217–7221.

89. Zhang, W., Xu, G., Ding, R., Qiao, J., & Duan, K. (2013). Microstructure, optimum pigment content and low infrared emissivity of polyurethane/Ag composite coatings. Physica B: Condensed Matter, 422, 36–39.

90. Zhao, J., Luo, W., Qi, L., Yuan, L., Huang, G., Huang, Y., & Weng, X. (2018). The High-Temperature Resistance Properties of Polysiloxane/Al Coatings with Low Infrared Emissivity. Coatings 2018, Vol. 8, Page 125, 8(4), 125.

91. Hallberg, T., Niinimaki-Heikkila, T., Hedborg-Karlsson, E., Salonen, P. S., Nilssom, C., & Jannis, A. (2005). Development of Low-emissive Camouflage Paint: Final Report.

92. Hu, C., Xu, G., Shen, X., Huang, R., & Li, F. L. (2010). Thermal ageing studies on low infrared emissivity composite coatings. Journal of Alloys and Compounds, 496(1–2), 691–694.

93. Zhou, Q., Zhu, S., Ma, Z., Liu, Y., Liu, L., & Gao, L. (2022). Experimental and first-principles study on the effect of oxygen vacancy on infrared emissivity of CeO2. Ceramics International, 48(8), 11313–11319.

94. Zhang, M., Li, M., Yan, Z., Zhang, L., Yin, J., Ma, X., Li, W., & Deng, L. (2022). Multifunctional Ag-ZrB2 composite film with low infrared emissivity, low visible light reflectance and hydrophobicity. Applied Surface Science, 604, 154626.

95. Chen, J., Zhou, Y., Nan, Q., Sun, Y., Ye, X., & Wang, Z. (2007). Synthesis, characterization and infrared emissivity study of polyurethane/TiO2 nanocomposites. Applied surface science, 253(23), 9154-9158.

96. Yang, Y., Tan, S., Fang, G., Yang, Z., Li, Y., & Yang, C. (2020). The compatible performance of three-dimensional SiO2–ZnO amorphous photonic crystals in adjustable structural color and low infrared emissivity. Optical Materials, 107, 110105.

97. Guo, T., Xu, G., Tan, S., Yang, Z., Bu, H., Fang, G., Hou, H., Li, J., & Pan, L. (2019). Controllable synthesis of ZnO with different morphologies and their morphology-dependent infrared emissivity in high temperature conditions. Journal of Alloys and Compounds, 804, 503–510.

98. Xiang, S., Xu, G., Liu, C., Bu, H., & Zhang, Y. (2018). Study on the variable color and emissivity properties of Co doped TiO2 under temperature fluctuations. Optical Materials, 85, 254–260.

99. Guo, T., Tan, S., Xu, G., Ma, J., Liu, X., Ji, G., Liu, G., He, Y., & Zhang, S. (2020). Temperature-dependent infrared emissivity property of Ce-doped ZnO nanoparticles. Ceramics International, 46(2), 1569–1576.

100. Ji, H., Liu, D., Cheng, H., Zhang, C., & Yang, L. (2018). Vanadium dioxide nanopowders with tunable emissivity for adaptive infrared camouflage in both thermal atmospheric windows. Solar Energy Materials and Solar Cells, 175, 96–101.

101. Wang, Z., Zhang, J., Xie, J., Li, C., Li, Y., Liang, S., Tian, Z., Wang, T., Zhang, H., Li, H., Xu, W., & Yang, B. (2010). Bioinspired Water-Vapor-Responsive Organic/Inorganic Hybrid One-Dimensional Photonic Crystals with Tunable Full-Color Stop Band. Advanced Functional Materials, 20(21), 3784–3790.

102. Zhang, W., & Lv, D. (2019). Preparation and characterization of Ge/TiO2//Si/SiO2 one-dimensional heterostructure photonic crystal with infrared spectrally selective low emissivity. Optical Materials, 96, 109333.

103. Qi, D., Wang, X., Cheng, Y., Gong, R., & Li, B. (2016). Design and characterization of one-dimensional photonic crystals based on ZnS/Ge for infrared-visible compatible stealth applications. Optical Materials, 62, 52–56.

104. Pan, M., Huang, Y., Li, Q., Luo, H., Zhu, H., Kaur, S., & Qiu, M. (2020). Multi-band middle-infrared-compatible camouflage with thermal management via simple photonic structures. Nano Energy, 69, 104449.

105. Zhang, W., Ma, Z., Lv, D., Luo, J., & Li, J. (2022). An ultra-low infrared emissivity composite coating with outstanding mechanical properties and salt water resistance. Infrared Physics & Technology, 126, 104351.

106. Hsissou, R., Seghiri, R., Benzekri, Z., Hilali, M., Rafik, M., & Elharfi, A. (2021). Polymer composite materials: A comprehensive review. Composite Structures, 262, 113640.

107. Gibson, R. F. (2010). A review of recent research on mechanics of multifunctional composite materials and structures. Composite Structures, 92(12), 2793–2810.

108. Hayes, R., Ahmed, A., Edge, T., & Zhang, H. (2014). Core–shell particles: Preparation, fundamentals and applications in high performance liquid chromatography. Journal of Chromatography A, 1357, 36–52.

109. Liu, Y., Xie, J., Luo, M., Jian, S., Peng, B., & Deng, L. (2017). The synthesis and characterization of Al/Co3O4 magnetic composite pigments with low infrared emissivity and low lightness. Infrared Physics & Technology, 83, 88–93.

110. Yuan, L., Weng, X., Xie, J., Du, W., & Deng, L. (2013). Solvothermal synthesis and visible/infrared optical properties of Al/Fe3O4 core–shell magnetic composite pigments. Journal of Alloys and Compounds, 580, 108–113.

111. Yang, Y., Zhou, Y., & Wang, T. (2014). Preparation of optically active polyurethane/TiO2/MnO2 multilayered nanorods for low infrared emissivity. Materials Letters, 133, 269–273.

112. Ye, X., Wang, Z., Zhang, L., Wang, Q., Xiao, X., Cai, S., Chen, D., & Liu, H. (2019). Synthesis and infrared emissivity properties of novel polyurethane/Ag/ZnO array composite coatings. Infrared Physics & Technology, 102, 103049.

113. Zhang, Z., Xu, M., Ruan, X., Yan, J., Yun, J., Zhao, W., & Wang, Y. (2017). Enhanced radar and infrared compatible stealth properties in hierarchical SnO2@ZnO nanostructures. Ceramics International, 43(3), 3443–3447.

114. Yee, K. S. (1966). Numerical Solution of Initial Boundary Value Problems Involving Maxwell's Equations in Isotropic Media. IEEE Transactions on Antennas and Propagation, 14(3), 302–307.

115. Gedney, S. D. (2011). Introduction to the Finite-Difference Time-Domain (FDTD) Method for Electromagnetics. Synthesis Lectures on Computational Electromagnetics, 27, 1–250.

116. Taflove, A., Hagness, S. C., & Piket-May, M. (2005). Computational Electromagnetics: The Finite-Difference Time-Domain Method (Vol. 3, pp. 629–670).

117. Schneider, J. B. (2012). Understanding the Finite-Difference Time-Domain Method. School of electrical engineering and computer science Washington State University, 28.

118. Reddy, V. S., & Garg, R. (2015). Finite Difference Time Domain (FDTD) Analysis of Microwave Circuits—A Review with Examples. IETE Journal of Research, 45(1), 20.

119. Palik, E. D. (1985). Metals. In Handbook of Optical Constants of Solids (1st ed., Vol. 1, pp. 341–488). Elsevier Inc.

120. Querry, M. R. (1985). Optical Constants. Missouri Univ-Kansas City.

121. Kischkat, J., Peters, S., Gruska, B., Semtsiv, M., Chashnikova, M., Klinkmüller, M., Fedosenko, O., MacHulik, S., Aleksandrova, A., Monastyrskyi, G., Flores, Y., & Masselink, W. T. (2012). Mid-infrared optical properties of thin films of aluminum oxide, titanium dioxide, silicon dioxide, aluminum nitride, and silicon nitride. Applied Optics, Vol. 51, Issue 28, Pp. 6789-6798, 51(28), 6789–6798.

122. Frank, W. B., Haupin, W. E., Vogt, H., Bruno, M., Thonstad, J., Dawless, R. K., Kvande, H., & Taiwo, O. A. (2009). Aluminum. Ullmann's Encyclopedia of Industrial Chemistry.

123. Lv, X., Gao, Y., Cui, Y., Wang, C., Zhang, G., Wang, F., Liu, P., & Ao, W. (2023). Study of ignition and combustion characteristics of kerosene-based nanofluid fuel containing n-Al/CuO thermite. Fuel, 331, 125778.

124. Sharma, D. K., Shukla, S., Sharma, K. K., & Kumar, V. (2022). A review on ZnO: Fundamental properties and applications. Materials Today: Proceedings, 49, 3028–3035.

125. Tang, Q., Li, Y., Zhou, Z., Chen, Y., & Chen, Z. (2010). Tuning electronic and magnetic properties of wurtzite ZnO nanosheets by surface hydrogenation. ACS Applied Materials and Interfaces, 2(8), 2441–2447.

126. Peng, K., Liu, C., Wu, Y., Fang, G., Xu, G., Zhang, Y., Wu, C., & Yan, M. (2022). Understanding the efficient microwave absorption for FeCo@ZnO flakes at elevated temperatures a combined experimental and theoretical approach. Journal of Materials Science & Technology, 125, 212–221.

127. Lei, C., Ge, C., Ge, X., Qian, J., & Du, Y. (2022). Enhanced microwave absorption of flaky FeSiAl/ZnO composites fabricated via precipitation. Materials Science and Engineering: B, 275, 115502.

128. Hasnidawani, J. N., Azlina, H. N., Norita, H., Bonnia, N. N., Ratim, S., & Ali, E. S. (2016). Synthesis of ZnO Nanostructures Using Sol-Gel Method. Procedia Chemistry, 19, 211–216.

129. Ayudhya, S. K. N., Tonto, P., Mekasuwandumrong, O., Pavarajarn, V., & Praserthdam, P. (2006). Solvothermal synthesis of ZnO with various aspect ratios using organic solvents. Crystal Growth and Design, 6(11), 2446–2450.

130. Kolodziejczak-Radzimska, A., & Jesionowski, T. (2014). Zinc Oxide—From Synthesis to Application: A Review. Materials 2014, Vol. 7, Pages 2833-2881, 7(4), 2833–2881.

131. Li, J., Wu, Q., & Wu, J. (2015). Synthesis of nanoparticles via solvothermal and hydrothermal methods. Handbook of Nanoparticles, 295–328.

132. Demazeau, G. (2007). Solvothermal reactions: an opening-up on the synthesis of novel materials or the development of new processes. 27(1), 173–177.

133. Demazeau, G. (2008). Solvothermal reactions: An original route for the synthesis of novel materials. Journal of Materials Science, 43(7), 2104–2114.

134. Ahmed, D., Osman, M., & Abbas Mustafa, M. (2015). Synthesis and Characterization of Zinc Oxide Nanoparticles using Zinc Acetate Dihydrate and Sodium Hydroxide. Journal of Nanoscience and Nanoengineering, 1(4), 248–251.

135. Ismail, A. A., El-Midany, A., Abdel-Aal, E. A., & El-Shall, H. (2005). Application of statistical design to optimize the preparation of ZnO nanoparticles via hydrothermal technique. Materials Letters, 59(14–15), 1924–1928.

136. Macanás, J., Soler, L., Candela, A. M., Muñoz, M., & Casado, J. (2011). Hydrogen generation by aluminum corrosion in aqueous alkaline solutions of inorganic promoters: The AlHidrox process. Energy, 36(5), 2493–2501.

137. Kim, D. W., Kim, K. T., Kwon, G. H., Song, K., & Son, I. (2019). Self-propagating heat synthetic reactivity of fine aluminum particles via spontaneously coated nickel layer. Scientific Reports, 9(1), 1033.

138. Aegerter, M. A., & Mennig, M. (2004). Wet Chemical Coating Technologies. Sol-Gel Technologies for Glass Producers and Users, 15–137.

139. Jabbari, M., Bulatova, R., Tok, A. I. Y., Bahl, C. R. H., Mitsoulis, E., & Hattel, J. H. (2016). Ceramic tape casting: A review of current methods and trends with emphasis on rheological behaviour and flow analysis. Materials Science and Engineering: B, 212, 39–61.

140. Nishihora, R. K., Rachadel, P. L., Quadri, M. G. N., & Hotza, D. (2018). Manufacturing porous ceramic materials by tape casting—A review. Journal of the European Ceramic Society, 38(4), 988–1001.

141. Chin, W. S. (2007). Development of the composite RAS (radar absorbing structure) for the X-band frequency range. Composite structures, 77(4), 457-465.

142. Vamsi Krishna, M., & Xavior, M. A. (2015). Experiment and statistical analysis of end milling parameters for Al/SiC using response surface methodology. Int. J. Eng. Technol, 7, 2274–2285.

143. Wang, S. B., Ran, Q., Yao, R. Q., Shi, H., Wen, Z., Zhao, M., Lang, X. Y., & Jiang, Q. (2020). Lamella-nanostructured eutectic zinc–aluminum alloys as reversible and dendrite-free anodes for aqueous rechargeable batteries. Nature Communications 2020 11:1, 11(1), 1–9.

144. Sharma, T., & Garg, M. (2022). Optical and morphological characterization of ZnO nano-sized powder synthesized using single step sol-gel technique. Optical Materials, 132, 112794.

145. Kovács, Z., Molnár, C., Gyulavári, T., Magyari, K., Tóth, Z. R., Baia, L., Pap, Z., & Hernádi, K. (2022). Solvothermal synthesis of ZnO spheres: Tuning the structure and morphology from nano- to micro-meter range and its impact on their photocatalytic activity. Catalysis Today, 397–399, 16–27.

146. Barreto, G. P., Morales, G., & Quintanilla, M. L. L. (2013). Microwave assisted synthesis of ZnO nanoparticles: effect of precursor reagents, temperature, irradiation time, and additives on nano-ZnO morphology development. Journal of Materials, 2013, 1-11.

147. Pérez-Zúñiga, G., Herrera-Pérez, G., Verde-Gómez, Y., & Valenzuela-Muñiz, A. M. (2021). Self-assembled ZnO-rGO nanocomposite, a solid-state transformation to control its crystallite size. Journal of Alloys and Compounds, 875, 159992.

148. Bahadur, A., Shoaib, M., Saeed, A., & Iqbal, S. (2016). FT-IR spectroscopic and thermal study of waterborne polyurethane-acrylate leather coatings using tartaric acid as an ionomer. e-Polymers, 16(6), 463-474.

149. Mohammadi, A., Barikani, M., & Barmar, M. (2015). Synthesis and investigation of thermal and mechanical properties of in situ prepared

biocompatible Fe3O4/polyurethane elastomer nanocomposites. Polymer Bulletin, 72(2), 219–234.

150. Parra, M. R., & Haque, F. Z. (2014). Aqueous chemical route synthesis and the effect of calcination temperature on the structural and optical properties of ZnO nanoparticles. Journal of Materials Research and Technology, 3(4), 363–369.

151. Agarwal, S., Jangir, L. K., Rathore, K. S., Kumar, M., & Awasthi, K. (2019). Morphology-dependent structural and optical properties of ZnO nanostructures. Applied Physics A: Materials Science and Processing, 125(8), 1–7.

152. Liu, Y., Xie, J., Luo, M., Peng, B., Xu, C., & Deng, L. (2017). The synthesis and optical properties of Al/MnO2 composite pigments by ball-milling for low infrared emissivity and low lightness. Progress in Organic Coatings, 108, 30-35.